Measurement and QCD Analysis of Event Shape Variables in Deep-Inelastic Electron-Proton Collisions at HERA

Von der Fakultät für Mathematik, Informatik und Naturwissenschaften der Rheinisch-Westfälischen Technischen Hochschule Aachen zur Erlangung des akademischen Grades eines Doktors der Naturwissenschaften genehmigte Dissertation

vorgelegt von

Diplom-Physiker
Thomas Kluge
aus Mönchengladbach

Berichter: **Universitätsprofessor Dr. Ch. Berger**
Universitätsprofessor Dr. G. Flügge

Tag der mündlichen Prüfung: 16. April 2004

Abstract

Deep-inelastic ep scattering data, taken with the H1 detector at HERA and corresponding to an integrated luminosity of 106 pb^{-1} are used to study the differential distributions of event shape variables. These include two-jet event shapes (thrust, jet broadening, jet mass and the C-parameter), as well as three-jet event shapes (out-of-event-plane momentum and azimuthal correlation) and jet rates. The four-momentum transfer Q is taken to be the relevant energy scale and ranges between 14 GeV and 200 GeV. The event shape distributions are compared with perturbative QCD predictions, which include resummed contributions for many of the observables. Power law corrections are applied to the predictions to account for hadronisation effects. A QCD fit is presented for the two-jet event shapes and consistent results are found for the strong coupling constant α_s and the non-perturbative parameter α_0.

Kurzfassung

Im Rahmen der vorliegenden Arbeit werden differenzielle Verteilungen von Ereignisformvariablen in tiefunelastischer ep Streuung untersucht. Der zugrundeliegende Datensatz wurde mit dem H1-Detektor bei HERA gewonnen und entspricht einer integrierten Luminosität von 106 pb^{-1}. Es werden zwei-Jet Variablen (Thrust, Jetbreite, Jetmasse und der C-Parameter), drei-Jet Variablen ("out-of-event-plane momentum" und azimutale Korrelation) und Jetraten studiert. Der Viererimpulsübertrag Q wird als die relevante Energieskala verwendet und nimmt Werte zwischen 14 GeV und 200 GeV an. Die Verteilungen der Ereignisformvariablen werden mit Vorhersagen der QCD verglichen, welche für viele der Observablen resummierte Anteile beinhalten. Hadronisierungseffekte werden durch potenzartige Korrekturen der Vorhersagen berücksichtigt. Schließlich wird ein QCD-Fit der zwei-Jet Variablen präsentiert, die Ergebnisse für die starke Kopplungskonste α_s und den nicht-perturbativen Parameter α_0 sind hierbei konsistent.

Contents

Introduction

The **standard model** of particle physics describes matter as consisting of structureless elementary particles (quarks and leptons), governed by renormalisable quantum field theories: the electroweak theory and quantum chromo dynamics (QCD). This model has to be considered as a great success, because since its invention and rise in the 1970s lots of high precision measurements have been performed, none of them able to falsify the model.

While the standard model does provide correct predictions, it is unfortunately an incomplete theory, e.g. it does not include gravity and fails to predict elementary particle masses. There are several possible extensions of the standard model on the market, hence it is now up to high energy physics experimentalists to rule out part of the hypotheses. These days new evidences appear to be just around the corner, the upcoming large hadron collider (LHC) is expected to shed light on the Higgs sector and possible super symmetric particles.

QCD is the constituent of the standard model which describes the dynamics between strong interacting particles, i.e. quarks and gluons. At high energies the large collider experiments challenge the theory by measurements of various cross sections with high precision. Perturbative calculations are the standard tools to obtain numerical results from QCD in this regime. In many cases the limited precision of the calculations affects the conclusions. The precision of perturbative predictions is an issue, because the determination of the corresponding matrix elements proves to be difficult and is often at best available for the first non-vanishing term of the series. Moreover, the uncertainty on the **strong coupling constant** α_s, the single free parameter of QCD, is still large.

Why is it nowadays still important to investigate QCD? Although meanwhile the foundations of quantum chromo dynamics appear to be well founded, there are still areas which are subject to developments:

- The region of low energy, where the application of perturbative methods is prohibitive, poses still many open questions. An important example is the **hadronisation process**, i.e. the transition from quarks to hadrons. Effects originated by this process are virtually always present in high energy physics measurements and are often not negligible.

- Another relevant application is the description of **high jet multiplicities**, i.e.

reactions where collimated, high momentum particle sprays in the final state are observed. While it is already interesting to test if QCD describes these kind of reactions, there is another motivation to study multi jet reactions: They are an important background for exotic reactions investigated now e.g. at the hadron electron ring accelerator (HERA) and in the future at the LHC.

This work studies QCD with means of **event shape variables**, an approach which highlights the connection of the perturbative and non-perturbative parts of QCD: the sensitivity being to the hard scattering matrix elements as well as to the following hadronisation. Hadronic final states in **deep-inelastic scattering** (DIS) offer the advantage to probe QCD over a wide range of momentum transfer Q in a single experiment.

Event shape variables have been studied before, in e^+e^- annihilation as well as in DIS at HERA. In this thesis the topic is revisited with a larger data sample compared to former H1 analyses and improved data reconstruction and correction techniques. Due to recent progress on theory side, it is now possible to study the **whole spectra** of event shape variables instead of only the mean values. Additional event shape variables are investigated for the first time in DIS, which are sensitive to 3-jet production: in total ten event shape variables are studied.

The thesis is organised as follows: Chapter 1 gives an overview of the theoretical foundations of event shape variables in deep-inelastic scattering and introduces the observables. The data set the analysis is based on was taken with the H1 detector at HERA, whose basic features are given in Chapter 2. The selection of the data set is described in detail in Chapter 3, where also the reconstruction techniques used are discussed. Subsequently in Chapter 4 the data correction procedure is presented and the results of the data measurement are given. In Chapter 5 a QCD analysis of five event shape variables is presented, based on the resummed and matched calculations accompanied with power corrections. Finally, the results are summarised and an outlook is given.

Chapter 1

Event Shape Variables

Firstly, this chapter gives a short overview on the topic of event shape variables. Then the deep-inelastic scattering process, which is investigated at HERA, is briefly discussed. The Breit frame of reference is introduced and the definitions of the event shape variables which are studied in this thesis are given.

1.1 Overview

Event shape variables were originally invented to study the characteristics of hadronic final states in e^+e^-annihilation [1, 2, 3]. The intention is to define a variable as a function of the hadron four momenta which describes the spatial shape of an event. For example the event shape variable "thrust" discriminates between more pencil-like and more isotropic hadron configurations. In general parts of the phase space are calculable with precision by perturbative QCD. Thus it is possible to test the SU(3) group structure of the theory [4] and to determine the strong coupling constant α_s [5]. First indications were provided that gluons are actually vector particles with analyses of quantities like thrust [6].

Mean values and spectra of event shapes have been studied, whereby perturbative calculations to fixed order in α_s fail to describe the part of the spectra where soft gluon emission becomes important. In this region **resummed calculations** are needed, which incorporate only an approximation of the exact matrix element, but this approximation to all orders in the α_s expansion.

Event shapes can be adapted to DIS if modifications are made, which take into account that the initial state is not a hadronic vacuum but contains the incident proton beam [7]. Since in DIS the effective center of mass energy is variable for fixed beam energies, the scale dependence of event shapes can be probed by just one individual experimental setup. This has an advantage compared to e^+e^- annihilation, where results from different experiments and/or beam energies need to be combined. While analyses of event shapes in DIS are relevant on their own, it is especially interesting to compare with the results from e^+e^- annihilation, in order

to check the universality of QCD. Despite the slightly different definitions, similar results were found for ep scattering and e^+e^- annihilation [8].

Perturbative calculations based on scattering matrix elements are always dealing with (coloured) partons, while measurements are made on (colourless) hadrons. Technically, event shape variables can be calculated from four-momenta of both partons and hadrons, but it is far from obvious that the detector measurements can be described by perturbative parton calculations without additional corrections. Though important for virtually any high energy physics analysis, the hadronisation process proves still to be one of the major unsolved problems in QCD. There are phenomenological models for this process, e.g. the Lund string model and cluster fragmentation (implemented in the programs JETSET [9] and HERWIG [10], respectively), which are tuned to give a good description of the data. However, from a theoretical point of view, it is unsatisfactory that these models are not derived from first principles. Moreover, phenomenological models employ (often numerous) unphysical parameters and, even worse, the uncertainties of the predictions are unknown.

It is quite common to choose the observables and the phase space under study such that the impact of hadronisation is small. The remaining effects are then estimated with the Monte Carlo models mentioned above, and applied as corrections to the parton level prediction of fixed order perturbative calculations. This approach is questionable, because the order in α_s of the included matrix elements differs in general in calculations and Monte Carlo generators. Furthermore, parton showers were up to now only employed in Monte Carlo generators to make up for higher orders, thus the interface between the uncorrected perturbative calculation and the hadronisation correction is not well defined. However, recently the matching between a next-to-leading-order calculation and parton shower simulations succeeded [11], showing great promise for future.

A possible way to overcome the shortcomings of hadronisation models could be the concept of universal power corrections [12]. Here a formally perturbative ansatz is used to deal with the hadronisation, the only free parameter α_0 being the average strength of a hypothetical, non-perturbative, infrared finite coupling α_{eff}. Power corrections have been successfully applied in analyses of event shapes variables in ep-scattering as well as in e^+e^--annihilation. There are also other areas, e.g. jet cross sections in $p\overline{p}$ collisions [13] were power like corrections find application.

Results on the analysis of mean event shape variables in DIS have been published by the H1 Collaboration [14]. These results give support to the concept of power corrections in the approach by Dokshitzer, Webber et al. [12] for the description of the hadronisation. However, a large spread of the fitted values for $\alpha_s(m_Z)$ lead to the assumption that higher order QCD corrections are needed.

The present work puts emphasis on the analysis of differential distributions of event shape variables in DIS. The evaluation of shapes of this distributions provides additional sensitivity compared to the mean values, which are simply the first mo-

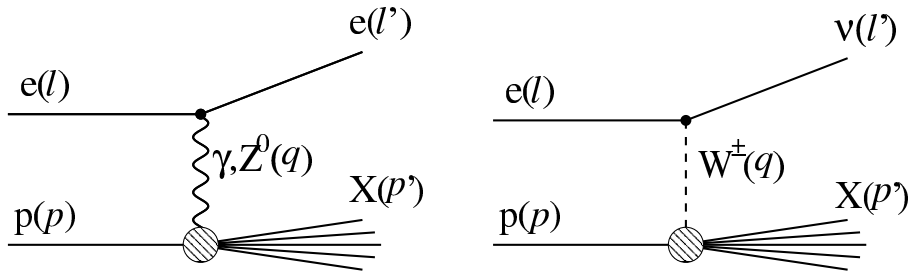

Figure 1.1: Diagrams of inelastic *ep*-scattering in Born approximation. Shown are the neutral current (left) and the charged current (right) reaction.

ments of the distributions. It is also advantageous that QCD fits can be restricted to an interval of the full spectrum where the theoretical predictions are reliable, whereby the mean value includes the complete range by definition.

1.2 Event Shapes in Deep Inelastic Scattering

The production of hadrons in the final state of deep-inelastic *ep* scattering forms the basis of this analysis. In this section a short overview of the theoretical foundations of this process is given, whereby the features important for the present analysis are discussed in more detail.

1.2.1 Kinematics

The investigation of *ep* scattering provides an insight into the elementary interactions participating in the process, namely electroweak theory and quantum chromo dynamics. There are two contributions to the total cross section at HERA, shown as diagrams in Fig. 1.1: the neutral current process (NC), where a photon or a massive Z^0 boson mediates the interaction, and the charged current process (CC), where a W boson is exchanged. The four-momenta are labeled as follows:

- l: incoming electron,
- l': scattered lepton,
- p: incoming proton,
- p': all particles in the hadronic final state X,
- q: exchanged vector boson, space like.

The kinematics of ep scattering can be determined by measurements of the scattered lepton and/or the hadronic final state. The momentum of the final state neutrino in charged current reactions cannot be directly measured (in a multi purpose detector of the size of H1), resulting in a less accurate reconstruction of the kinematics. Therefore only the neutral current reaction is discussed in the present analysis.

The kinematics of ep scattering are commonly specified by the following Lorentz invariant quantities, defined via the four-momenta l, p and q:

$$s = (l+p)^2, \quad W^2 = (p+q)^2, \quad Q^2 = -q^2 = -(l-l')^2,$$

$$x = \frac{Q^2}{2p \cdot q}, \quad y = \frac{p \cdot q}{p \cdot l}, \tag{1.1}$$

where s is the center of mass energy squared, Q^2 the negative four momentum squared of the exchanged boson, W the invariant mass of the hadronic final state, x the Bjørken scale variable and y the inelasticity. If $Q^2 \gtrsim 5\,\mathrm{GeV}$ and $W \gg m_p$ the reaction is called deep-inelastic scattering (DIS).

Energy-momentum conservation implies $Q^2 = sxy$ and $W^2 = Q^2(1-x)/x$ (if the masses of the electron and proton are ignored), hence only three of the kinematic variables are independent. For fixed beam momenta the center of mass energy $\sqrt{s}$ is constant and one is left with two independent variables, whereby Q^2 and x are most often used. In Born approximation and the infinite momentum frame of the proton x corresponds to the proton momentum fraction which is carried by the struck parton.

The double differential Born cross section for neutral current scattering is given by

$$\frac{\mathrm{d}^2\sigma_{\mathrm{NC}}^{e^\pm p}}{\mathrm{d}x\mathrm{d}Q^2} = \frac{2\pi\alpha^2}{xQ^4}\left[\left(1+(1-y)^2\right)\tilde{F}_2(x,Q^2) - \frac{y^2}{2}\tilde{F}_L(x,Q^2) \mp \left(y - \frac{y^2}{2}\right)x\tilde{F}_3(x,Q^2)\right], \tag{1.2}$$

where α is the electromagnetic fine structure constant. Each of the generalised structure functions $\tilde{F}_2$ and $\tilde{F}_L$ includes contributions from photon exchange, photon-Z^0 interference and Z^0 exchange. In contrast $x\tilde{F}_3$ misses the pure photon exchange contribution and only depends on photon-Z^0 interference and Z^0 exchange terms. The weak contributions due to the Z^0 are suppressed for $Q^2 \ll m_Z^2 = 8\,315\,\mathrm{GeV}^2$ because of a propagator term $\frac{Q^2}{Q^2+m_Z^2}$. In the present work values of Q^2 up to $10\,000\,\mathrm{GeV}^2$ are observed, therefore Z^0 exchange can in general not be neglected.

QED radiative corrections modify the simple Born picture. Experimentally, real photon emissions are especially important, because the effect on the measured cross section depends on the detector acceptance and the experimental cuts applied. Real photon emission from the electron can be divided into three characteristic experimental signatures

- Initial State Radiation (ISR), where the radiated photon is collinear with the incoming electron. If this photon is not detected, the effect is equivalent to a reduction of the electron beam energy, in consequence the kinematics are modified.
- Final State Radiation (FSR) denotes the emission of a photon collinear with the outgoing electron. Usually the electron and the photon are detected as only one electromagnetic object, in this case the correction is only small.
- For $Q^2 \approx 0$ there is a sizeable contribution from the QED-Compton process, which is characterised by a final state electron-photon system of large invariant mass. Here the photon can be measured as a separate object in the detector.

Equation (1.2) indicates the cross section for the inclusive process $ep \to eX$.

In the next sections the properties of the hadronic final state X are studied in more detail.

1.2.2 QCD Radiation

While the actual measurement is performed on hadrons, in a theoretical approach initially one deals with the level of partons. The hadronisation will be covered in section 1.2.4.

Fig. 1.2 shows several contributing diagrams to the production of final state partons: the lowest order diagram and first order QCD corrections to order α_s. The real corrections are labeled QCD Compton (❷) and Boson Gluon Fusion (❸), their relative frequency compared to the lowest order depends on the value of the strong coupling constant α_s.

In the QCD Compton case the scattering matrix element $\mathcal{M}$ for gluon radiation off a quark contains a factor $1/(p_q + p_g)^2$, with

$$(p_q + p_g)^2 = 2p_q \cdot p_g = 2E_q E_g(1 - \cos\theta_{qg}), \tag{1.3}$$

where p_q and p_g are the four-momenta of the quark and the gluon, respectively. Evidently $\mathcal{M}$ gets singular when $\theta_{qg} \to 0$ (collinear) or $E_g \to 0$ (soft). Integration over the phase space of the gluon yields

$$\mathrm{d}\sigma_{\mathrm{pQCD}} \sim \alpha_s \int \frac{\mathrm{d}E_g}{E_g} \frac{\mathrm{d}\theta_{qg}^2}{\theta_{qg}^2} \mathrm{d}\phi. \tag{1.4}$$

The perturbative inclusive cross section develops a double logarithmic divergence for a soft and collinear emission, which is partly canceled by virtual corrections (e.g. from ❹), while the remaining part is absorbed in parton densities. It can be shown that a similar argument holds for the boson gluon fusion graph as well as for the emission of more than one parton.

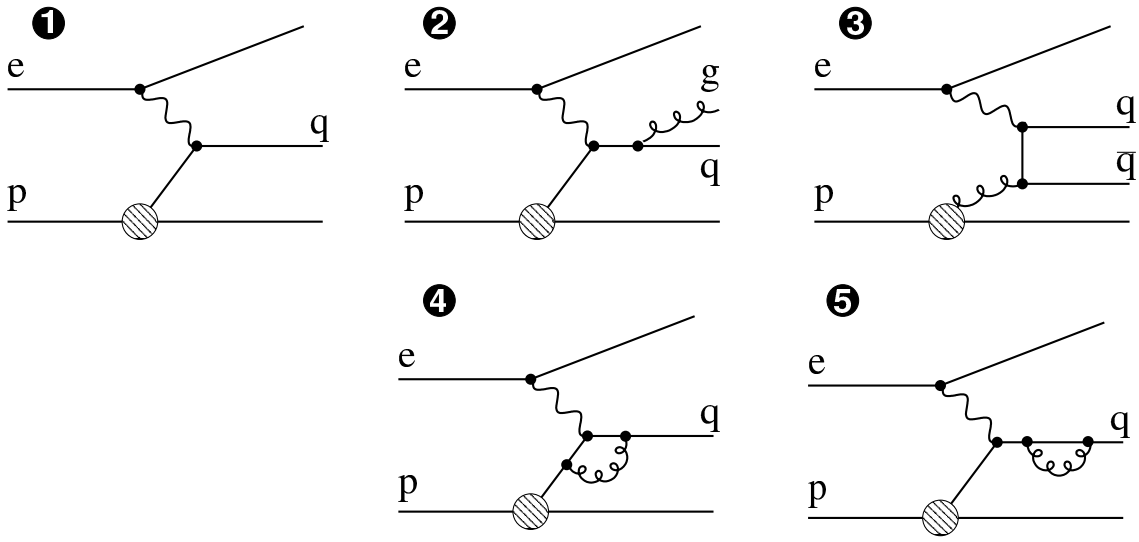

Figure 1.2: Diagrams for deep-inelastic ep scattering. Shown is the Born approximation (❶) and two diagrams of real corrections: QCD Compton (❷) and Boson Gluon Fusion (❸). In the lower row two virtual correction graphs (❹+❺) are depicted.

For a specific observable to be calculable in perturbative QCD it needs to be assured that the real and virtual correction terms cancel order by order. This is guaranteed for infrared and collinear (IRC) safe quantities. **Infrared safety** requires the observable not to change if an extra parton with vanishing energy $E \to 0$ is added to the particle configuration. A variable is **collinear safe** if it is invariant under a splitting of a single parton into two collinear ones, which carry in sum the original momentum. Any observable which is linear in the hadron momenta fulfills the IRC requirement.

Two extreme cases of QCD radiation can be distinguished.

a) Hard parton emissions, far away from the singular regions, lead to pronounced jet configurations. If n hard partons are present and nothing else, such a configuration is labeled the Born level of an n-jet event[1]. The cross section gets small with increasing n, because every additional jet is suppressed by another power of α_s.

b) On top of any given n-jet configuration there can be in addition soft-collinear emissions. The cross section for this is enhanced due to the singular behaviour mentioned above, resulting in a large number of accompanying soft partons.

[1] In DIS, events with n jets from the hard scattering are sometimes referred to as "$(n+1)$-jet" events, to underline that there is in general an additional jet from the proton remnant. In this work the remnant is only of minor importance, therefore the notation "n-jet" was found to be more descriptive.

Hard and soft QCD radiation is accounted for in different ways when calculating cross sections. Case a) is treated by the leading order (LO) term of the perturbative expansion in α_s, exact matrix elements are available in DIS up to α_s^3, corresponding to 4-jet cross sections in leading order [15]. Case b), the higher order correction to a given n-jet cross section, is more challenging to handle.

b1) It may appear straightforward to calculate the full matrix element simply to higher orders, unfortunately this task proves to be very difficult. For DIS the highest order available up to now is next-to-leading order (NLO) for 1-, 2- and 3-jet events. Care has to be taken that real and virtual parts of the corrections cancel, whereby two procedures are used: The phase space slicing method, implemented in MEPJET [16], and the subtraction method, which is used in DISENT [17], DISASTER++ [18] and NLOJET++ [15].

b2) A popular approximative approach is that of final state parton showers (PS): in the leading $\log 1/Q^2$ approximation of QCD, described by the DGLAP equations [19, 20, 21] all orders of α_s are included. These parton showers are used in Monte Carlo event generators [22] to make up for otherwise missing higher orders.

b3) For specific observables, e.g. event shape variables, there are also resummations of logarithmically enhanced terms to all orders in α_s available. These terms can be added to fixed order calculations, in practice NLO, to get an improved prediction. The combination of the fixed order and resummed part of the calculation needs to be done in a specific matching scheme, to prevent double counting of terms. Resummations had always to be performed in tedious work by hand, for a single observable at a time. Only recently a generalised resummation, suitable for a large class of observables, has been presented [23].

Event shape variables can be understood as a measure how the geometric properties of the energy flow of an event differ from the Born level. To make clear what kind of Born level is referred to, the variables are labeled as "2-jet shapes", "3-jet shapes" etc. For $n \geq 1$, any $(n+1)$-jet event shape variable is defined to become zero in the n-jet Born limit, and is of order 1 if additional hard emission of type a) are present, e.g. in the case of an $(n+1)$-jet Born event.

While all event shape variables discussed in the present work are infrared and collinear **safe**, they are nonetheless **sensitive** to low energy emissions, therefore small deviations from the Born limit $0 < F \ll 1$ are observed for type b) emissions. The sensitivity of event shapes to QCD radiation, and consequently to the value of the strong coupling, makes it possible to perform α_s fits, either to mean values or distributions of shape variables. If event shapes are investigated as a function of the scale Q, the scale dependence of QCD can be studied.

1.2.3 Perturbative Calculations

The ingredients of perturbative calculations for event shape variables are both the fixed order contribution and the resummed part. This section briefly presents what is available for DIS, citing formulae from Refs. [24, 25].

Consider the cumulative cross section R of an event shape observable F normalised to the Born cross section σ_0:

$$R(F) = \int_0^F \frac{1}{\sigma_0} \frac{\mathrm{d}\sigma}{\mathrm{d}F}. \tag{1.5}$$

The normalised distribution can be obtained later by differentiating this expression with respect to F. A perturbative expansion of R in the strong coupling reads

$$R(F) = 1 + \sum_{n=1}^{\infty} c_n(F) \alpha_s^n, \tag{1.6}$$

where c_n is known from the $\mathcal{O}(\alpha_s^n)$ matrix element. In next-to-leading order this simplifies to

$$R_{\mathrm{NLO}}(F) = 1 + c_1(F)\alpha_s + c_2(F)\alpha_s^2. \tag{1.7}$$

In general, this describes well the inclusive phase space region, where F is of the order of 1. In order to perform a fit of α_s to measured data, a prediction of at least NLO precision is needed.

The region of $F \ll 1$ is dominated by soft and/or collinear partons, where the corresponding divergences lead to incomplete cancellations of real and virtual corrections. This results in a bad convergence of the series (1.6). Numerically each power of the coupling is accompanied by up to two powers of a large logarithm $L = \log(1/F)$, such that the series contains terms $(\alpha_s \log^2 1/F)^n$, which need to be resummed to all orders. Therefore a reorganisation of the expansion is necessary, making use of L as a second variable for the expansion.

Many observables have the property to exponentiate, which means that it is possible to write:

$$R(F) = \exp\left(\sum_{n=1}^{\infty} \alpha_s^n \left(\sum_{m=0}^{n+1} c_{nm} L^m + \mathcal{O}(F) \right) \right). \tag{1.8}$$

Leading logarithms (LL) are now terms with $m = n + 1$, while next-to-leading logarithms (NLL) are those with $m = n$. The resummed result in next-to-leading logarithm accuracy is

$$R_{\mathrm{NLL}}(F) = (c_0' + \alpha_s c_1') e^{Lg_1(\alpha_s L) + g_2(\alpha_s L)}. \tag{1.9}$$

To allow comparisons with data over the full range of F, it is necessary to add both, the fixed order and the resummed part, and remove the terms which would be

counted twice, being the $\mathcal{O}(\alpha_s)$ and $\mathcal{O}(\alpha_s^2)$ terms of the resummed result. A simple matching of R itself does not work, because the result does not vanish for $F \to 0$, therefore the logarithm of the cross section, $\log R$, is used instead. The final result for "log R-matching" has the form

$$R_{\text{matched}} = R_{\text{NLL}} e^{\alpha_s\left(R^{(1)}_{\text{NLO}} - R^{(1)}_{\text{NLL}}\right) + \alpha_s^2\left(R^{(2)}_{\text{NLO}} - R^{(2)}_{\text{NLL}} - \frac{1}{2}(R^{(1)}_{\text{NLO}})^2 + \frac{1}{2}(R^{(1)}_{\text{NLL}})^2\right)}, \tag{1.10}$$

where $R^{(n)}$ is a term to order $\mathcal{O}(\alpha_s^n)$.

There are other valid matching schemes available, hence an ambiguity in the result is introduced, which is generally small and contributes to the uncertainty of the prediction.

In a more realistic discussion than presented here, the hadronic initial state has to be accounted for. This can be achieved if the scalar constants c and g become matrices which operate on vectors of parton densities. Moreover, depending on the event shape variable, there may be more singularities than $F = 0$.

1.2.4 Non-Perturbative Calculations

One important process in the description of event shapes in DIS has been neglected in the discussion so far: the transition from the final state partons to experimentally observable hadrons, labeled hadronisation.

Perturbative QCD breaks down if the relevant scale approaches values as low as $\Lambda_{\text{QCD}} \approx 200$ MeV. If one extrapolates into this non-perturbative regime, a pole is reached at $\mu_r = \Lambda_{\text{QCD}}$. A diverging coupling reflects the confinement of the partons at low scales, where quarks and gluons cannot be treated as free particles.

The hadron masses which determine the scale of hadronisation are of the order of Λ_{QCD}, rendering the application of perturbative QCD impossible. It is interesting to note that QCD is unique among the theories of the standard model in that both, strong and weak coupling regimes, are relevant to current high energy experiments.

All event shapes variables are subject to the non-perturbative effects of hadronisation, therefore the calculations in the previous section are incomplete and need to be corrected. The corrections can be determined by Monte Carlo models like the Lund string fragmentation. For many applications these models lead to a reasonable description, however the interface between perturbative and non-perturbative processes is unclear and there are usually unphysical parameters which need to be tuned.

Due to the semi-inclusive nature of event shapes it is not actually needed to describe every feature of the hadronic final state, e.g. hadron multiplicities and the frequency of individual hadron species. Because of this, it is tempting to make use of an analytical approach.

It can be inferred from various data analyses that non-perturbative corrections in general are suppressed by a power law of the form $(\Lambda_{\text{QCD}}/Q)^p$. In the case of event shapes the leading corrections are proportional to $1/Q$.

The power law behavior of the corrections can be described if a hypothetical effective coupling α_{eff}, valid for long distances respective low scales is introduced [26]. For large scales the effective coupling has to align with the usual renormalised coupling $\alpha_s(Q)$, whereby the matching is made at a scale μ_I, which is conventionally chosen to be 2 GeV.

In the language of Feynman diagrams the effective coupling corresponds to the introduction of massive gluon loops. This ansatz results in only one single non-perturbative parameter, being the first moment of the coupling:

$$\alpha_0(\mu_I) = \frac{1}{\mu_I} \int_0^{\mu_I} \alpha_{\text{eff}}(k) \mathrm{d}k. \tag{1.11}$$

Power corrections for event shape variables in DIS have been calculated to one-loop accuracy in [7] and to two-loop accuracy in [27]. For the differential distributions the power correction results in a shift

$$\frac{1}{\sigma_{\text{tot}}} \frac{\mathrm{d}\sigma(F)}{\mathrm{d}F} = \frac{1}{\sigma_{\text{tot}}} \frac{\mathrm{d}\sigma^{\text{pQCD}}(F - a_F \mathcal{P})}{\mathrm{d}F} \tag{1.12}$$

where a_F is of order one and can be calculated perturbatively. The power correction term $\mathcal{P}$ is assumed to be universal for the observable and the process.

The mean value of an event shape is then modified by non-perturbative effects by an additive constant

$$\langle F \rangle = \langle F \rangle_{\text{pQCD}} + a_F \mathcal{P}, \tag{1.13}$$

with the same coefficient a_F and power correction $\mathcal{P}$ as for the distribution.

The power correction $\mathcal{P}$ is proportional to $1/Q$ and evaluated to be

$$\mathcal{P} = \frac{16}{3\pi} \mathcal{M} \frac{\mu_I}{Q} [\alpha_0(\mu_I) - \alpha_s(Q) - \frac{\beta_0}{2\pi} \left(\ln \frac{Q}{\mu_I} + \frac{K}{\beta_0} + 1 \right) \alpha_s^2(Q)]. \tag{1.14}$$

The coefficient $\beta_0 = 4\pi b = 11 - 2/3 n_f$, where n_F is the number of active flavours, is taken from the perturbative expansion of the renormalisation group equation (5.1). The Milan factor $\mathcal{M} \simeq 1.49$ assures the universality at the two-loop level [27]. Finally, K accounts for the difference between the $\overline{\text{MS}}$ and the CMW renormalisation scheme

$$\alpha_{s,\text{CMW}} = \alpha_{s,\overline{\text{MS}}} + \frac{K}{2\pi} \alpha_{s,\overline{\text{MS}}}^2, \tag{1.15}$$

and is defined as

$$K = \frac{67}{6} - \frac{\pi^2}{2} - \frac{5}{9} n_F. \tag{1.16}$$

The quoted universality of the power corrections has been tested experimentally, for mean values compatibility with $\alpha_0(\mu_I = 2\,\text{GeV}) = 0.5$ on the 20% level was found in DIS as well as in e^+e^- annihilation. While comparable conclusions were drawn in an analysis of differential distributions in e^+e^- annihilation [28], fits to distributions in DIS had not yet been carried out, and are subject of the present thesis.

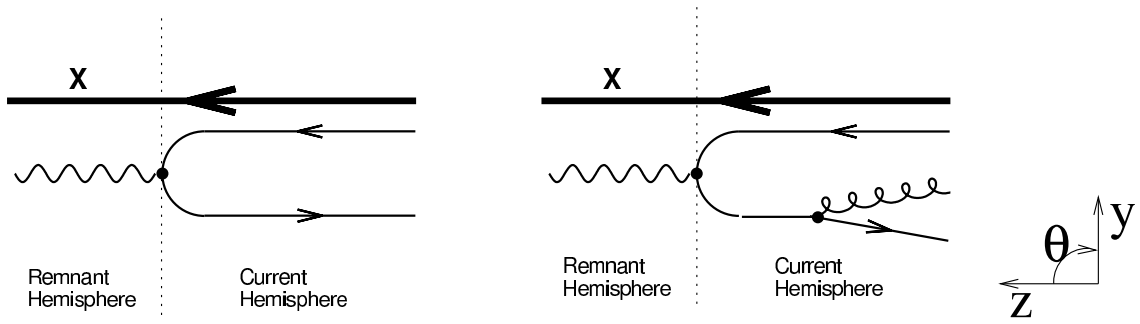

Figure 1.3: Scattering in the Breit frame of reference. Born level (left) and QCD Compton (right). Transverse momenta are only generated through QCD radiation and are balanced.

1.2.5 The Breit Frame of Reference

In addition to the hadronic flow from the hard scattering, there are also hadrons in the final state stemming from the dissociation of the hit proton, which occurs at a lower scale of $\mathcal{O}(m_P) < Q$, hence it is necessary to separate this proton remnant from the event. In the 1-jet Born level the separation is maximised in the Breit frame of reference, see Fig. 1.3, defined by $2x\vec{p} + \vec{q} = 0$, where x is the Bjørken scaling variable, $\vec{p}$ the momentum of the proton and $\vec{q}$ the momentum of the exchanged boson. In this frame the momentum transfer q is purely space like and anti parallel to the proton direction. The z-axis in the Breit frame is defined to coincide with the proton-boson axis, the proton going to the +z-direction, the photon or Z^0 to the -z-direction. In practice, the Breit frame transformation is calculated with the help of the experimentally accessible kinematic quantities Q^2 and y.

Particles building the remnant are almost collinear to the proton direction, hence the hemisphere defined by pseudo-rapidity[2] $\eta > 0$ is labeled the remnant hemisphere (RH). The incoming quark is exactly back scattered at the boson of virtuality Q into the current hemisphere (CH), such that the Breit system of reference is sometimes called the "brick wall frame". The current hemisphere can be identified with one half of an e^+e^- annihilation event with a center of mass energy $\sqrt{s} = Q$.

Event shapes are usually defined for momenta in the current hemisphere (CH, $\eta < 0$) alone, or in a more general way to some restricted region in pseudo-rapidity, e.g. $\eta < 3$. In the Born picture there is just the struck quark in the CH, collinear to the -z axis. Additional QCD radiation in the final state generates transverse momenta in the event. Contrary, in the laboratory frame the recoil from the scattered electron in general makes for transverse momenta not caused by the hard QCD matrix element.

Multiple QCD radiation may lead to particles from the hard subprocess leaking into the remnant hemisphere, causing an imperfect separation and an energy loss

[2]The pseudo-rapidity is defined as $\eta = -\log(\tan\theta/2)$ with θ the polar angle w.r.t to the z-axis.

in the current hemisphere. This feature of event shapes in DIS poses a problem for theoretical calculations of some event shape variables, which, however, has been solved. A better separation (of the current region from the proton remnant) than with the Breit frame of reference is only possible if a more detailed knowledge of the hadronic final state structure is available.

1.3 Definition of the Event Shape Variables

Many event shapes variables have been defined so as to be sensitive to different aspects of QCD dynamics, e.g. the longitudinal or transverse development of jets. They all have in common to be dimensionless, positive definite quantities and most of them fulfill the requirement of infrared and collinear safety. The variables used in this work can be assigned to three categories: 2-jet event shapes, 3-jet event shapes and jet rates.

1.3.1 2-Jet Event Shapes

The 2-jet variables studied in this work are two kinds of thrust (τ and τ_c), the jet broadening B, the jet mass ρ and the C-parameter. These are defined for the particles in the current hemisphere (CH) alone, corresponding to a cut on the pseudo-rapidity in the Breit frame of $\eta < 0$.

Thrust $\tau = 1 - T$ measures the longitudinal momentum components projected onto the virtual boson axis

$$T = \frac{\sum_{h \epsilon CH} |\vec{p}_{z,h}|}{\sum_{h \epsilon CH} |\vec{p}_h|}. \tag{1.17}$$

Thrust $\tau_C = 1 - T_C$ uses the direction $\vec{n}_T$ which maximizes the sum of the longitudinal momenta of all particles in the current hemisphere along this axis

$$T_C = \frac{\sum_{h \epsilon CH} |\vec{p}_h \cdot \vec{n}_T|}{\sum_{h \epsilon CH} |\vec{p}_h|}. \tag{1.18}$$

The **jet broadening** B measures the scalar sum of transverse momenta with respect to the virtual boson axis

$$B = \frac{\sum_{h \epsilon CH} |\vec{p}_{\perp h}|}{2 \sum_{h \epsilon CH} |\vec{p}_h|}. \tag{1.19}$$

The **jet mass** ρ_0 is defined in a way to not depend on hadron masses

$$\rho_0 = \frac{\sum_{h \epsilon CH} |p_h| - (\sum_{h \epsilon CH} \vec{p}_h)^2}{(2 \sum_{h \epsilon CH} |p_h|)^2}. \tag{1.20}$$

The C**-parameter** is defined as

$$C = \frac{3}{2}\frac{\sum_{h,i\epsilon CH} |\vec{p}_h||\vec{p}_i| \sin^2\theta_{hi}}{(\sum_{h\epsilon CH} |\vec{p}_h|)^2}, \tag{1.21}$$

where θ_{hi} is the angle between particle i and h.

It is important that the event shape variables are defined independently to hadron masses, because otherwise universality-breaking terms are introduced to the power corrections. Of the observables listed, only the jet mass was originally defined in a mass dependent way. The definition shown above treats the hadrons massless within the p-scheme, i.e. references to the particle energy E were replaced by the modulus of its 3-momentum $|\vec{p}|$. The normalisation is always performed with respect to the sum of momenta in the current hemisphere.

An event is only accepted, i.e. contributes to the 2-jet event shape distributions, if the energy in the current hemisphere exceeds some value $\epsilon_{\rm lim}$. This is necessary to ensure the all-order infrared and collinear safety of the observables, because higher order processes may lead to event configurations where the partons are scattered into the target hemisphere and the current hemisphere may be completely empty except for arbitrarily soft emissions. It is important to choose $\epsilon_{\rm lim}$ not to be too small a fraction of Q, we take

$$\sum_{h\in \rm CH} E_h \;\; > \;\; \epsilon_{\rm lim} = Q/10\,, \tag{1.22}$$

otherwise the event is ignored. This cut-off is part of the event shape definitions, the precise value is not critical [14].

The event shapes defined in the current hemisphere may be distinguished according to the event axis used. The definitions of τ and B employ momentum vectors projected onto the boson direction, while the others do not, like their counterparts in e^+e^- reactions. Explicit use of the boson direction implies sensitivity to radiation into the remnant hemisphere through recoil effects on the current quark [25].

For all five presented event shapes detailed calculations are available: a perturbative part at $\mathcal{O}(\alpha_s^2)$ + NLL precision, together with power corrections.

1.3.2 3-Jet Event Shapes

Interest has only recently moved to 3-jet event shapes in DIS, whereby the presented work shows the first measurements for two variables of this type, out-of-plane momentum $K_{\rm out}$ and azimuthal correlation χ. These event shapes are sensitive to large angle soft emissions, i.e. to emissions between hard jets, and are more geometry dependent than 2-jet event shapes. Because of this, the pseudo rapidity requirement is loosened to $\eta < 3$. The definition of $K_{\rm out}$ is taken from [29], the definition of χ from [30].

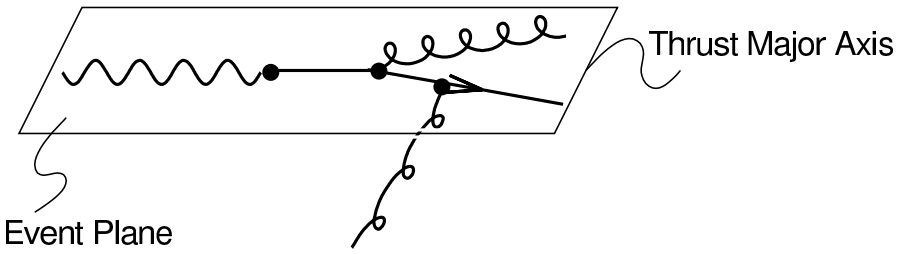

Figure 1.4: The definition of the out-of-event plane momentum $K_{\rm out}$ makes use of an event plane spanned by the virtual boson momentum and the thrust major axis. Partons pointing out of these plane contribute to $K_{\rm out}$.

The **out-of-event plane momentum** is sensitive to momenta perpendicular to a suitably defined event plane, and can only be non-zero for configurations with at least three partons:

$$K_{\rm out} = \sum_h{}' |p_h^{\rm out}|. \tag{1.23}$$

Here $p_h^{\rm out}$ is the out-of-plane momentum of the hadron h with the event plane defined as the plane formed by the virtual boson momentum $\vec{q}$ in the Breit frame and the unit vector $\vec{n}$ which enters the definition of thrust major:

$$T_M = \max_{\vec{n}} \frac{1}{Q} \sum_h{}' |\vec{p}_h \cdot \vec{n}|, \qquad \vec{n} \cdot \vec{P} = 0. \tag{1.24}$$

The actual event shape which is investigated in this work is $K_{\rm out}/Q$, the out-of-event plane momentum normalised to Q. The sum indicated by $\sum_h{}'$ extends over all hadrons with pseudo rapidity in the Breit frame η less than 3. The observable $K_{\rm out}$ is similar to the out-of-plane jet shape studied in e^+e^- annihilation, where the event plane is defined by the thrust and thrust major axes [31].

The calculations in [29] are carried out for small values of $K_{\rm out}$, i.e. near to planar parton configurations and are inspired by the following scenario, see Fig. 1.4: Two relatively hard partons with transverse momentum p_t lie back-to-back in the Breit frame and span necessarily a plane together with the virtual photon. The momentum of a third, possibly soft parton is then probed with the $K_{\rm out}$ variable. For the event plane to be well defined, only events with sufficiently high $p_t \sim Q$ have to be selected, which is accomplished by a cut on the 2-jet resolution y_2 defined by the k_t clustering algorithm: $0.1 < y_2 < 2.5$. For the definition of y_2 see section 1.3.3.

An observable which is well known in e^+e^- environments is the energy-energy correlation (EEC), which is a function of the polar angle between pairs of hadrons weighted by their energy. A similar quantity has been adopted to DIS:

The **azimuthal correlation** involves the azimuthal angles between all hadron pairs h and i in an event:

$$\chi \;=\; \pi - |\phi_h - \phi_i|, \quad \text{weighted by} \quad w = \frac{p_{th} p_{ti}}{Q^2}, \tag{1.25}$$

where the azimuth in the Breit frame of hadron h is denoted by ϕ_h. The azimuthal correlation is the only variable presented in this work, where not a plain (normalised) differential cross section is determined. In this case a single event contributes not only one value χ to the differential distribution, but instead every pair of hadrons enters with a weight w. The restrictions with respect to η and y_2 apply in the same way like for the out-of-plane momentum K_{out}.

While resummed calculations for K_{out} and χ have been performed [29, 30], the matching to NLO and power corrections are not yet available. Hence in this work comparisons to leading order Monte Carlo programs only are drawn.

1.3.3 Jet Rates

Jet rates belong not to the class of classical event shapes, although they exhibit many similar features. The main difference being that for the separation of the proton remnant no fixed cut in η is made, instead the particles entering further calculation are determined dynamically by the jet algorithm.

Jet definitions were introduced in the first place to get observables which resemble on detector level the underlying hard parton momenta as closely as possible. To achieve this, adjacent final state momenta, determined by some distance measure are consecutively merged. There are so called "cone" and "cluster" jet definitions, where in this work only the latter will be used.

Cluster algorithms make use of a resolution parameter y_{cut}, which determines the minimal separation of partons to resolve them as two different jets. For the definition of a jet cross section, the resolution y_{cut} stays fixed and the jet algorithm calculates for any event the number and momenta of the identified jets.

In the case of jet rates it is the other way around: the number of jets to look for is fixed, and the appropriate value of y_{cut} is determined for any event by the algorithm. The n-jet rate is then defined as the distribution of y_{cut} for the transition of a n- to a $(n-1)$-jet configuration, normalised to the total cross section. While jet cross sections are relatively insensitive to soft radiation, this is not the case for jet rates, a feature also found for the "classical" event shapes.

The jet definition used in this work is the k_t clustering algorithm in its exclusive mode [32, 33], where two distance measures are introduced: one for distances between two particles, y_{ij}, and another for the separation of each particle from the remnant, y_{ir}:

$$y_{ij} = \frac{2\min(E_i^2, E_j^2)(1 - \cos\theta_{ij})}{Q^2}, \tag{1.26}$$

$$y_{ir} = \frac{2E_i^2(1-\cos\theta_i)}{Q^2}. \tag{1.27}$$

The pair with the minimal y_{ij} or y_{ir} value of all combinations is selected to either form a new pseudo-particle or to assign the particle i to the remnant. The procedure is repeated until a certain number of jets n is found. Since the proton remnant is treated explicitly by the jet algorithm, all hadrons of both hemispheres enter the calculation. The event shape variables y_n are defined as the minimum of y_{ij} and y_{ir} where the transition of n- to $(n-1)$-jets occurs. In the present analysis distributions of y_2, y_3 and y_4 are measured.

Fixed order calculations in NLO are available for y_2 and y_3, while for y_4 the present state of the art is LO accuracy. Resummation for these observables should be possible in the near future with a generalised resummation program [23]. Power corrections could not yet successfully applied to jet rates, on the other hand hadronisation corrections are known to be much smaller compared to what is known from classical 2-jet event shapes.

Chapter 2

HERA and the H1 Detector

The previous chapter showed that deep inelastic scattering is a fruitful process for studying the various aspects of the standard model and in particular of QCD. Now, what are the experimental setups needed to produce DIS events? Obviously at least one kind of particles, leptons or hadrons has to be accelerated. Because there is no dense material out of leptons alone, one is left with two possibilities.

- Accelerate leptons on hadronic matter (fixed target)
- Bring two high energy beams, out of leptons and hadrons, into collision (collider, storage ring).

However, the kinematics of fixed target experiments are always restricted to the high x, low Q^2 region. In 1992 DESY, until that time successful in building and operating e^+e^- storage rings, started the operation of the first electron-proton storage ring, HERA, in order to open the door to high Q^2, low x DIS physics.

2.1 The Electron Proton Storage Ring HERA

HERA consists of two separate accelerators, housed in one common tunnel of 6.3 km circumference.

- The electron machine is operated with normalconducting magnets and partly with superconducting RF cavities, where the maximum beam energy amounts to 27.6 GeV at currents of up to 50 mA. It is possible to switch between electron and positron operation.
- For the proton machine superconducting magnets and normalconducting RF cavities are used. From 1992 to 1997 the proton storage energy was fixed to 820 GeV, which could then be raised to 920 GeV. The highest proton currents achieved are 100 mA.

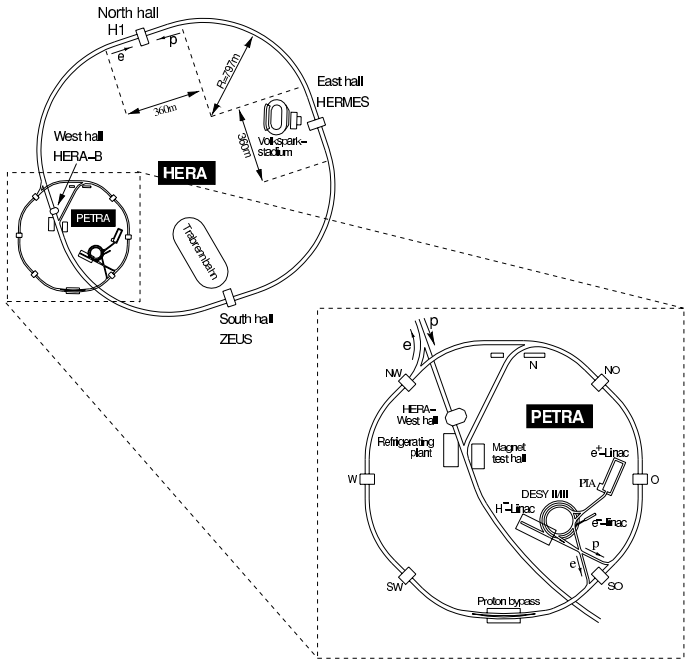

Figure 2.1: The storage ring HERA (left) together with the preaccelerators (right).

The beam pipes of both accelerators are solely connected at two interaction regions, where a sophisticated design assures that the much stronger bending magnets for the protons do not interfere with the electron beam line. Collisions between electron and proton bunches occur at a rate of 10 MHz and at a center of mass energy of 318 GeV (301 GeV) for a proton energy of 920 GeV (820 GeV).

Around the interaction regions the multi purpose detectors H1 and the ZEUS are placed, in order to measure the particles emerging from the scattering process. The highest luminosity measured by H1 amounts to $\mathcal{L} = 1.8 \cdot 10^{31}\,\mathrm{cm}^2\mathrm{s}$.

Both beam lines are also used for fixed target experiments, concurrently with the collision operation: There is the HERMES experiment, studying the scattering of longitudinally or transversally polarised electrons of 27.6 GeV energy on a resting target of polarised hydrogen or deuterium [34]. The HERA-B experiment measures collisions of 920 GeV protons with the nuclei of target wires [35].

Figure 2.1 shows on the left hand side the layout of HERA with the four experiments and on the right hand side the preaccelerator complex in a magnified view.

2.2 The H1 Detector

Purpose of the H1 detector is to measure cross sections of a broad spectrum of ep reactions. The features most important for the presented analysis are the measurement of the scattered electron and the hadronic final state. A full description of H1 can be found in [36, 37]. Since commissioning in 1992 the detector was subject to several modifications, the description given below refers to the setup of 1996-2000, where the majority of the data used in the presented analysis was taken.

To identify neutral current or charged current reactions, it is necessary to separate the scattered lepton from the rest of the event and determine its momentum. Electrons can directly be measured with tracking devices and high granularity calorimetry, as long as a good lepton/hadron separation is achieved. Neutrinos, on the other hand, have too a small reaction cross section in an apparatus of the size of H1, and can therefore not be directly measured. Their identification uses the attribute of apparent missing energy in the calorimeters, taken away by the undetected neutrino. This approach needs calorimetry as hermetic as possible.

In addition to the scattered lepton, many more particles may be produced in the reaction. Inelastic reactions are characterised by the occurrence of many hadrons, mostly charged pions. In the optimal case, the identities and four momenta of all reaction products are determined by the detector. Momenta and particle identification of long lived charged particles can be achieved in a drift chamber by measuring tracks and their differential energy loss $\mathrm{d}E/\mathrm{d}x$. Though tracking devices have two drawbacks: they are insensitive to neutral particles and their momentum resolution gets worse for increasing momenta. Both issues are addressed when the tracking information is complemented by electromagnetic and hadronic calorimetry.

To calculate from an observed number of events the corresponding cross section, it is necessary to determine the luminosity at the interaction point. This is done via measurement of the event rate from a reference reaction with well known cross section. At HERA the Bethe-Heitler process $ep \to ep\gamma$ serves as the reference.

Unfortunately, most of the reactions occurring within the acceptance of the H1 detector are background processes from interactions of the beams with resting matter. This can be beam-gas, i.e. a beam particle hitting a nucleon of the remaining gas molecules in the vacuum beam pipe, or beam-wall, i.e. an off-momentum beam particle getting out of the aperture of the accelerator and hitting the material of the beam pipe. To prevent background events from flooding the data stream, one needs fast trigger electronics which decides in real time, based on raw data, whether an event is likely caused by ep scattering or by some background process. In addition the trigger logic is programmed to accept mostly events from interesting low cross section processes.

Figure 2.2 gives an overview of the central parts of the H1 apparatus. The main active components can de divided into calorimetry and tracking.

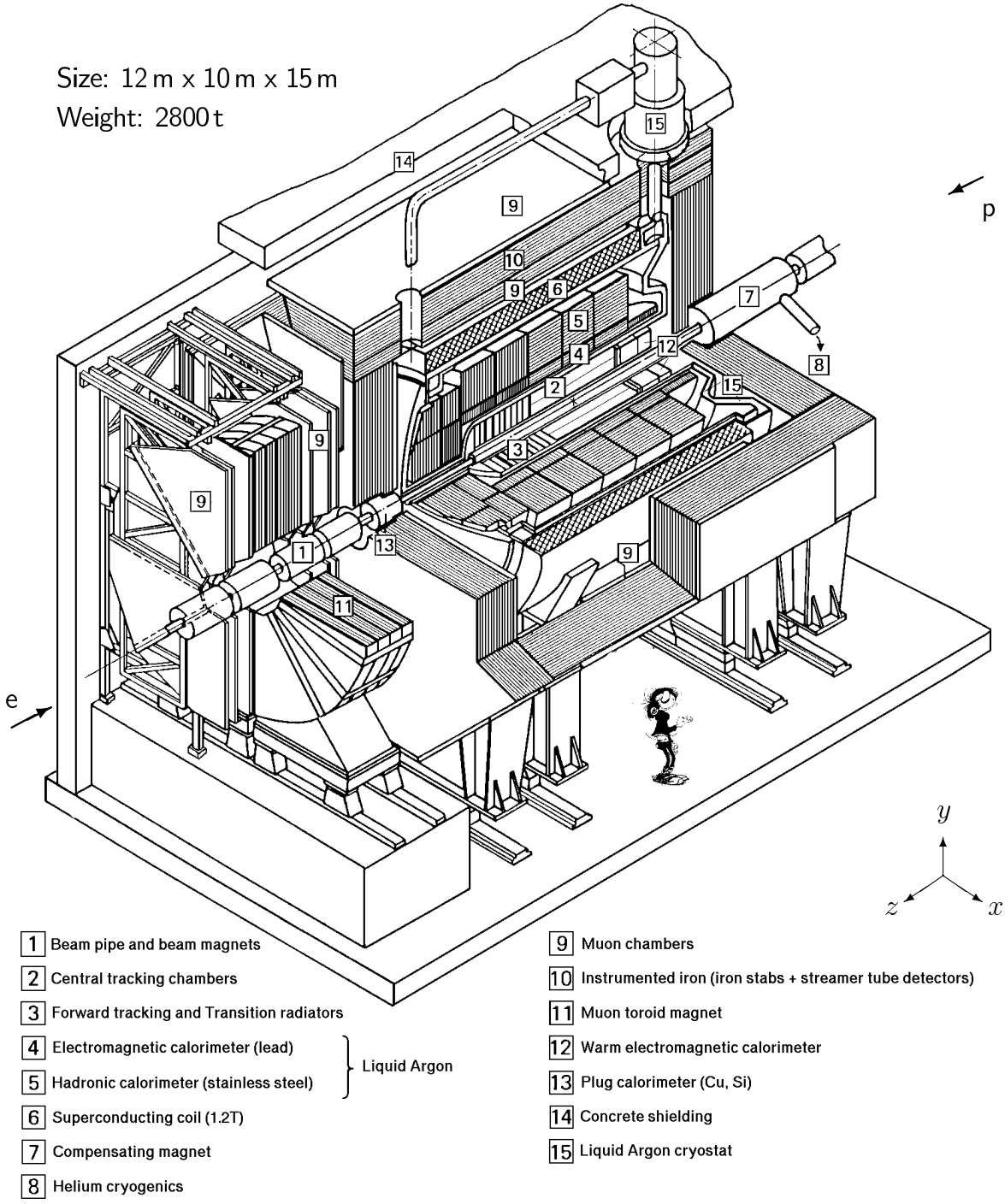

Figure 2.2: The central region of the H1 detector.

2.2.1 Calorimetry

The liquid argon sampling calorimeter (LAr) covers the polar angle interval ($4° \leq \theta \leq 154°$). It consists of a lead/argon electromagnetic section [4] and a stainless steel/argon section for the measurement of hadronic energy [5]. The lepton energy uncertainty in the LAr calorimeter varies between 1% in the backward region and 3% in the forward region, while the systematic uncertainty of the hadronic energy amounts to 2% for the present analysis. The depth of the electromagnetic section corresponds to 20-30 radiation lengths, depending on the polar angle of the energy deposition. Accordingly, the hadronic section represents 4.5-8 hadronic interaction lengths.

The LAr is non-compensating, i.e. pions generate a smaller signal than electrons of the same energy. Therefore a weighting technique is applied to the electromagnetic and the hadronic components of the energy deposition, in order to account for this non-compensating nature of the calorimeter.

In the presented analysis the LAr is utilised to identify electrons, which exhibit compact, high energetic clusters in the electromagnetic part, together with only small deposits in the hadronic part. Between the single active volumes of the LAr there are small gaps, called "cracks", leading to inferior calibration around these areas. These cracks are evenly and symmetrically distributed over the solid angle and are excluded for electron measurements in this analysis, resulting in a small acceptance loss, which is accounted for in the detector correction.

The LAr is used to measure the energy of the hadronic final state particles as well. Hadron clusters are less compact than electron clusters and extend in gerneral over many calorimeter cells. The capacity of any single cell generates noise, which may get sizable when summed up over all cells of a hadronic cluster candidate. In order to reduce such fake clusters, a noise suppression is performed, with the drawback that also low energy particles cannot be measured by the calorimeter anymore. Here the combination with data from the tracking devices improves the situation.

While the LAr is the main calorimeter of H1, there are few more devices which extend the acceptance of the experiment: In the backward region ($153° \leq \theta \leq 177°$) energy is detected by a lead/scintillating fibre Spaghetti-type calorimeter ([12] SPACAL), while the very forward region ($0.7° \leq \theta \leq 3.3°$) is covered by a copper/silicon calorimeter ([13] PLUG). Hadronic showers of very high energy may not be completely contained in the hadronic LAr, therefore part of the instrumented iron ([10] Tail Catcher) is also equipped with calorimetric readout.

Finally, compact calorimeters (Taggers) are set up long way off in the tunnel, in order to detect photons and electrons collinear to the electron beam line. This way photo production events, DIS with initial state radiation and Bethe-Heitler reactions can be identified.

2.2.2 Tracking

The central tracking devices (2 CTD) are situated within a solenoidal magnetic field of 1.2 T, in order to determine the transverse momentum of charged particles by their bending radius. The main tracking detector is a large jet chamber (CJC), which covers the polar angles $25° \lesssim \theta \lesssim 165°$. The CJC is used to reconstruct tracks from charged particles, which tell again the transverse momentum p_t and the particles direction θ and ϕ with respect to the vertex. The p_t resolution amounts to $\sigma_p/p^2 = 5 \cdot 10^{-3}\,\mathrm{GeV}^{-1}$. Two z-drift chambers in the central region improve the θ measurement of reconstructed tracks.

In the presented analysis, the central trackers are used to identify electrons by demanding a track pointing to an electromagnetic cluster in the LAr. The CTD also supplement the hadronic measurement by means of combined objects, build out of calorimeter clusters and tracks. Precise timing information from the CJC is used to suppress non-ep background.

Proportional chambers in the central and forward region provide already on the first trigger level timing and vertex information, allowing to suppress non-ep background.

The forward tracker modules (3 FTD) are used to identify tracks with $5° \lesssim \theta \lesssim 25°$, while in the backward region $153° \leq \theta \leq 177°$ a drift chamber improves the angular resolution of the SPACAL.

Silicon micro vertex detectors improve the reconstruction of the primary event vertex and allow to identify secondary vertices which may occur when heavy quarks are produced in the ep reaction.

Penetrating muons are measured by two dedicated systems for the central (10 CMD) and the forward (9 FMD) region.

2.3 Event Simulation with Monte Carlo Methods

H1, as any measuring device, is subject to imperfections which affect the measurements made. These are e.g. inefficiencies, limited resolutions and restricted acceptances, which are also in general time dependent. To make the results independent of such detector effects and to allow comparisons with other experiments, corrections are applied to the data.

Detector corrections can be determined with the help of computer simulations, which are carried out in two steps. Firstly, events stemming from the physical process under study are generated by a Monte Carlo program. Four vectors are given for particles after hadronisation, therefore an event at this stage is called the **hadron level** (or generator level). The event is then fed into the detector simulation H1SIM, which models the response of the detector components and the readout. H1SIM is based on GEANT [38] and is used in this work in its "fast" mode, where electromagnetic showers are not simulated in detail, but parametrised. The result

are Monte Carlo events on **detector level**, which in the ideal case have the same properties as measured ones. If the observables on detector level are well described by the Monte Carlo, it is plausible to assume that also the difference between hadron and detector level is similar for data and Monte Carlo. This difference can then be used to extract the detector correction, which applied on the data, yield the measurement on hadron level.

Depending on the method to determine the detector correction, it is not necessary to have a Monte Carlo generator which describes every detail of the studied physical process, it is more important that the detector simulation is reliable. It is a common practice to utilise two different Monte Carlo generators for the detector corrections and take their difference as the model uncertainty, which contributes to the systematical error.

In the presented analysis the Monte Carlo generators RAPGAP 2.08 [39] and DJANGOH 1.2 [40] are used for detector and QED radiative corrections. RAPGAP has the ability to generate deep inelastic scattering and diffractive events. The hard scattering includes processes with two outgoing partons, initial and final state parton showers in leading log approximation take account of the QCD cascade. Parton density functions of the proton are taken from the CTEQ5L [41] set, included in the PDFLIB 8 [42, 43] package. The hadronisation is treated with the Lund string model, QED radiation to $\mathcal{O}(\alpha)$ is calculated with HERACLES [44].

DJANGOH shares many properties with RAPGAP. The main difference lies in the model of the QCD cascade, where for this work RAPGAP was used with parton showers (MEPS) from LEPTO 6.5 [45], while in DJANGOH the color dipole model (CDM) of ARIADNE 4.08 [46] was employed.

The number of events simulated with both Monte Carlos is in every part of the phase space at least four times that of the data, at high Q^2 much larger.

In addition to the neutral current DIS process, several background reactions were studied with the help of special Monte Carlo generators. Photo production events were generated with PYTHIA 6.1 [47] for the direct and the resolved subprocess separately, corresponding to an integrated luminosity of $\mathcal{L}_{\text{int}} = 100\,\text{pb}^{-1}$. A charged current DIS sample has been produced with DJANGOH 1.2 ($\mathcal{L}_{\text{int}} = 2700\,\text{pb}^{-1}$). While inelastic QED Compton scattering is included in RAPGAP and DJANGOH and hence already included in the detector correction, the elastic QED Compton component is still missing, and was therefore generated with WABGEN [48] ($\mathcal{L}_{\text{int}} = 630\,\text{pb}^{-1}$). Photon-photon reactions into electron pairs have been generated with the GRAPE Monte Carlo [49] ($\mathcal{L}_{\text{int}} = 3000\,\text{pb}^{-1}$). Finally, a $W^{\pm}$ production sample, where the weak boson decays into leptons, was simulated with EPVEC [50] ($\mathcal{L}_{\text{int}} = 1000\,\text{pb}^{-1}$).

Chapter 3

Data Selection and Reconstruction

The following sections describe how the event sample on which this work is based on is extracted from the bulk of H1 events. Measurement of event shape variables rely on the determination of the hadronic final state, which is therefore discussed in more detail.

3.1 Selection Criteria

The presented analysis is based on data taken with the H1 detector during the years 1995 to 2000, corresponding to an integrated luminosity of $106\,\mathrm{pb}^{-1}$. Since the operating mode of the HERA accelerator changed within this period, the data set is divided into three subsets, see Tab. 3.1. A preselection discards exceedingly small runs, and requires all major detector components to be operational.

From the recorded events a **data selection** is build, with the following requirements.

- The sample has to consist of neutral current DIS events and to be mostly free of background.
- The event kinematics need to be precisely determined, especially for the boost to the Breit frame of reference, as well as for the differential measurement with respect to the scale Q.

No.	Year	E Proton	Lepton Type	E Lepton	Int. Luminosity
①	$1995-1997$	$820\,\mathrm{GeV}$	e^+	$27.6\,\mathrm{GeV}$	$30\,\mathrm{pb}^{-1}$
②	1998	$920\,\mathrm{GeV}$	e^-	$27.6\,\mathrm{GeV}$	$14\,\mathrm{pb}^{-1}$
③	$1999-2000$	$920\,\mathrm{GeV}$	e^+	$27.6\,\mathrm{GeV}$	$62\,\mathrm{pb}^{-1}$

Table 3.1: The three data subsets used in the analysis. The integrated luminosities are calculated with the run selection and high voltage corrections applied.

- The results of the event shape analysis are corrected for photon radiative effects, these corrections are precisely known from QED. Nevertheless, regions of phase space where the corrections are getting large should be avoided.

3.1.1 Phase space

First of all the phase space is chosen with respect to the kinematic variables Q^2 and y. It is known from [25] that the theory calculations for event shape distributions (in NLO/NLL precision including $1/Q$ power corrections) loose their predictive power for low scales ($Q \lesssim 20\,\text{GeV}$), because hadronisation effects get large. Therefore it is most promising to study the region of high Q, hence the lower bound in this analysis is set to

❑ $Q > 14\,\text{GeV}$ ($Q^2 > 196\,\text{GeV}^2$).

The upper limit of Q is given by the center of mass energy of the ep system (301 GeV or 318 GeV), where the event in the selection with the highest scale features $Q = 200\,\text{GeV}$. The region of high Q^2 NC DIS corresponds experimentally to an electron scattered into the LAr calorimeter, which acceptance begins at $Q^2 \approx 100\,\text{GeV}$. As a suitable trigger for electrons in the LAr the subtrigger ST67 is employed. It is sensitive to compact electromagnetic energy depositions together with a valid trigger signal from the central proportional chambers. Subtrigger ST67 is fully efficient for electron energies above 11 GeV [51], therefore the phase space for this analysis is restricted to

❑ $E_e > 11\,\text{GeV}$.

The final identification of electrons and their calibration is performed by the software module `QESCAT` at the reconstruction stage.

To fully constrain the phase space, also the interval in the kinematic variable y has to be specified. When determining the cuts on y, it is important to take into account the resolution of the kinematic reconstruction, which is hence briefly discussed in the following.

A measurement of either the scattered electron or the hadronic final state alone is sufficient to fix the kinematic variables of an event. However, if information from both objects is used, the redundancy helps to improve the experimental resolution. When dealing with the hadronic final state, it is convenient to define the following quantities

$$\Sigma = \sum_{\text{i}} (E_i - p_{z,i})\,, \quad p_{T,h} = \sqrt{(\sum_{\text{i}} p_{x,i})^2 + (\sum_{\text{i}} p_{y,i})^2}, \quad \gamma_h = 2\arctan\frac{\Sigma}{p_{T,h}}, \quad (3.1)$$

where the sums include all final state particles, except the scattered electron. In the case of only one collimated jet in an event, the inclusive hadronic angle γ_h denotes the polar angle of the hadronic system.

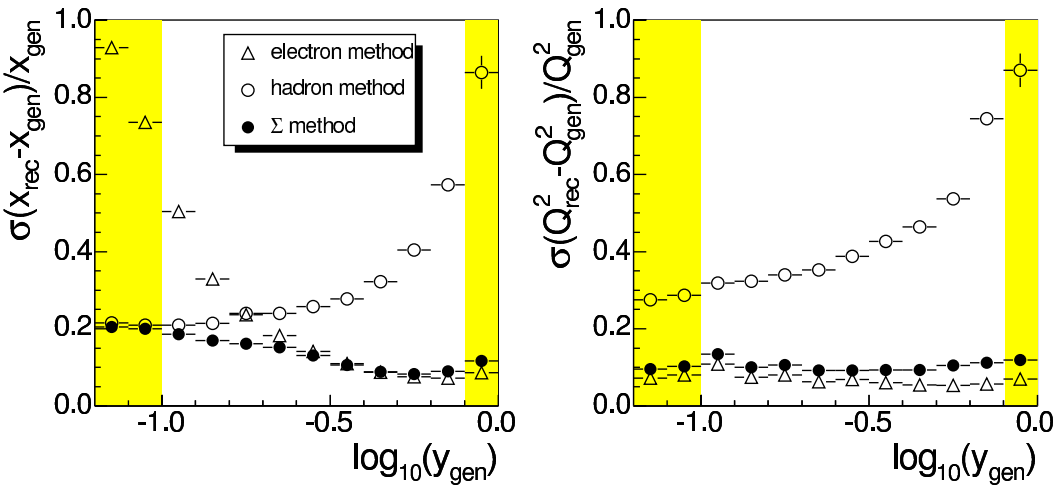

Figure 3.1: Resolution of the kinematic variables for three reconstruction methods, determined with RAPGAP. "gen" and "rec" subscripts denote variables on generator and detector level, respectively. The shaded areas are not part of the data selection.

Various methods exist to reconstruct the event kinematics, using either the electron or the hadronic final state or both. The **electron method** uses the polar angle θ_e and the energy E_e of the scattered electron

$$Q_e^2 = 2E_0E_e(1+\cos\theta_e), \quad y_e = 1 - \frac{E_e}{2E_0}(1-\cos\theta_e), \quad x_e = \frac{Q_e^2}{y_e s}, \tag{3.2}$$

with E_0 being the energy of the electron beam.

It is the hadronic final state alone, which is used in the hadron or **Jacquet-Blondel method**

$$Q_{\mathrm{h}}^2 = \frac{p_{T,h}}{1-y_{\mathrm{h}}}, \quad y_{\mathrm{h}} = \frac{\Sigma}{2E_0}, \quad x_{\mathrm{h}} = \frac{Q_h^2}{y_{\mathrm{h}} s}. \tag{3.3}$$

The **sigma method** combines variables from the scattered electron and the hadronic final state

$$Q_\Sigma^2 = \frac{(E_e \sin\theta_e)^2}{1-y_\Sigma}, \quad y_\Sigma = \frac{\Sigma}{\sum E - p_z}, \quad x_\Sigma = \frac{Q_\Sigma^2}{y_\Sigma s}. \tag{3.4}$$

Since the energy of the electron beam does not enter this calculation, the sigma method is less sensitive to initial state radiation (see also Section 1.2.1).

Fig. 3.1 shows the experimental resolution of x and Q^2 as a function of y for the three presented methods, determined with simulated events from the RAPGAP event sample, including QED radiative processes.

The electron method exhibits a worse resolution in x for low y, whereby for high y the hadron method degrades strongly. The sigma method appears optimal, because it results in the best x resolution of the three methods over most of the shown y range, only for high values of y the electron method performs slightly better.

It is obvious from the right hand side of Fig. 3.1 that there is no alternative to the electron method when reconstructing Q^2 in neutral current deep inelastic scattering. A combination of the electron and the sigma method, referred to as the **electron-sigma method**, leads to the best overall resolution and is hence used in this analysis for the boost to the Breit system of reference. It is defined as

$$Q^2_{e\Sigma} = Q^2_e, \quad y_{e\Sigma} = \frac{Q^2_{e\Sigma}}{x_{e\Sigma} s}, \quad x_{e\Sigma} = x_\Sigma. \tag{3.5}$$

Badly measured events can lead to unphysical values of x and Q^2, which in consequence result in an ill defined Lorentz boost. Because of this, a consistency requirement is applied:

- $Q^2_{e\Sigma} \leq s$ and $0 \leq x_{e\Sigma} \leq 1$.

A lower limit on the inelasticity

- $0.1 < y_{e\Sigma}$,

ensures a good resolution in $x_{e\Sigma}$. Moreover, this requirement selects events with high particle multiplicity in the central region of the detector, which assures a reliable reconstruction of the event vertex [52].

Fig. 3.2 shows the expected contribution of photo production events to the total data sample for low and high values of Q^2 separately. It demonstrates that the background events accumulate at values of high y_e. Hence a cut on y_e:

- $y_e < 0.8$,

yields a substantial reduction of the photo production background. For lower Q^2, this region is already kinematically suppressed by the $E_e > 11\,\text{GeV}$ cut. QED radiative events also give rise to high values of y_e and are hence reduced by this cut as well.

3.1.2 Data Quality Cuts

Now that the phase space is determined, it is necessary to further suppress remaining background. It has also to be checked if the Monte Carlo event samples from RAPGAP and DJANGOH, which contain only NC DIS events, describe the data reasonably well. In the following, several distributions of variables which are used for data quality cuts are pictured. The distributions of the data include statistical errors and are compared to the Monte Carlo predictions, which are normalised

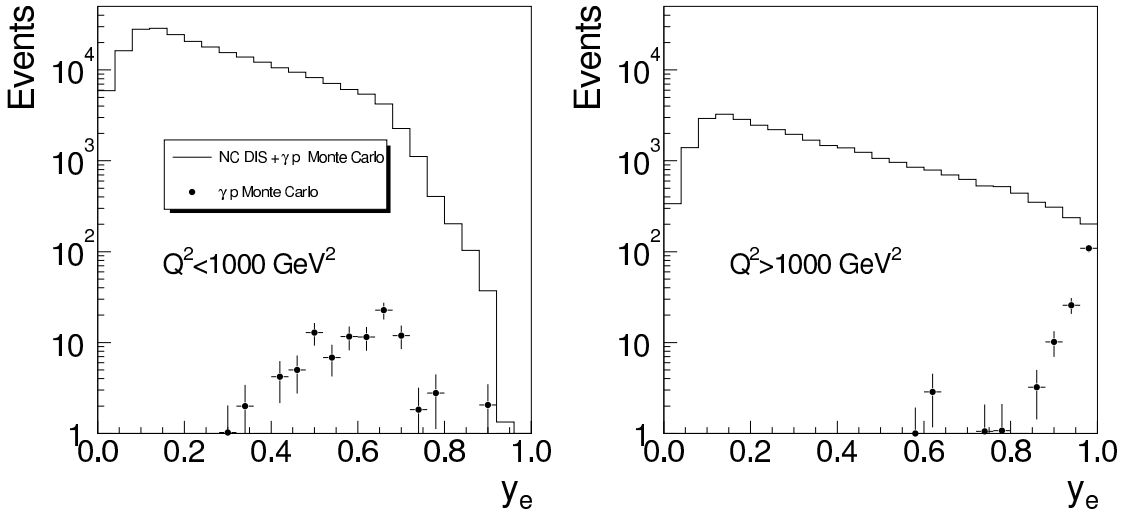

Figure 3.2: The photo production background, as predicted by PYTHIA. The normalisation is made to the integrated luminosity of the data. The photo production contamination rises with y_e, but is for lower Q^2 (left hand side) suppressed by the $E_e > 11\,\mathrm{GeV}$ cut.

to have the same integrated luminosity as the data. For each individual variable displayed, the cut condition on this variable is released, but in turn marked by a shaded area, whereby all other cuts are applied as usual.

Although for all three data sets ①-③ simulated event samples are available and used for the detector correction, only the Q_e^2 plot is shown threefold. For sake of brevity, all other plots are based on sample ③ from 1999-2000, which contributes most to the total set. The plots which are not displayed here were also checked, and showed a similarly good description.

To reduce the contribution by fake electrons from hadrons of photoproduction events, a track reconstructed by the CJC and pointing to the electron cluster candidate is required. The track is then also used for the measurement of the electron angles θ_e and ϕ_e. Fig. 3.3 (left hand side) shows the distance of closest approach between the cluster center of gravity and the nearest vertex fitted track. A maximum distance of

- $\Delta_{\mathrm{clus,trk}} < 12\,\mathrm{cm}$

is allowed in order to fulfill the matching requirement. DJANGOH describes the region around the cut better than RAPGAP, which underestimates the data in the region of large $\Delta_{\mathrm{clus,trk}}$.

Fiducial cuts are placed on the position of the electron in the calorimeter, to exclude cracks in the LAr, where the energy measurement is poor:

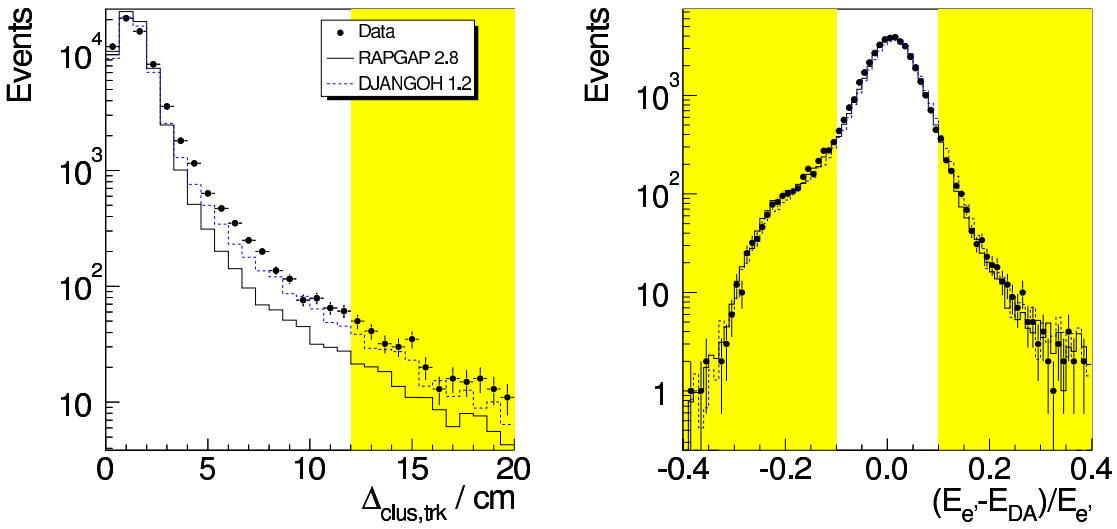

Figure 3.3: Distance of closest approach between the electron cluster and a corresponding track (left). Relative difference between a direct measurement of the electron energy and a cross check with the double angle method DA (right).

- $(\phi_e \mod 45°) \notin [-2°, 2°]$ and $z_e \notin [-70\,\text{cm}, -65\,\text{cm}]$, $z_e \notin [15\,\text{cm}, 20\,\text{cm}]$.

If a hard final state radiative photon is emitted and the corresponding energy deposit is not clustered to the electron, it will be assigned to the hadronic final state. In consequence both, the measurement of Q_e^2 as well as of the hadronic final state are spoiled. Such cases can be identified and cut if the direct electron energy measurement is checked with the double angle method. The latter reconstructs the electron energy with the help of the polar angles of the electron and the hadronic system, and is in first order independent of the absolute energy scale of the calorimeters:

$$E_e^{\text{DA}} = \frac{2E_0 \sin\gamma_h}{\sin\gamma_h + \sin\theta_e - \sin(\gamma_h + \theta_e)}. \tag{3.6}$$

Events where the deviation between both values is larger than 10% are cut:

- $(E_e - E_e^{\text{DA}})/E_e^{\text{DA}} < 10\%$.

Fig. 3.3 (right hand side) reveals that both Monte Carlos give a reasonable description of this relative difference.

Vertices from NC DIS events are to be found around the nominal interaction point according to a Gaussian distribution along the z axis (the width depending on the length of the colliding bunches), while the background from beam-gas and beam-wall collisions is almost flat or pronounced at massive structures, e.g. collimators. To reject those non-ep background events, the reconstruction of a primary vertex is required and a cut on the z-component of this vertex is applied

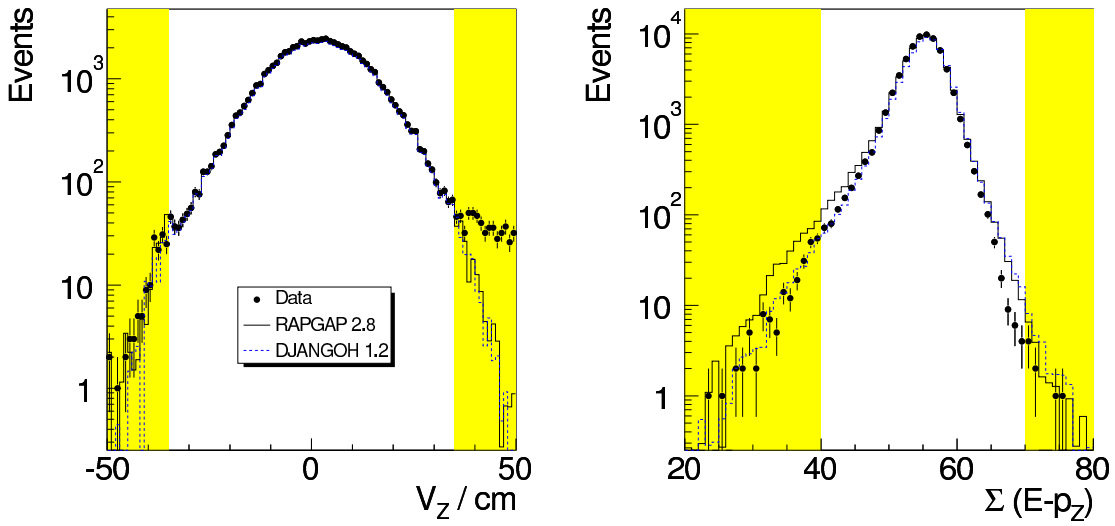

Figure 3.4: The z-component of a reconstructed primary vertex (left) and the $\sum(E-p_z)$ distribution (right).

- $-35\ \text{cm} < V_z < 35\ \text{cm}$.

Fig. 3.4 (left hand side) shows the distribution of V_z. Both Monte Carlos had to be reweighted in order to describe the V_z distribution within the accepted interval. This measure results in an improved description of the electron scattering angle θ_e and consequently also of Q^2.

Another useful variable to assure data quality is $\sum(E-p_z)$, which equals two times the electron beam energy for NC DIS events in a perfect detector ($\sum(E-p_z) = 2 \cdot 27.6\,\text{GeV}$). If particles are lost in the backward direction (e.g. the beam electron in case of photo production or an ISR photon), a too low value of $\sum(E-p_z)$ is reconstructed. In order to further reduce non-ep background, photoproduction and hard initial state radiation, the following cut is applied:

- $40\,\text{GeV} < \sum(E-p_z) < 70\,\text{GeV}$.

A slight difference between the Monte Carlos is visible at the lower tail of the $\sum(E-p_z)$ distribution in Fig. 3.4 (right hand side), whereby DJANGOH is more close to the data.

A pion within the hadronic final state of a charged current event may fake a scattered electron. To suppress such charged current events, the momentum balance in the transverse plane is utilised, whereby precisely measured neutral current reactions are characterised by

$$\not{p}_\perp \equiv \sqrt{\left(\sum p_x\right)^2 + \left(\sum p_y\right)^2} \approx 0\,\text{GeV}, \tag{3.7}$$

because the incoming beams have vanishing transverse momentum, which is conserved in the scattering. Charged current events feature apparently missing momentum, because of the undetected neutrino. Therefore a cut

- $\not{p}_\perp < 15\,\mathrm{GeV}$,

suppresses CC background. The $\not{p}_\perp$ distribution is resembled by both used Monte Carlos, presented in Fig. 3.5 (upper right).

Purely electro magnetic reactions like elastic QED-Compton or $\gamma\gamma$ events are characterised by small hadronic activity in the calorimeters and can therefore be suppressed by a cut on the hadronic fraction of the total measured energy,

- $E^{\mathrm{LAr}}_{\mathrm{hadronic}}/E^{\mathrm{LAr}}_{\mathrm{total}} < 10\%$,

shown in Fig. 3.5 (upper left). The mean hadronic fraction is to some extend overestimated by DJANGOH.

Diffractive events, where a colourless particle mediates the interaction, exhibit a rapidity gap between the proton direction and the remainder of the hadronic final state. This feature is not included in the analytical calculations of the QCD analysis to follow nor in the RAPGAP and DJANGOH Monte Carlo samples. In the phase space under investigation, no major contribution of rapidity gap events is expected, which is confirmed by Fig. 3.5 (lower plot). Here the rapidity of the most forward cluster with energy of more than 0.4 GeV is plotted. Rapidity gap events exhibit low values of η_{max}, however no excess is seen in the data. An additional cross check was performed with a RAPGAP event sample containing also rapidity gap events. No significant deviation in the event shape distributions was found.

To further reduce non-*ep* background events, a proper event timing with respect to the colliding beam bunches is required. The event timing is precisely measured by the central jet chambers CJC and has to match within 12 ns:

- $|t_0^{\mathrm{CJC}} - t_0^{\mathrm{nominal}}| < 12\,\mathrm{ns}$.

Finally, events originating from cosmic muons are identified by the QBGFMAR package [53] and removed.

Now that all cuts against background have been introduced, the Monte Carlo description of the kinematic variables on detector level is studied. Fig. 3.6 shows the Q^2_e distribution on a double logarithmic scale, all data sets are well described by the Monte Carlos.

Distributions of inelasticity y, reconstructed with the electron and the sigma method are pictured on Fig. 3.7. A logarithmic abscissa is chosen for y_Σ to focus on the low y_Σ region, where the corresponding cut is placed. The photoproduction background in the highest y_e bins is obvious in the data. DJANGOH undershoots the data somewhat, which is only visible on the linear ordinate of the y_Σ plot.

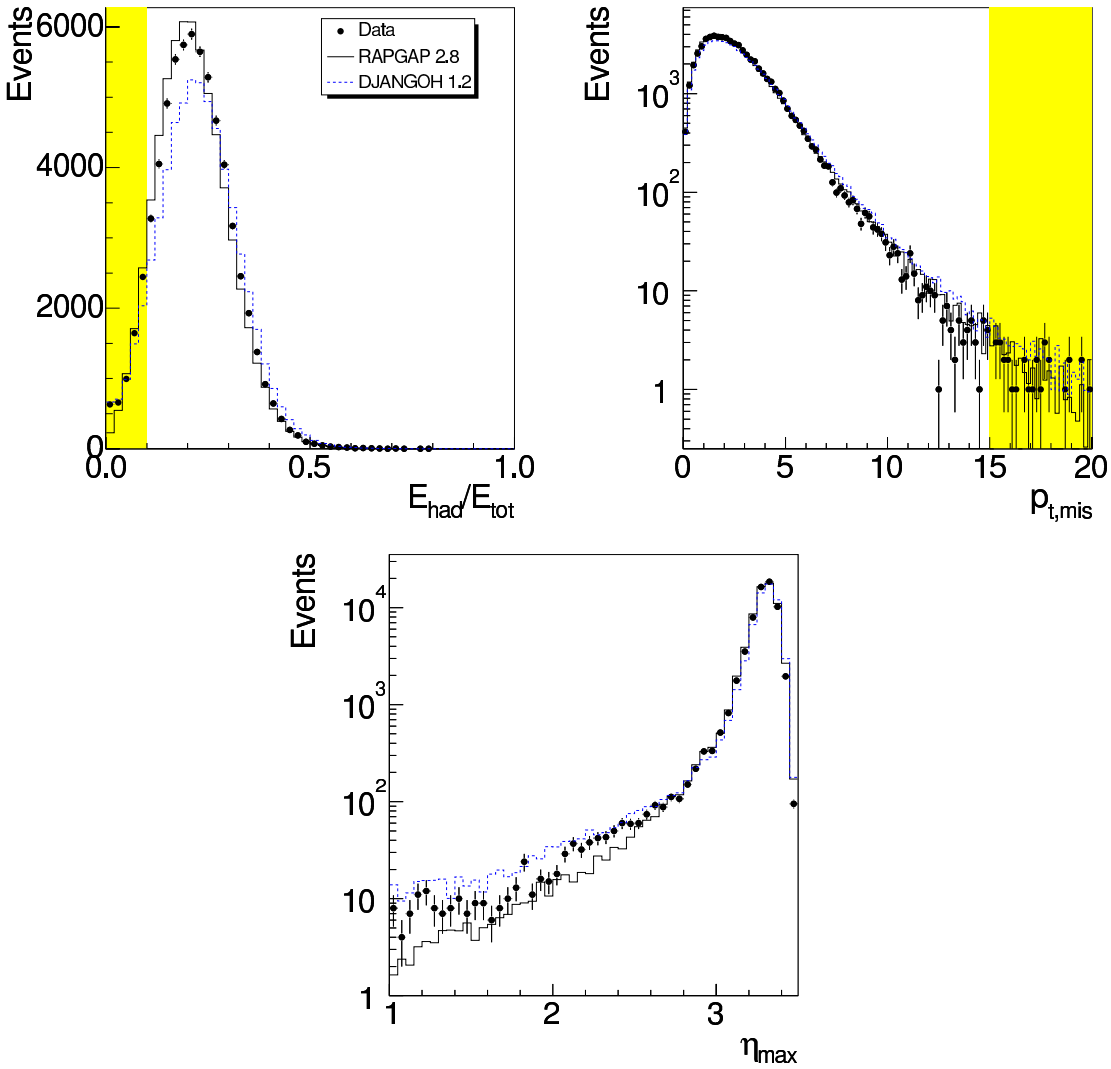

Figure 3.5: Hadronic fraction of the total measured energy (upper left), modulus of the transverse missing momentum vector (upper right) and the maximum rapidity of a cluster with energy greater than 0.4 GeV.

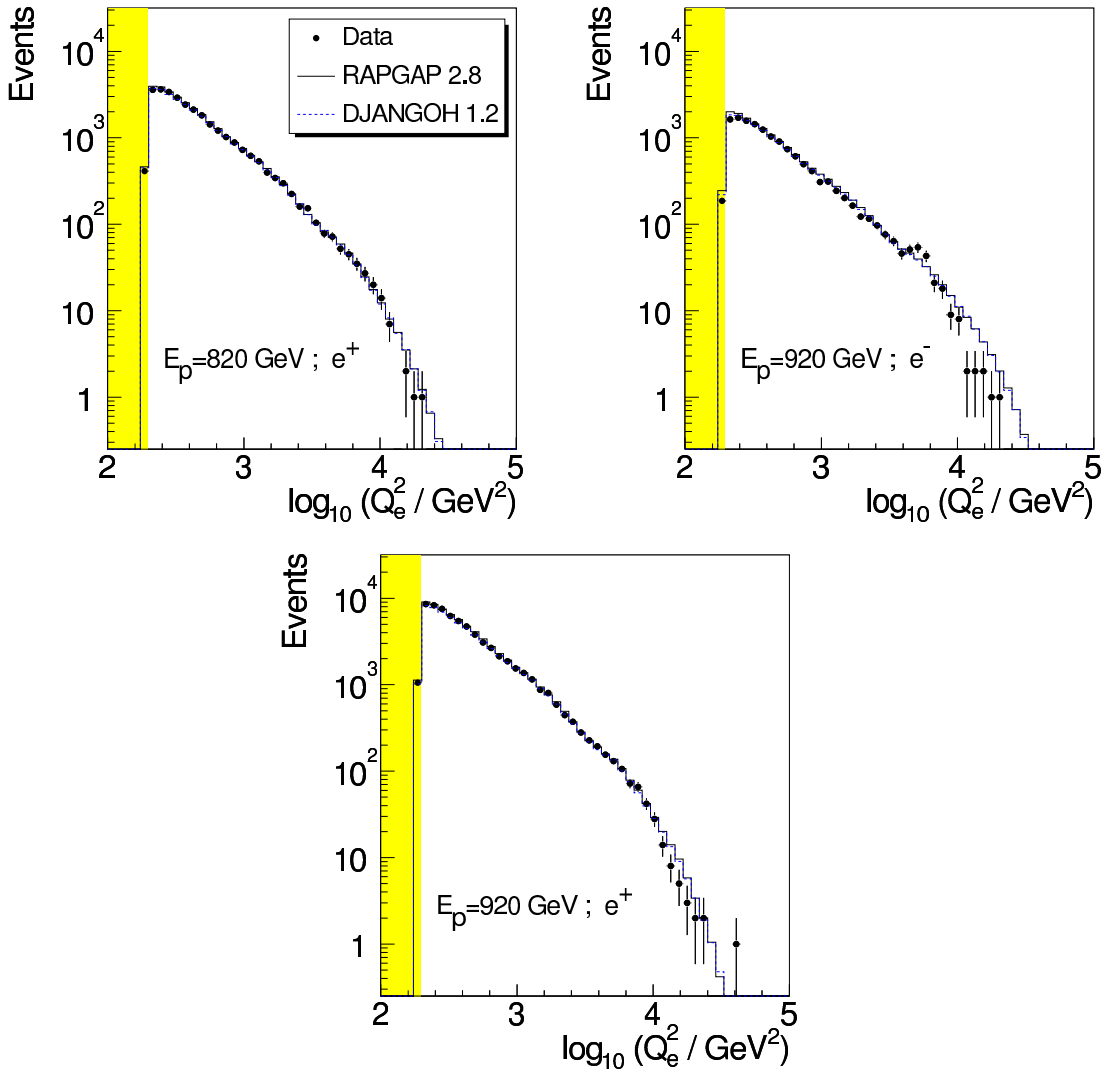

Figure 3.6: Distribution of the virtuality Q_e^2 for the three data sets. The selection requires $Q_e^2 > 196\,\mathrm{GeV}^2$.

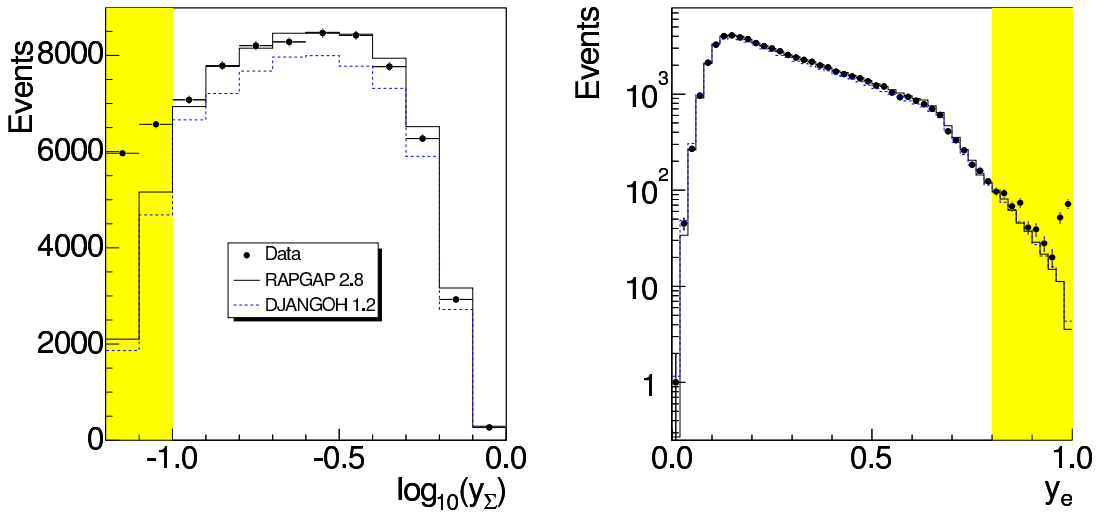

Figure 3.7: Distribution of the inelasticities y_Σ (left) and y_e (right). The selection requires $y_\Sigma > 0.1$ and $y_e < 0.8$.

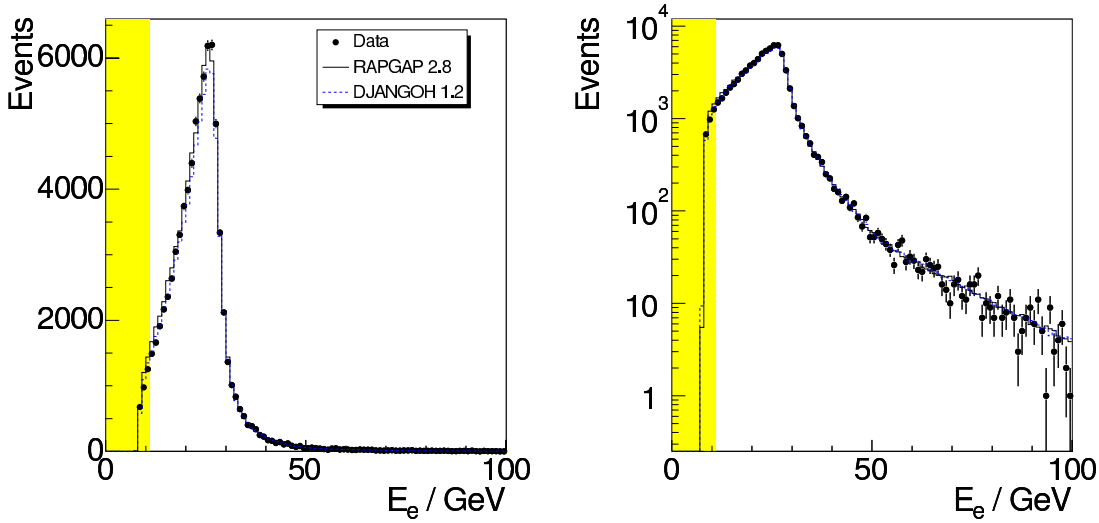

Figure 3.8: Distribution of the scattered electron energy E_e in linear and logarithmic scale. The selection requires $E_e > 11\,\text{GeV}$.

- $Q_e^2 > 196\,\mathrm{GeV}$
- $0.1 < y_\Sigma$
- $y_e < 0.8$
- $11\,\mathrm{GeV} < E_e$
- Trigger: ST67
- `QESCAT` electron with track/cluster link < 12 cm
- $-35\ \mathrm{cm} < V_z < 35\ \mathrm{cm}$
- $|p_T| < 15\,\mathrm{GeV}$
- $40\,\mathrm{GeV} < \sum(E - p_z) < 70\,\mathrm{GeV}$
- $(E_e^{\mathrm{QESCAT}} - E_e^{\mathrm{DA}})/E_e^{\mathrm{DA}} < 10\%$
- $E_{\mathrm{hadronic}}^{\mathrm{LAr}}/E_{\mathrm{total}}^{\mathrm{LAr}} < 10\%$
- $|t_0^{\mathrm{CJC}} - t_0^{\mathrm{nominal}}| < 12\,\mathrm{ns}$

Table 3.2: Overview of phase space and data quality cuts.

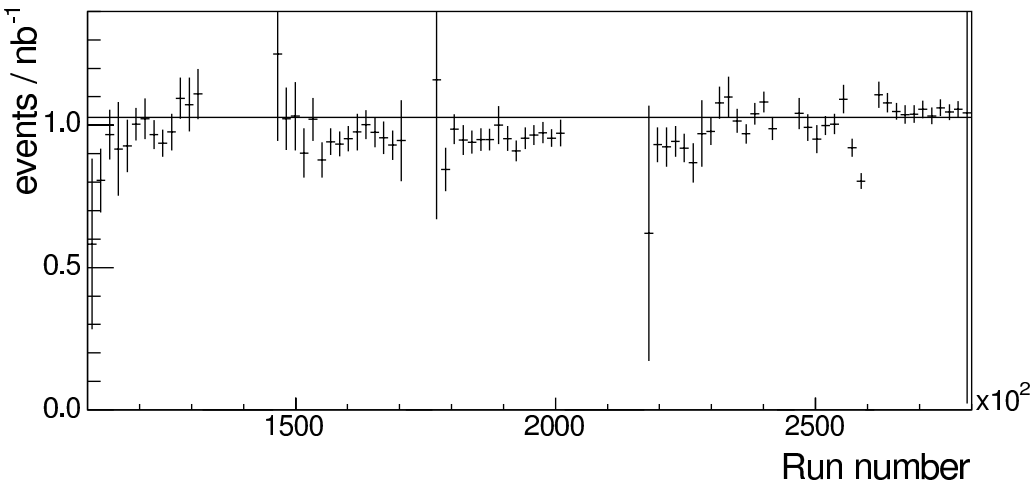

Figure 3.9: Event yield as a function of the data taking run number. The interval on the abscissa corresponds to the years 1995-2000.

Fig. 3.8 shows the reconstructed energy of the scattered electron, which is well described by both Monte Carlos over the whole range. A summary of all cuts is given in Tab. 3.2.

Fig. 3.9 shows the event yield, i.e. the number of selected events per integrated luminosity, against the consecutive number of data taking runs. It depends on the trigger performance and detector acceptance, which may vary with time. The gaps are caused by special data takings periods as well as by periods without beams, where run numbers were consumed for cosmic muon data taking. The event yield appears quite stable for the whole used data set. If inefficient regions within the central tracker had been excluded, the stability could be further improved. Anyway, a precise absolute cross section determination is not the aim of the presented analysis, which deals with **normalised** differential cross sections.

To summarise, the Monte Carlos RAPGAP and DJANGOH describe all control distributions well, but not always to the same level of precision. In consequence it is concluded that the selected data consist of clean neutral current DIS events. The total selected event sample amounts to 107693 events for an integrated luminosity of $106\,\mathrm{pb}^{-1}$.

The data is further divided into bins of Q, given in Tab. 3.3, to study the scale dependence of the event shape variables.

3.1.3 Background Estimate

The total contribution of background processes to the event sample is small. It may however be that the few remaining background events accumulate in only few

# of Q bin	1	2	3	4	5	6	7
Interval/ GeV	[14,16[	[16,20[	[20,30[	[30,50[	[50,70[	[70,100[	[100,200[
Events N	26614	35324	30536	12015	2102	867	235

Table 3.3: Definitions of bins in the momentum transfer Q.

Process	γp	CC	el. QED Compton	$\gamma\gamma$	$W^{\pm}$ production
Monte Carlo	PYTHIA	DJANGOH	WABGEN	GRAPE	EPVEC
total relative contribution	10^{-3}	10^{-7}	10^{-5}	10^{-3}	10^{-7}
typical bin significance	< 0.2	0.0	< 0.02	< 0.2	0.0
highest bin significance observed	0.7	0.006	0.08	0.3	0.001

Table 3.4: Contribution of background processes to the selected data set, estimated with simulated Monte Carlo samples.

bins of the event shape distributions and this way compromise the measurement. To quantify this, a measure of significance is introduced. The significance of a background process in a single bin is defined as

$$\frac{B}{\sqrt{T}}, \tag{3.8}$$

with B the number of background events and T the total number of events in the bin. Tab. 3.4 summarises the expected remaining background in the selected data set, estimated with Monte Carlo simulations. The biggest contribution stems from photoproduction. However, within the 679 investigated result bins, the highest observed significance is well below unity. It can hence be noted that the background is sufficiently suppressed.

3.2 Reconstruction of the Hadronic Final State

Any measurement of event shape variables relies on a precise measurement of the hadronic final state, which is (in neutral current deep inelastic scattering) defined as everything measured in the detector save the scattered electron. The following describes how this is performed in the work at hand.

The present analysis enhances former investigations of event shapes at H1 [8, 14] twofold:

- Instead of calibrated calorimeter clusters alone, combined objects of clusters and tracks make up the hadronic objects. This approach leads to a better reconstruction of less energetic hadronic particles.

- A new energy weighting scheme for the LAr calorimeter was chosen (based on studies described in [54]), which is known to exhibit significant improvements in the response and linearity, the energy resolution and the signal shape compared to the standard (`H1REC`) energy weighting scheme.

The basic way to measure energetic hadrons is to use both the electromagnetic and hadronic sections of the LAr and SPACAL calorimeters. However, particles originating from the event vertex have to cross dead material in front of the calorimeter. At low particle energies, energy loss in the dead material can be problematic, all the more because a noise suppression algorithm has to remove isolated clusters of very low energy. The central tracking chambers CJC have a good momentum resolution for low energy particles, therefore it may appear obvious to combine signals from both devices, as long as no double counting of energy occurs.

H1 combined objects are constructed by the `FSCOMB` [55] algorithm, the built entities are called **HFS objects**. The algorithm works as follows:

1. Clusters already assigned to the scattered electron are removed.
2. The noise suppression removes isolated low energy deposits.
3. Primary vertex fitted tracks are selected, with $p_T \leq 2\,\mathrm{GeV}$ and a minimum angle to the electron of 1° in θ and 5° in ϕ. An energy is assigned to the tracks under the assumption of a pion mass hypothesis.
4. For each track the following procedure is performed:
   - The track is extrapolated into the calorimeter, where successively clusters are removed, beginning with smallest distance of closest approach to the track, until the removed energy equals the track energy within one standard deviation of the energy resolution or all clusters within a cylinder of radius 25 cm (electromagnetic part) or 50 cm (hadronic part) around the track have been removed.
   - If the total removed energy is larger than that of the track, the last cluster is kept and rescaled to match the track energy instead.
5. Finally, all remaining clusters and tracks form the HFS objects.

Event shapes are by their definition sensitive to low momentum particles, thus it can be expected that the inclusion of low momentum tracks in HFS combined objects leads to an improved measurement. In an ideal detector a measured quantity would be the same on detector as well as on hadron level. Due to the limited resolution of a real world detector, the reconstructed value will always deviate to a greater or lesser extent. However, if the observable is binned, it is only of interest if an event

is assigned to the right bin or not. This is the reason why bin sizes should match roughly the resolution of the observable.

To quantify the performance of the reconstruction, it is common practice to study the bin purities and stabilities of the final distributions with the help of Monte Carlo event samples. Purity P_i and stability S_i of bin i are defined as follows:

$$P_i = \frac{N_i^{\text{det}\cap\text{had}}}{N_i^{\text{det}}}, \qquad S_i = \frac{N_i^{\text{det}\cap\text{had}}}{N_i^{\text{had}}} \tag{3.9}$$

with

N_i^{det} : number of events assigned to bin i on detector level,
N_i^{had} : number of events assigned to bin i on hadron level,
$N_i^{\text{det}\cap\text{had}}$: number of events assigned to bin i on both, detector and hadron level.

Only events passing cuts on detector level are considered, therefore the detector acceptance is separated from purity and stability. High purities and stabilities indicate a reliable reconstruction.

Fig. 3.10 shows exemplarily for two event shape distributions purities and stabilities for calibrated clusters and combined objects. It is obvious that in every bin the combined objects give better results of up to $\simeq 5\%$, which can be explained by the fact that the combined objects on detector level approximate the hadron level better than cluster do, thus bin migrations are lessened. This conclusion holds also for the other investigated event shape variables and over the whole studied Q range.

The hadronic calibration of the non-compensating LAr calorimeter relies on an energy weighting technique, which equalises the electromagnetic and hadronic components of a shower by software. The different response of the calorimeter to single electromagnetic and hadronic particles can be expressed in the e/π ratio, which is known from test beam measurements. Being always greater than unity, this ratio is a function of the particles energy, giving rise to a non linear response for energy deposited by hadrons.

The energy weighting procedure is performed as follows:

1. Initially the electromagnetic calibration is applied to all clusters.

2. A shower shape analysis identifies the hadronic clusters, the fine granularity of the LAr calorimeter is essential in this step.

3. The hadronic clusters are reweighted, weighting factors depend on the location of the cluster, its energy density and on the energy in the neighborhood of the cluster.

Within the framework of other H1 analyses, e.g. of inclusive cross sections [51] and of dijet cross sections in photoproduction [56], it could be demonstrated that

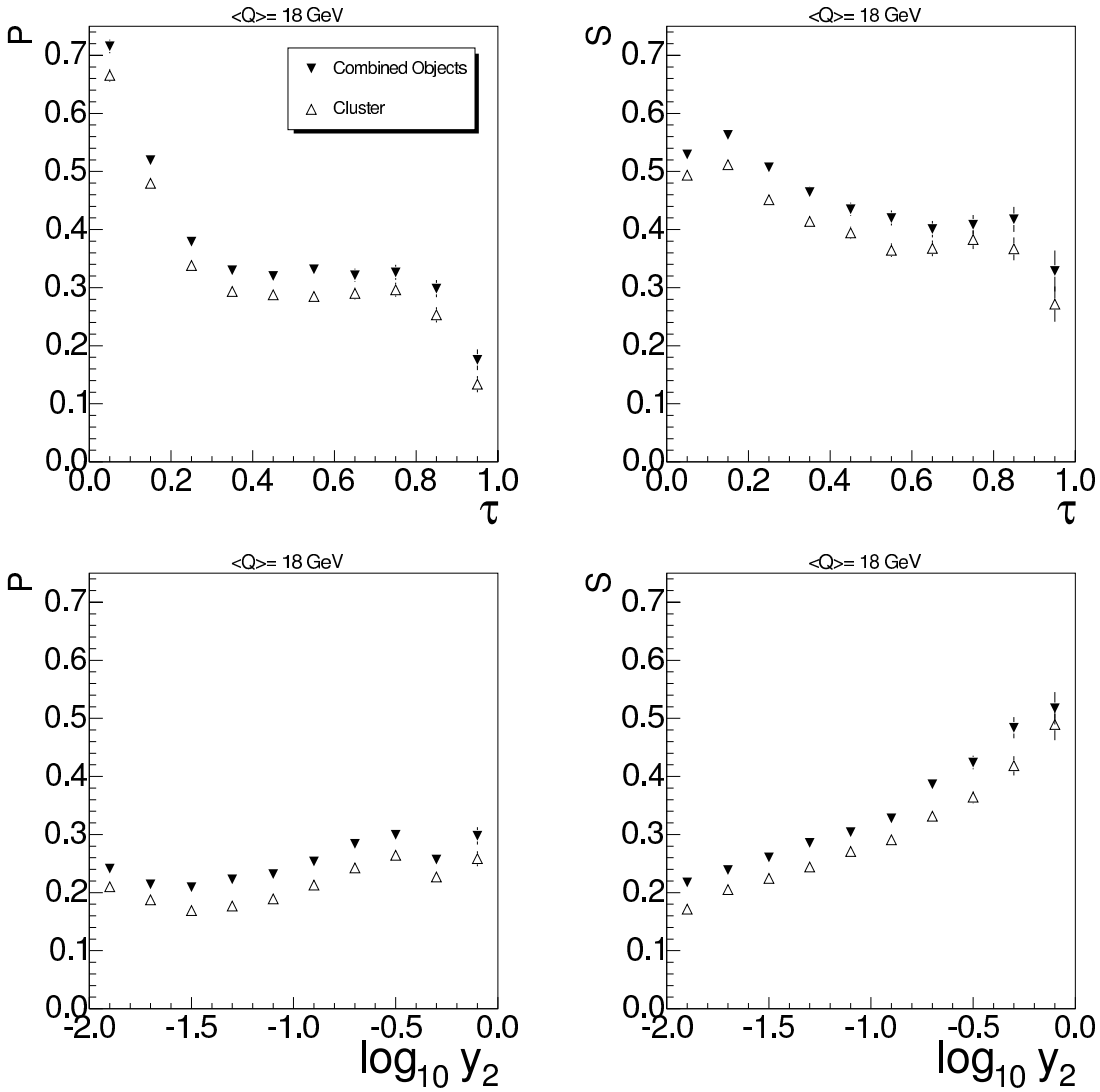

Figure 3.10: Comparison of calibrated clusters and combined objects, determined with the RAPGAP Monte Carlo event sample. Purity (left) and stability (right), exemplarily shown for thrust τ (upper) and jet rate y_2 (lower).

the final calibration is described by the Monte Carlo simulation to a precision of better than 2%. This residual difference is taken as the systematic error for the absolute hadronic energy scale.

To evaluate the calibration for the present work, the transverse momentum balance p_{Te}/p_{Th} of neutral current events is investigated. If the hadronic final state is properly calibrated, it will balance the transverse momentum of the electron, resulting in a transverse momentum balance of one. A comparison of p_{Te}/p_{Th} between data and Monte Carlo is pictured in Fig. 3.11, as a function of the inclusive hadronic angle γ_h, to study the homogeneity throughout the calorimeter. The upper plot proves that the momenta are well balanced, though small deviations can be seen. The lower plots depict the double ratio of the transverse momentum balance, i.e. the data distribution divided by the Monte Carlo distribution. It is documented that the Monte Carlo models the data to an accuracy of 2% for the new energy weighting, where for the old scheme only 4% accuracy can be quoted. The usage of combined objects or calibrated cluster is not pivotal when working with the new weighting.

The bottom line is, that by using the new weighting scheme in this work, the hadronic energy scale uncertainty can be reduced from the original 4% to 2%. The restricted knowledge of the absolute hadronic energy scale proved to be the largest contribution to the experimental systematic error for jet rates in former analyses.

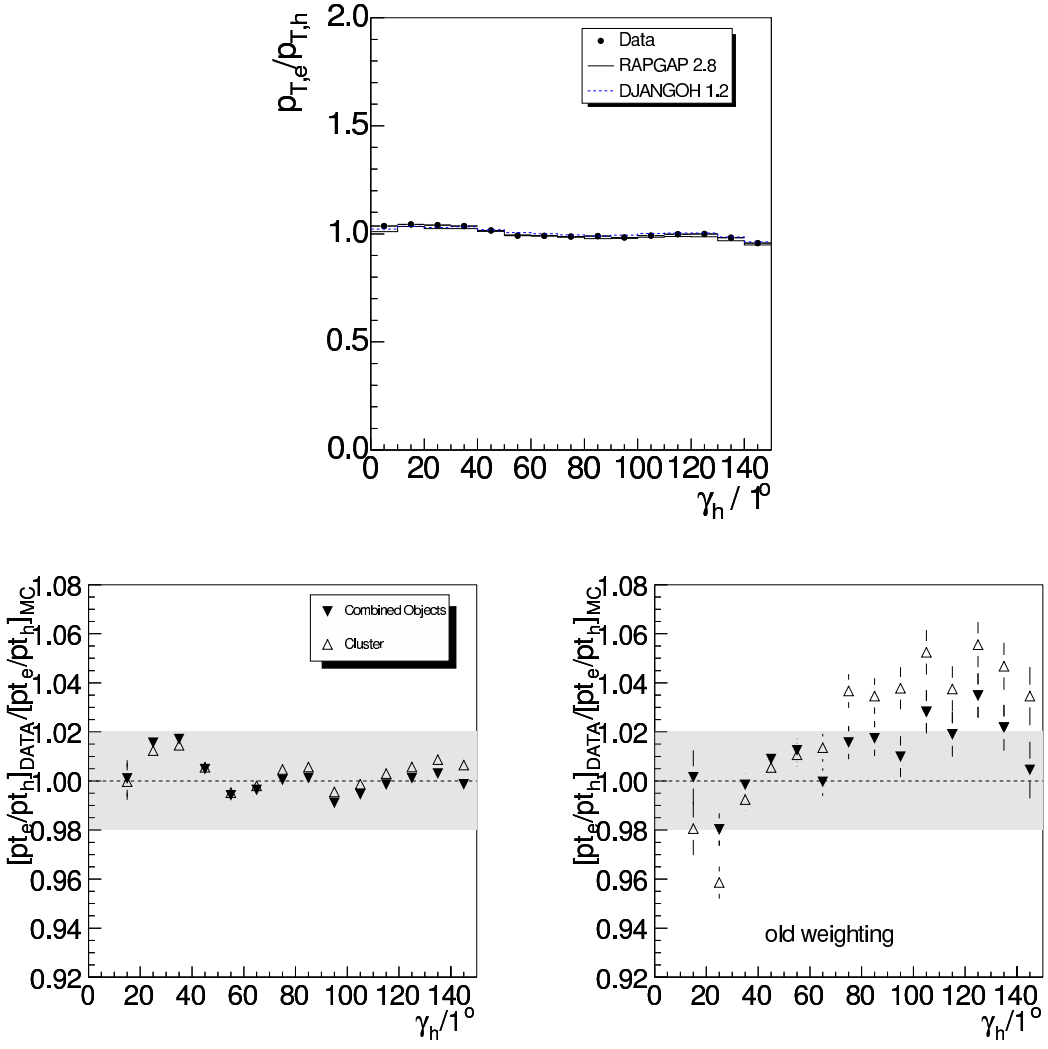

Figure 3.11: p_T balance as a function of the inclusive hadronic angle (upper plot). The double ratio data/Monte Carlo, for the new weighting, which is used in this work (lower left), and the old weighting (lower right).

Chapter 4

Detector Correction Procedure

The measured data are degraded by detector effects, i.e. the specific parameters of the H1 apparatus influence the distributions. To make the results comparable to other data, e.g. from the ZEUS collaboration, detector effects have to be compensated by a correction procedure, i.e. results are given on hadron level.

The comparison with theory calculations could in principle be done on detector level, if the calculated events were fed into a detector simulation. However, this is not possible with the NLO calculations used in this work, because events corresponding to real and virtual corrections of a parton configuration need to enter the same result bin, in order to partly cancel each other and yield the correct cross section (see also section 1.2.2). If one would apply the detector simulation on the NLO events, this could not be guaranteed, because the limited detector resolution leads to bin migrations. Therefore the data are corrected to the hadron level.

The correction is done with a Bayesian unfolding method, which is especially suitable if bin migrations are relatively high. Moreover, this method is not so dependent on the exact description by the Monte Carlo used for unfolding.

QED radiative effects depend on detector resolution and acceptance, and are so far not included in the theory calculations. Hence these are also corrected for in the data, which are then given on the "non-radiative hadron level".

4.1 Unfolding of Detector Effects

The influence of the detector properties on the reconstructed distributions can be infered from the detector simulation, in order to correct for resolution effects, acceptance gaps and possible biases. A prerequisite for this are Monte Carlo event samples of the physical process under study: neutral current DIS in the present analysis.

The Monte Carlo generators used for the detector correction are RAPGAP 2.8 and DJANGOH 1.2, both are expected to give a fair estimate of the event shape distributions. This will be investigated in the next subsection. Thereafter, the

actual unfolding method is presented, yielding data distributions on hadron level, which are the basis for the fit in chapter 5.

In principle one could also perform the correction to the level of hard partons in the Monte Carlo, thus the correction would also include the hadronisation. This is not done in this work, because of the ambiguities mentioned in section 1.2.4, instead power corrections are applied on the theory calculations. Moreover, by not unfolding to parton level, the dependence on the specific hadronisation model is considerably reduced.

4.1.1 Monte Carlo Samples

The high statistics Monte Carlo event sets, as described in section 2.3, are compared to data on detector level. Again, for the sake of brevity, only plots for data set ③ (see also section 3.1), are shown. Fig. 4.1-4.2 picture the spectra with statistical errors of all ten event shape variables, which are studied in this work. Out of all seven Q bins, three are shown: for the lower, middle and high Q region. The description is in general good. At low Q, both Monte Carlos are close to each other and to the data, only for the multi jet rates y_3 and y_4 discrepancies are visible.

At high Q, the description of RAPGAP is similarly good, whereas DJANGOH is a bit more off. The latter predicts for some observables (all but the jet rates and K_{out}) distributions, which are too high at the QPM limit $F = 0$ and consequently too low at higher values. This feature of DJANGOH (used together with the CDM hadronisation model as implemented in ARIADNE) was also found in a previous analysis of 2-jet event shapes [57].

For high Q and at high values of the shape variable τ, B and ρ_0, there are some data bins which seem to lie above a (imaginary) smooth distribution. The reason for this is not clear. However, as will be shown in section 4.2, these regions are strongly affected by QED radiation effects (but not for τ_c and C-parameter), in such a manner that the bin contents are increased by radiation. It could be, that in rare cases high energetic clusters from FSR photons contaminate the reconstructed hadronic final state. Particles in the vicinity of the scattered electron correspond to objects on the edge between the Breit frame hemispheres, far away from the current jet, and may hence give rise to high values of a 2-jet event shape (compare section 1.2.2). On the other hand, both Monte Carlos include QED radiation and should therefore describe such effects.

While not precise for all bins, the Monte Carlo description is sufficient for unfolding. To take into account the discrepancies observed, both Monte Carlos are used for the detector correction. The result obtained with RAPGAP is taken as the central value, half the difference to the result from DJANGOH is taken as the systematical error for the model dependence.

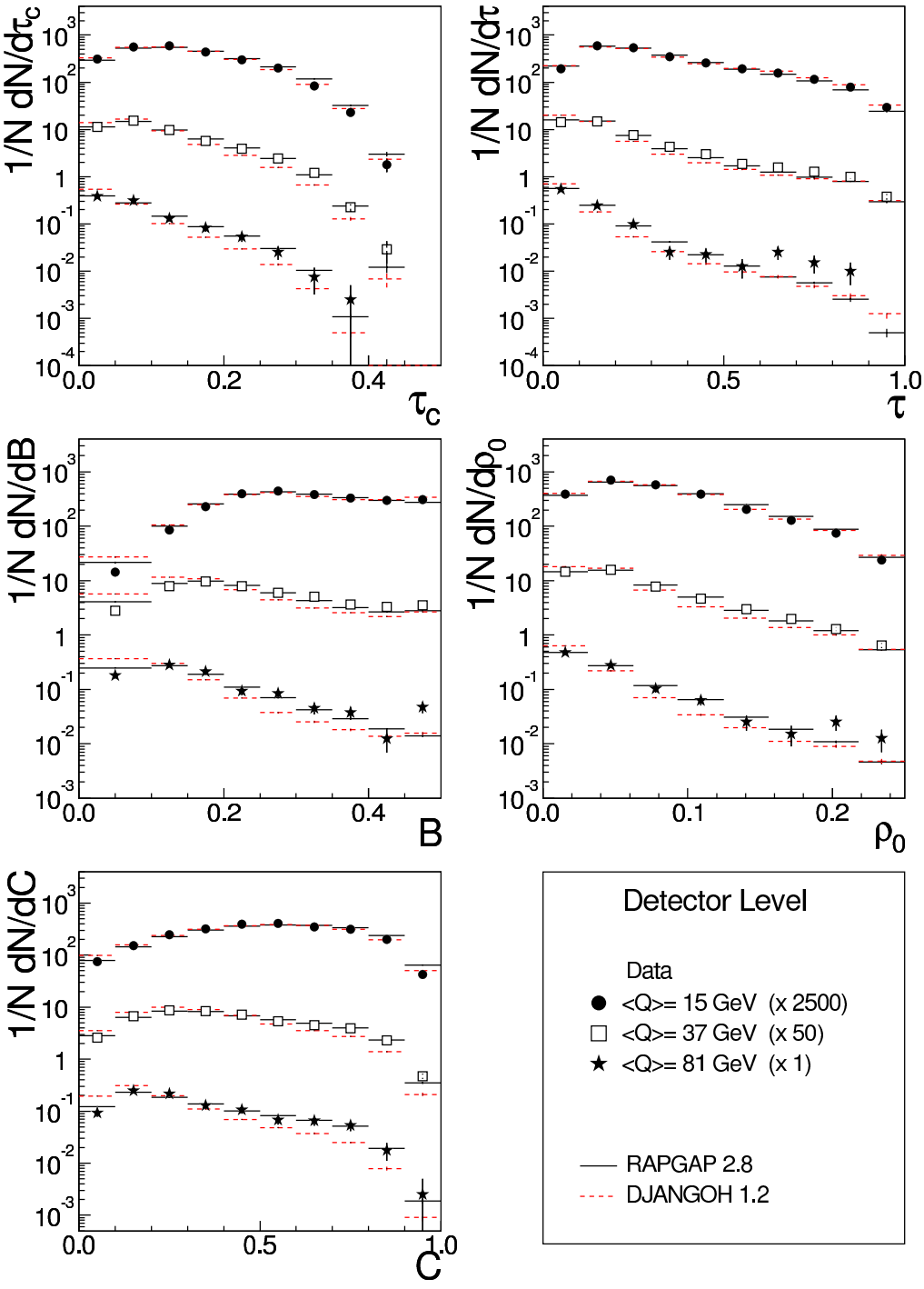

Figure 4.1: Event shapes on detector level for three out of the seven Q bins. The error bars represent the statistical uncertainty.

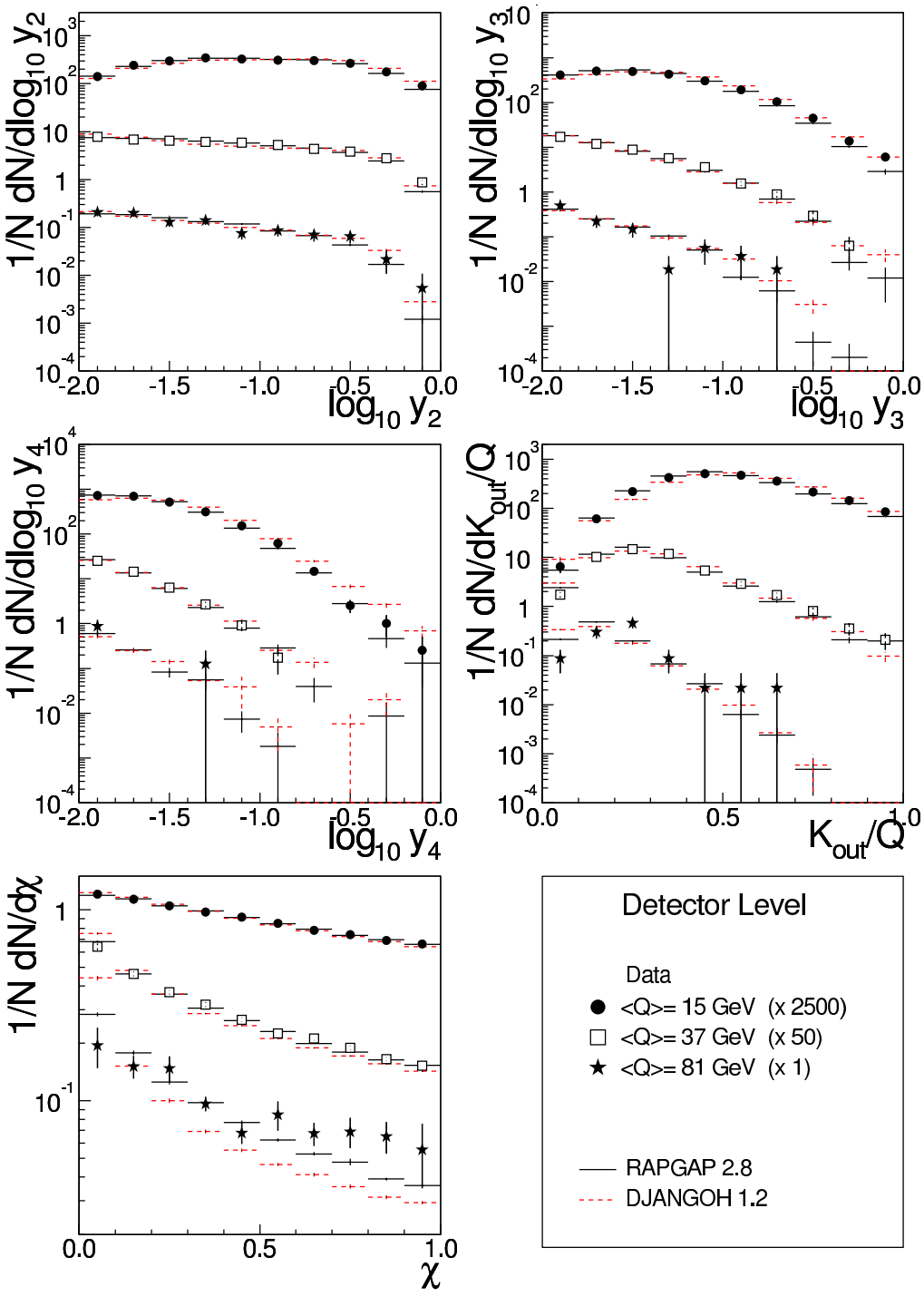

Figure 4.2: Event shapes on detector level for three out of the seven Q bins. The error bars represent the statistical uncertainty.

4.1.2 Unfolding Procedure

Most straightforward and often used is the so called bin-by-bin correction

$$h^i_{\text{data}} = \frac{h^i_{\text{MC}}}{d^i_{\text{MC}}} d^i_{\text{data}}, \tag{4.1}$$

where h^i and d^i denote the content of bin i on hadron and detector level, respectively. The corrected result in a bin depends only on data of the same bin on detector level, thus bin migrations are completely neglected. When this method is applied, it is usually demanded that the migrations, evaluated by bin purities, are not too high. E.g., in a recent analysis by the H1 collaboration of inclusive cross sections, a bin purity greater than 0.3 is required [51].

Bin purities for the event shape distributions of the present work are studied in the following. The azimuthal correlation χ is an exception in that sense, that for this observable the concept of bin migrations is not applicable. For this observable any event fills n^2 bins of the distribution, where n is the number of hadrons (on hadron level) or of HFS objects (on detector level). Because the number of hadrons and HFS objects will in general be different, no unique assignment of bin entries is possible, and therefore the bin purity is not well defined.

Fig. 4.3 shows the purities for all bins of the present analysis in an overview. To guide the eye, the region of purity less than 30% is marked by a shaded area. Although bin migrations have been lessened by choosing combined objects, the bin purities are still in general rather low, especially for the jet rates and parts of the K_{out} distribution. It is obvious that the 4-jet rate y_4 is already at the limit of resolution of the H1 detector: to measure even higher jet rates is not reasonable.

While the full range of definition is always shown in Fig. 4.3, only part of the bins will later be used for the QCD fit. No explicit cut on a minimum bin purity is applied for bins used for fitting.

Low bin purities could lead to problems, if a fit of the unfolded data treats the bins as uncorrelated. To account for the correlations, the full covariance matrix is needed, however the bin-by-bin correction does not provide such a matrix. Therefore only for χ the bin-by-bin correction is used, whereas for all other observables a method which takes the migrations into account is needed.

The response of the detector can be expressed by the **smearing matrix** C^{ij}, which is defined via the equation

$$d^i = C^{ij} h^j. \tag{4.2}$$

The smearing matrix contains the complete information of bin-to-bin migrations. It is reasonable to add an extra bin to the distribution, which holds events which did not pass requirements in the event shape definition[1]. This way migrations in and out of the interval of definition are accounted for.

[1] Examples for such requirements are the y_2 cut in the definition of K_{out} and χ, or the minimum current hemisphere energy requirement for the 2-jet event shapes, compare section 1.3.

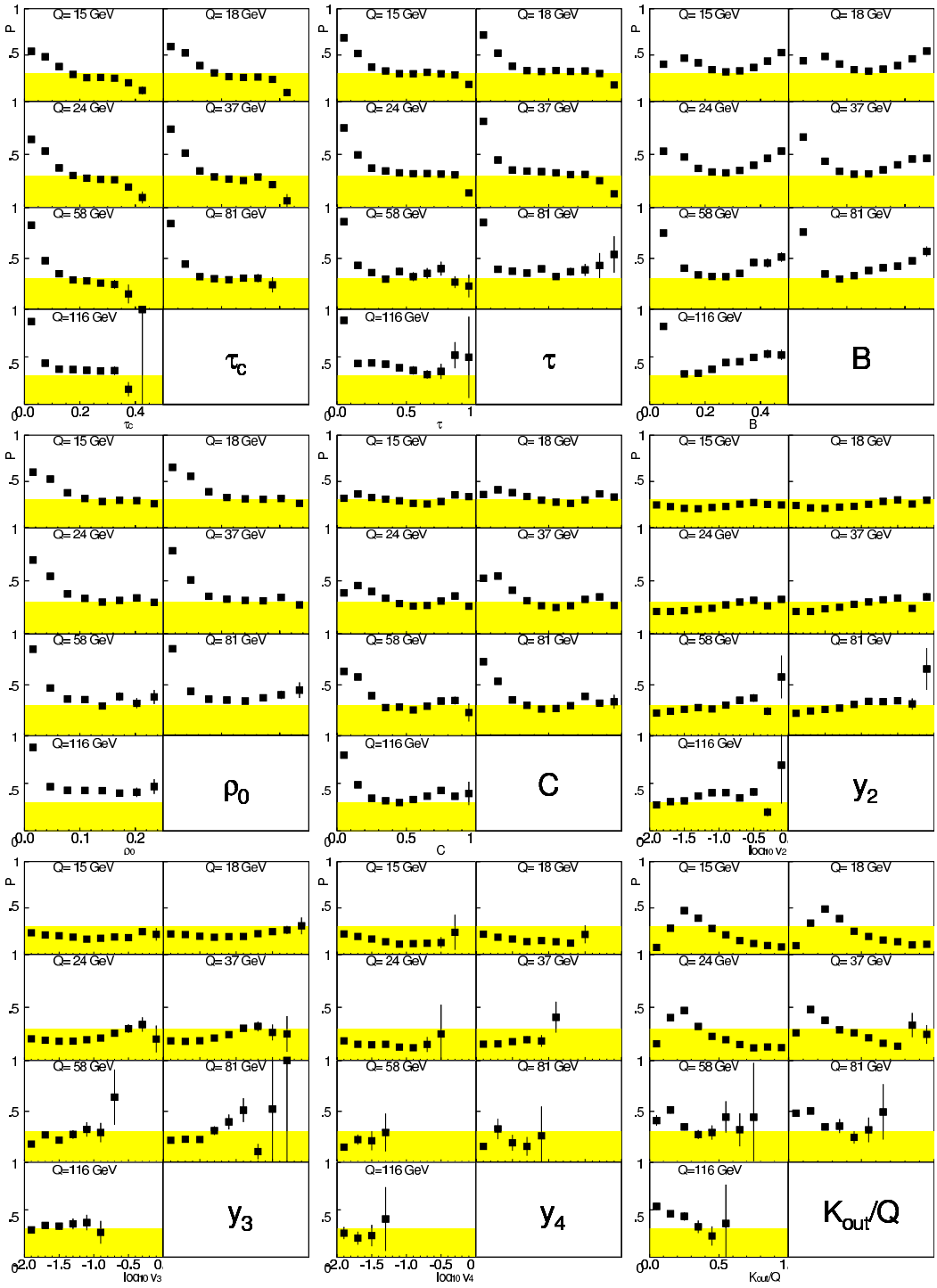

Figure 4.3: Bin purities, determined with RAPGAP. To guide the eye, the shaded area marks the region below 0.3. For the definition of purity see Section 3.2.

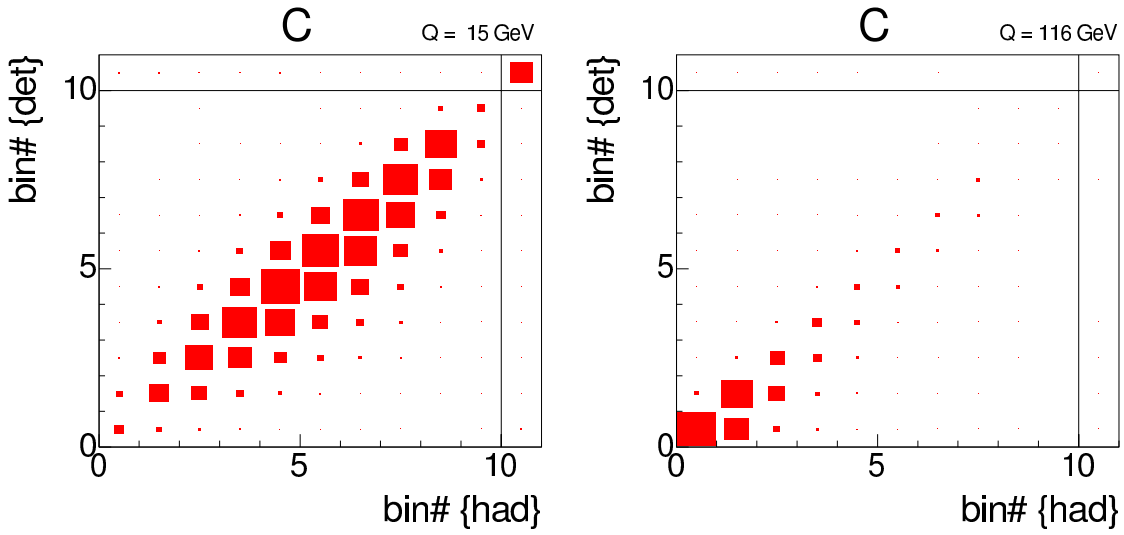

Figure 4.4: Smearing matrices for the C-parameter event shape for the lowest (left) and the highest Q bin (right). Bin 11 contains events which are not accepted by the current hemisphere energy requirement.

The smearing matrix for Monte Carlo events C^{ij}_{MC} can easily be calculated, because d^i_{MC} as well as h^i_{MC} are known. Fig. 4.4 shows the smearing matrix for the C-parameter in two Q bins.

It may appear obvious to simply invert the smearing matrix

$$U^{ij}_{\mathrm{MC}} \equiv (C^{ij}_{\mathrm{MC}})^{-1}, \tag{4.3}$$

where U^{ij}_{MC} is labeled the unfolding matrix, and apply it on the detector level distribution,

$$h^i_{\mathrm{data}} = U^{ij}_{\mathrm{MC}} d^i_{\mathrm{data}}. \tag{4.4}$$

As a matter of fact, this procedure yields a bias free estimate of h^i_{data} [58]. However, it is well known that this matrix inversion method leads to instabilities, because small statistical fluctuations in the measurement can produce large effects on the result. To overcome this issue, various regularisation methods exist.

The present work adopts an iterative algorithm exploiting the Bayes theorem for the determination of the unfolding matrix, which was introduced in [59]. This method was also used in a previous event shape analysis by the H1 collaboration [14, 57], as well as in a recent dijet analysis [60].

The Bayes theorem connects the conditional probability $P(C_i|E_j)$, that an effect E_j is due to a cause C_i, with the inverse conditional probability $P(E_j|C_k)$ and the

initial probability $P_0(C_i)$ of the cause:

$$P(C_i|E_j) = \frac{P(E_j|C_i)P_0(C_i)}{\sum_k P(E_j|C_k)P_0(C_k)}. \tag{4.5}$$

Applied to the problem of unfolding, the causes can be identified with the hadron level and the effects with the detector level. Consequently, the smearing matrix corresponds to $P(E_j|C_i)$. The algorithm proposed in [59] yields the following prescription for the unfolding matrix:

$$U^{ij}_{\mathrm{MC}} = \frac{C^{ij}_{\mathrm{MC}} h^i_0}{\sum_k C^{kj}_{\mathrm{MC}} \left(\sum_k C^{ik}_{\mathrm{MC}} h^k_0\right)}. \tag{4.6}$$

If the smearing matrix is known from Monte Carlo simulation, the measurement d^i alone is not sufficient to draw a conclusion for the hadron level: in addition a "prior" h^i_0 has to be given.

The method of the iterative algorithm is, to take a rough estimate as the prior to determine the hadron level with the help of equations 4.4 and 4.6, and then use this intermediate result as prior h^i_0 for the next iteration. With every iteration the so far unfolded result is fed as the prior distribution in the unfolding formula. The solution is expected to approach a good estimate in just few iterations. The result is relatively independent to the hadron level distribution of the Monte Carlo which is used to determine the smearing matrix, i.e. the model dependence of the detector correction is reduced compared to the bin-by-bin correction [57].

What should be used as the prior in the first iteration? In case of complete ignorance about the form of h^i, even a flat distribution may be suitable. However, event shape distributions are very different from flat distributions, compare Fig. 4.1-4.2, so in this work the hadron level from the unfolding Monte Carlo is used as the prior, to speed up convergence.

Naïvely one could argue that in the limit of infinite iterations, the result converges to the optimal result. That is in general not the case, as G.D'Agostini points out in [61]: "...in practice this technique [the iterative procedure] is just a 'trick' to give to the experimental data a weight (an importance) larger than that of the priors.". It may happen, that after some iterations fluctuations build up, a problem also well known for the matrix-inversion method. So it is rather that the Bayes solution converges to the solution which would be obtained with matrix inversion. A possible modification to damp fluctuations was proposed in [61]: smooth the distributions between two iterations with the help of a low order polynomial. This has also been tested for the present analysis, but was found to be not helpful, possibly because the distributions to unfold are rather steep.

In consequence, one needs to find a number of iterations when to stop, which will be studied in the following. Fig. 4.5 shows the unfolded data distribution of thrust in Q bin no. 4, after 1-10 iterations. While the bins in the center of the distribution

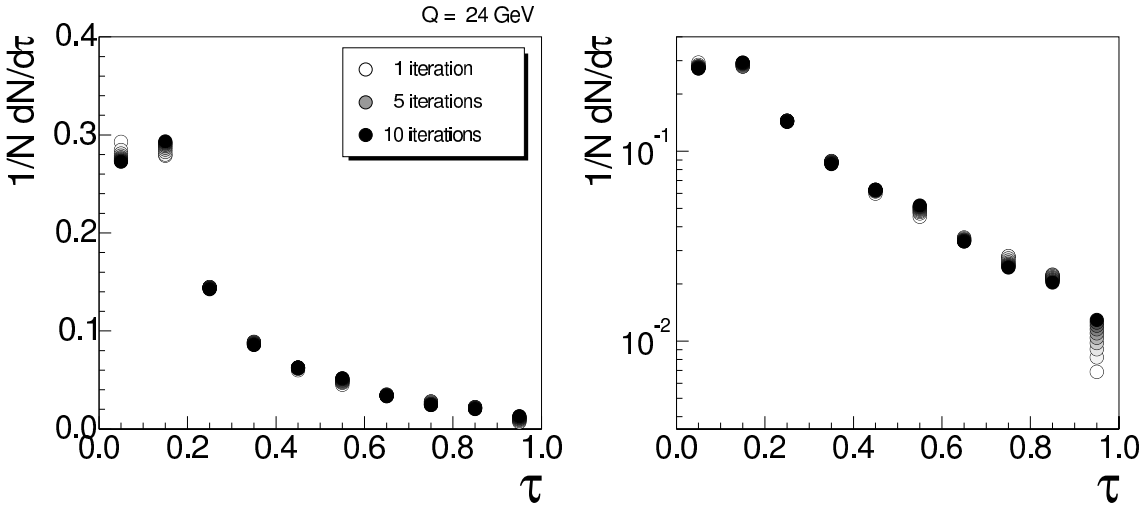

Figure 4.5: Data unfolded with the Bayesian method, in linear (left) and logarithmic (right) scale. RAPGAP is used as unfolding Monte Carlo.

remain stable, the bins at the edges experience some dependence on the number of iterations. To study the unfolding procedure in more detail, simulated DJANGOH events are treated like real data and unfolded with the help of the RAPGAP event set. This way, one can compare the unfolded result to the "true" values, see Fig. 4.6 where the histogram marks the optimal solution. In the leftmost bin the solution converges to the right result, whereby in the rightmost bin the solution drifts away.

Fig. 4.7 shows the relative difference between the unfolded result and the true distribution, over 10 and over 100 iterations. The solution appears stable, with the exception of the two rightmost bins. The dependence from the number of iterations varies by observable and Q bin: compare Fig. 4.8, showing the 2-jet rate over 10 iterations. Again, few bins at the tail of the distribution drift away.

On the right hand side of Fig. 4.8, the absolute value of the relative deviations of all observables within the intervals used for the QCD fit are summed for all Q bins, and plotted against the number of iterations. For comparison, the corresponding value for the bin-by-bin unfolding is given as a line. The unfolded result resembles the correct hadron level best after three iterations, then it starts to drift away again. So the recommendation of three iterations given in [61] can be confirmed by this study. Moreover, in case of this Monte Carlo scenario, the bin-by-bin correction performs less well, as long as the number of iterations for the Bayesian unfolding is chosen between 2 and 20.

To give an idea of the size of the corrections, Fig. 4.9 shows the correction factors that are obtained by the bin-by-bin method. Mostly, the corrections are less

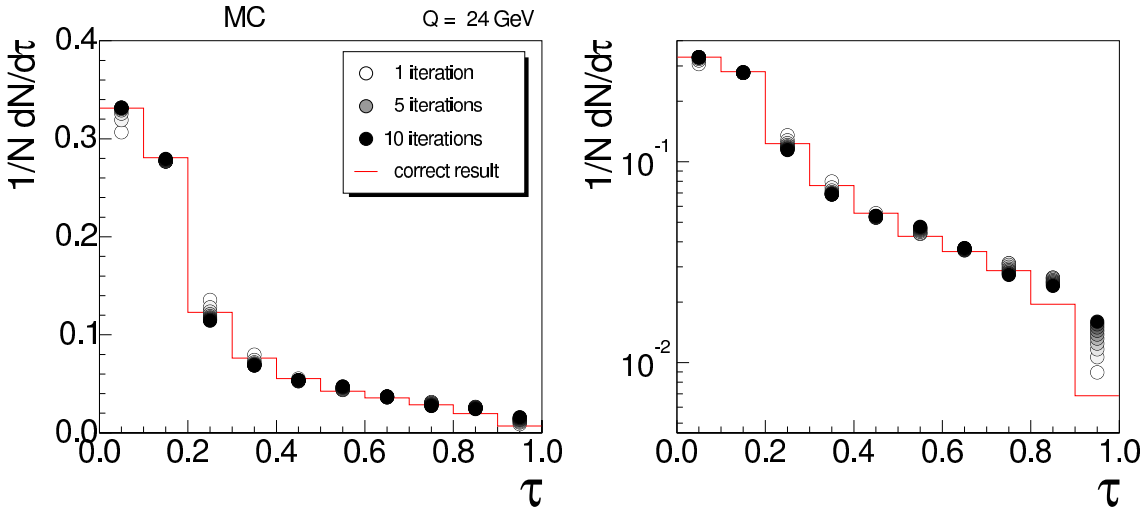

Figure 4.6: DJANGOH events used as fake data and unfolded with the Bayesian method, in linear (left) and logarithmic (right) scale. RAPGAP is used as unfolding Monte Carlo. The histogram denotes the "true" hadron level of DJANGOH.

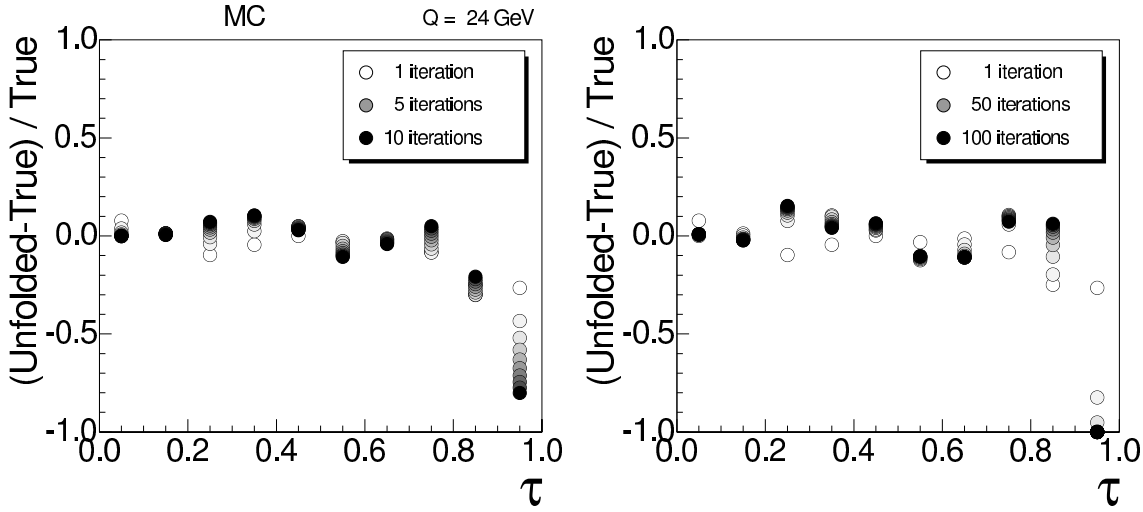

Figure 4.7: DJANGOH events used as fake data and unfolded with the Bayesian method, for 10 iterations (left) and 100 iterations (right). RAPGAP is used as unfolding Monte Carlo.

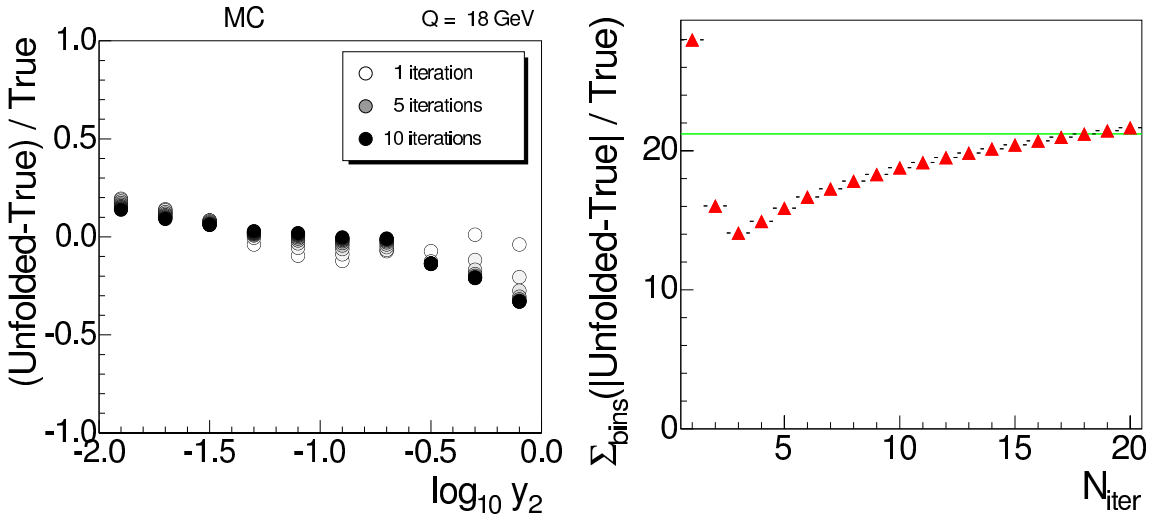

Figure 4.8: DJANGOH events used as fake data and unfolded with the Bayesian method, for 10 iterations (left). RAPGAP is used as unfolding Monte Carlo. Deviations between the unfolded result and the true solution (right), summed over all bins used for fitting against the number of unfolding iterations. The optimum in this Monte Carlo study being three iterations.

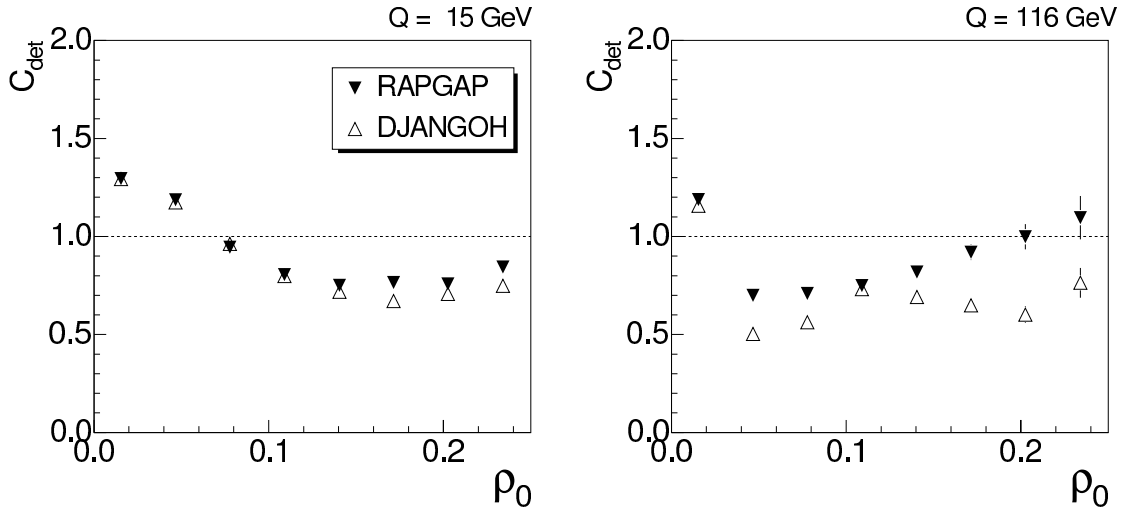

Figure 4.9: Correction factors determined by the bin-by-bin method, for the jet mass for the lowest (left) and the highest Q bin (right).

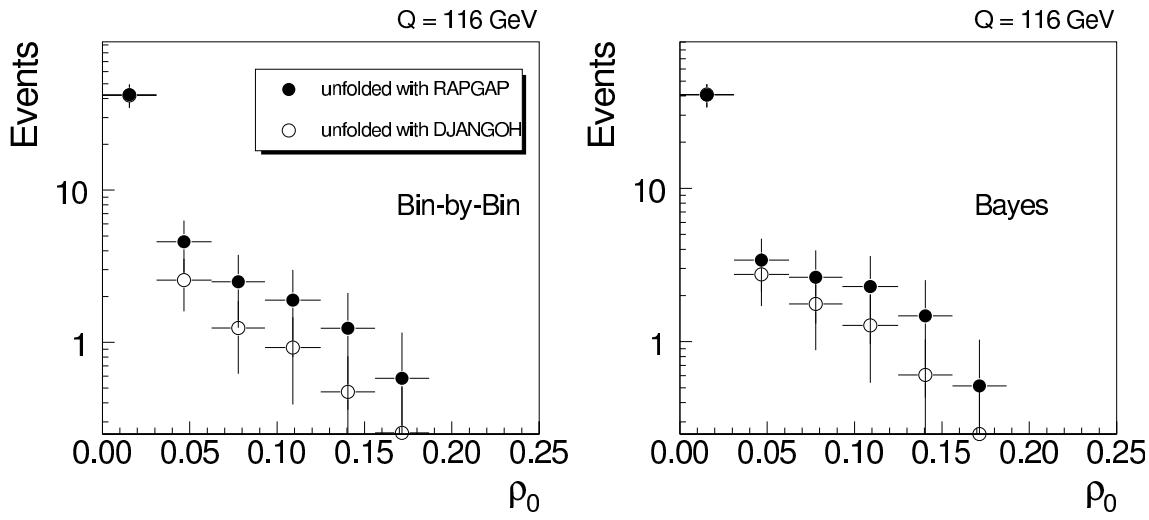

Figure 4.10: Corrected data distributions for the jet mass obtained by the bin-by-bin method(left) and the Bayesian unfolding (right).

than 30%, however discrepancies are observed at high Q. This is expected, because DJANGOH and RAPGAP disagree at high Q (see Fig. 4.1). The consequences for the unfolded results are visualised on Fig. 4.10, where it can be seen that the model dependence on the Monte Carlo model is smaller for the Bayesian unfolding, as it is expected. However, at high Q the statistics of the data are limited, anyway.

To illustrate the effect of the detector resolution, Fig. 4.11 displays the correlation matrix as determined by the Bayesian unfolding, where non diagonal elements are due to bin migrations. Bin correlations are smaller at high Q, corresponding to a better detector resolution at higher energies.

Conclusion:

- The Bayesian unfolding is used in this work, because it incorporates bin migrations and provides a covariance matrix.
- A test, namely unfolding one Monte Carlo with another, revealed that for the bins used in the QCD fit, the Bayesian method yields more precise results than the bin-by-bin method.
- The best overall solution is reached after three iterations.

The bias which is introduced by the unfolding is estimated via unfolding the Monte Carlo with itself, and is included in the systematical error.

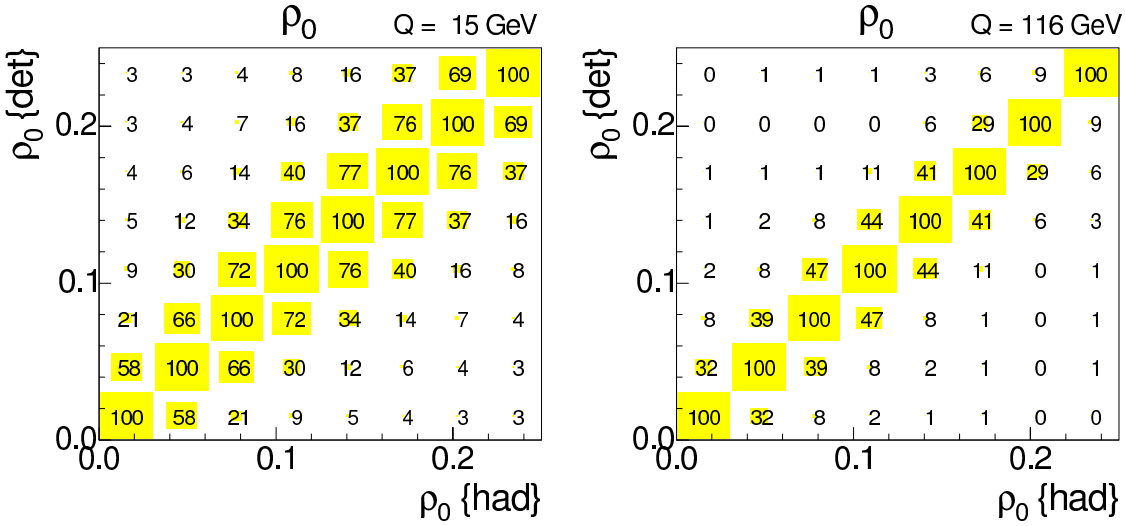

Figure 4.11: Correlation matrices for the jet mass for the lowest (left) and the highest Q bin (right). The numbers denote the correlation in per cent.

4.2 QED Radiative Corrections

Currently available NLO calculations do not account for QED radiation, therefore the unfolded data is corrected for this radiative effects in a second step. This is done by applying bin-by-bin correction factors. It is not possible to build a smearing matrix in this case, because an event with an additional radiative photon will in general lie in a different Q bin than its counterpart on Born level.

In order to determine the correction factors, two additional sets of event samples from RAPGAP 2.8 and DJANGOH 1.2 are used. They are generated with exactly the same settings as the central set, except that the QED radiation in the HERACLES submodule was turned off. Correction factors are then derived from bin divisions of both samples on hadron level. Only phase space cuts were applied on the non radiative hadron level, therefore also the detector acceptance is corrected for.

Fig. 4.12-4.13 display the correction factors to be applied to the data. Depending on the observable, the corrections get quite high with increasing Q. The factors are consistent with previous findings [57].

Thrust τ and jet broadening B feature large sensitivity to QED radiation already at low scales. A possible explanation of this could be that both event shape variables make explicit use of the virtual boson axis in their definition. Radiative photons alter the virtual boson axis because of momentum conservation. The other 2-jet event shapes (τ_c, ρ_0 and C-parameter) do not use the virtual boson axis explicitly: e.g. the thrust axis used in the definition of τ_c can follow rotations of the current

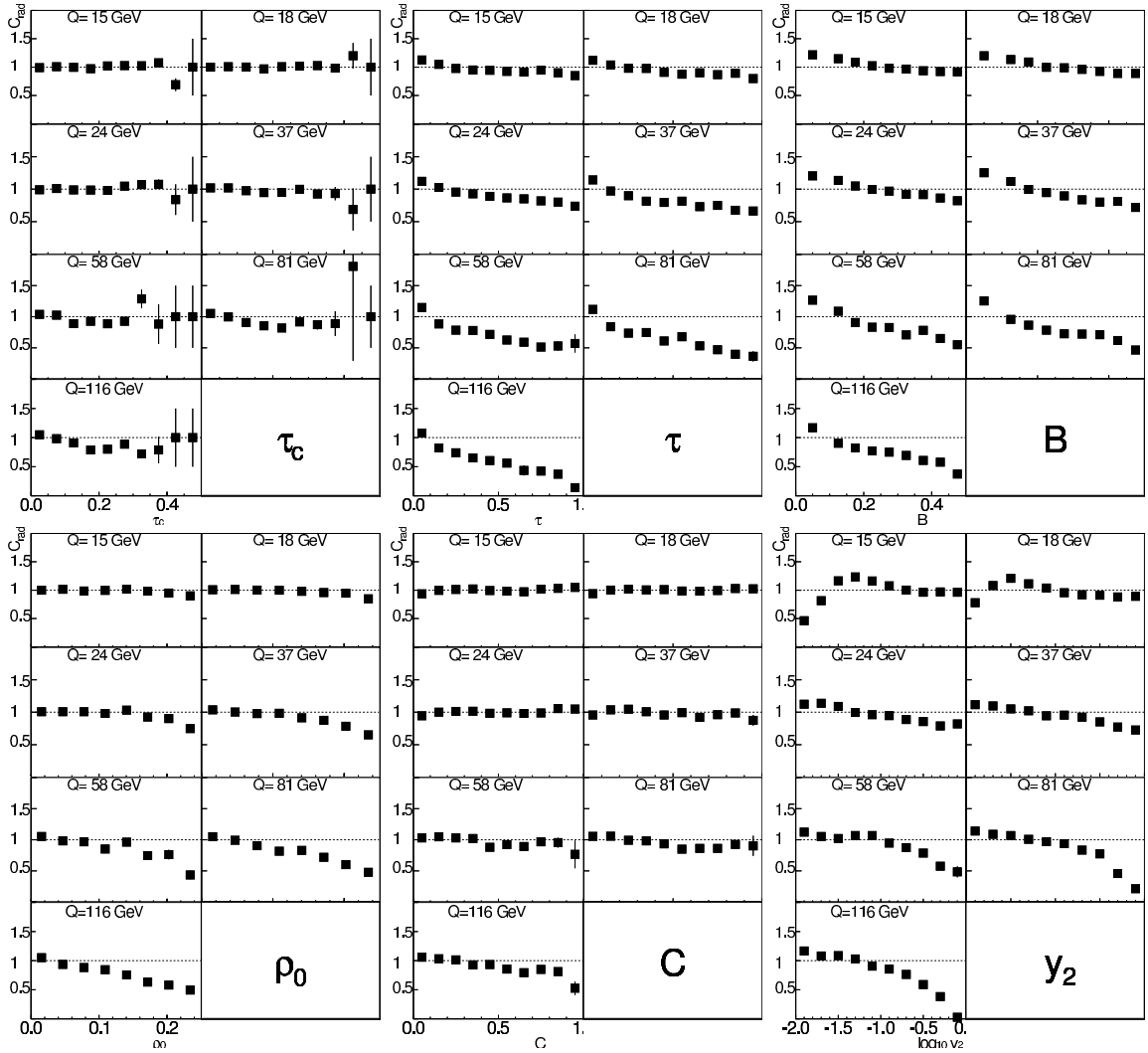

Figure 4.12: Correction factors for the event shape distributions, including QED radiation and detector acceptance, determined with RAPGAP/HERACLES.

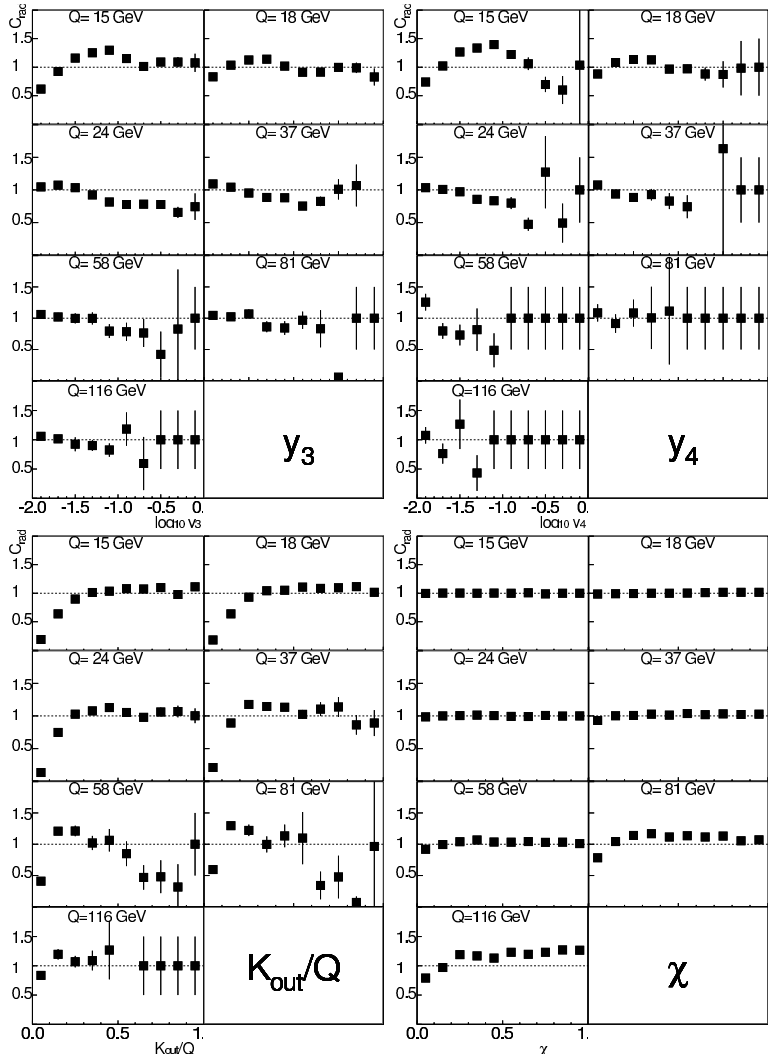

Figure 4.13: Correction factors for the event shape distributions, including QED radiation and detector acceptance, determined with RAPGAP/HERACLES.

hemisphere, which is fixed to the virtual boson axis.

Since jet rates are defined on particles of both, the current and the remnant hemisphere in the Breit frame of reference, the acceptance corrections are in general larger than for the 2-jet event shapes. This property is visible for the region of low y_2 and low Q.

The azimuthal correlation χ appears to be nearly insensitive to QED radiation. Apparently the definition relying on azimuthal differences $\Delta\phi$ lets radiative effects mainly cancel.

4.3 Experimental Systematic Uncertainties

The reconstruction and detector correction procedure aims to the best central value of the observables, but uncertainties remain, e.g. on the absolute value of the energy scales and on the Monte Carlo model used for unfolding. To get an estimate for the systematic errors of the results, several parameters are varied, to an extent corresponding to what is assumed to be one standard deviation. The analysis is then individually repeated for every variation, whereby the change in the result bins marks the systematic error.

Systematic errors can be determined from data as well as from Monte Carlo event samples. It has been checked that the results obtained from both are compatible at low and moderate Q; the actual systematic error determination was then performed based on the RAPGAP Monte Carlo sample, in order to profit from the very good statistics at high Q, where the data is subject to statistical fluctuations.

Most systematic error estimates, which are briefly discussed in the following, are standard for H1 analyses (see e.g. [62]), only the hadronic energy scale needs special treatment for event shape variables.

The kinematics and therefore the boost to the Breit frame of reference depends on the reconstructed electron, thus the electromagnetic energy scale is varied by its uncertainty of $\pm(1\% - 3\%)$, depending on the z position of the electron cluster. In addition polar and azimuthal angles of the electron are changed by $\pm 3\,\mathrm{mrad}$ each.

Clusters from the SPACAL calorimeter contribute only to a lesser extent to the hadronic final state. The variation of the hadronic energy scale of this calorimeter by $\pm 7\%$ showed negligible impact, and is hence not included. Likewise, a shift of the track momentum for combined objects by $\pm 3\%$ was checked, but not included in the final systematic error.

For hadrons, a LAr calorimeter energy scale uncertainty of 2% is quoted (compare section 3.2), consequently this value is used for the jet rates, the out-of-event plane momentum K_{out} and the azimuthal correlation χ. In case of the other event shape variables, any hadronic energy scale variation cancels by definition. Though, it appears too optimistic to assume an error free measurement with the LAr, thus another variation is used for these variables, which is described in the following.

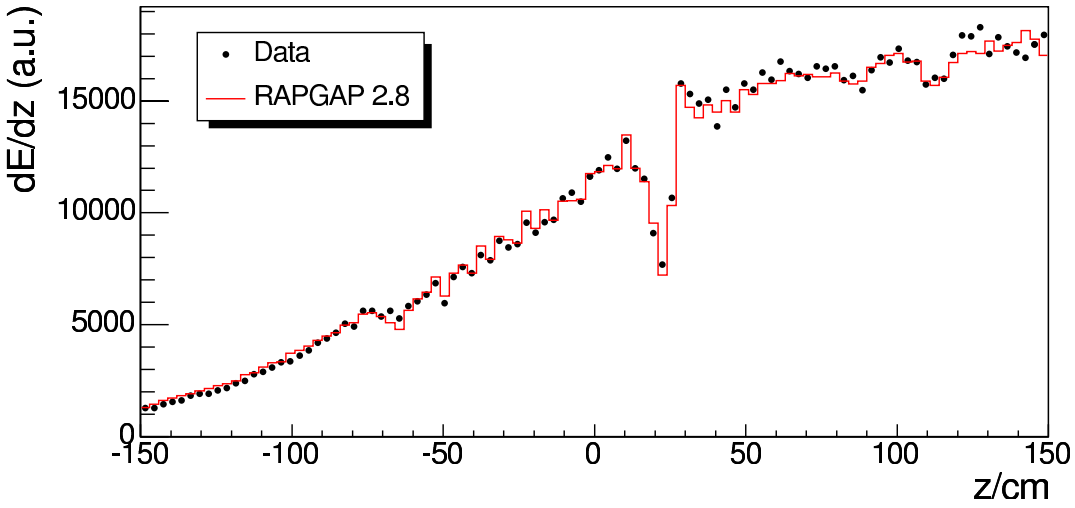

Figure 4.14: Differential energy flow as a function of the z position within the detector.

Event shapes are sensitive to the intercalibration of the calorimeters, i.e. to the relative calibration between parts of the detector. Inhomogeneities are in general included in the detector simulation, and are this way corrected for in the unfolding step. As a suitable quantity to check how well the description of the Monte Carlo actually is, the differential energy flow is used. This variable denotes the mean total hadronic energy, measured at some position within the H1 detector.

Fig. 4.14 shows the differential energy flow on detector level, as a function of the z position at the inner calorimeter surface. Several structures are visible in the distribution, which stem from regions of dead material within the LAr. Especially the z crack at $+20\,\mathrm{cm}$ (compare section 3.1.2) results in a prominent gap. This energy flow distribution is well described by RAPGAP/H1SIM.

Fig. 4.15 displays the relative difference between tha data and RAPGAP in two dimensional spherical coordinates. The root mean square of the deviations amounts to 8.6%, but one has to take into account that the statistics of the data is limited, hence part of the observed deviations are statistical fluctuations. However, regions of correlated shifts are visible, e.g. corresponding to the upper right (data lower than RAPGAP) and lower middle (data higher than RAPGAP) in the plot.

Now the assumption is made, that this deviations are a rough estimate of the uncertainty on intercalibration. In a systematic study, the calibration of the hadronic final state objects is modified by a factor taken from the bin contents of Fig. 4.15, according to the polar angle θ and azimuth ϕ of the object,

$$E_{\mathrm{varied}} = E_{\mathrm{calibrated}} \left(1 \pm \frac{\Delta E^{\mathrm{data}} - \Delta E^{\mathrm{MC}}}{\Delta E^{\mathrm{MC}}} \right) \qquad \Delta E(\theta, \phi) \equiv \int_{\mathrm{bin}} \frac{\mathrm{d}E}{\mathrm{d}\theta \mathrm{d}\phi}. \tag{4.7}$$

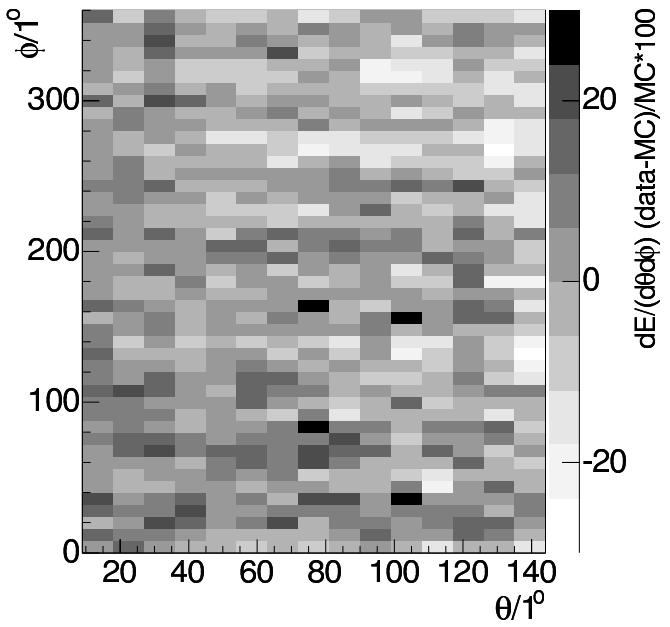

Figure 4.15: Double differential energy flow as a function of the position within the detector. Shown is the relative difference between data and RAPGAP in per cent.

The resulting change in the results is considered as the systematic hadronic energy uncertainty for τ_c, τ, B, ρ_0 and the C-parameter. Since in the measured spectra a large number of events contribute, which are evenly distributed in ϕ, the effect on the results is small (compared to e.g. the electromagnetic energy scale uncertainty).

All systematic variations which have been considered are summarised in Tab. 4.1.

The uncertainties due to the energy scales and electron angle measurements give rise to correlations between the bins of the unfolded event shape distributions, hence a covariance matrix is build for these systematic errors. This is done in two steps: Firstly an intermediate covariance matrix V' is prepared [63]

$$V'_{ij} = 1/2 \sum_{\epsilon \in +,-} \delta_i^\epsilon \delta_j^\epsilon, \tag{4.8}$$

where i and j are bin indices and ϵ denotes the variation of the scale (up/down). The deviation with respect to the central scale in bin i is denoted by δ_i^ϵ. Obviously this estimate of the covariance matrix is not exactly precise, because only two samples (on top of the central scenario) enter the calculation. In a second step the errors are symmetrised:

$$\bar{\delta}_i = \max_{\epsilon \in +,-} (|\delta_i^\epsilon|) \tag{4.9}$$

1. Variation of the electromagnetic energy scale of the QESCAT electron finder by $\pm(1\% - 3\%)$.
2. Variation of the polar and azimuthal angles of the electron by ± 3 mrad each.
3. Variation of the hadronic energy scale of the LAr calorimeter by $\pm 2\%$ (for y_2, y_3, y_4, K_{out} and χ).
   Variation of the intercalibration of the hadronic energy, with root mean square of $\simeq 8\%$ (for τ_c, τ, B, ρ_0 and C-parameter).
4. Usage of RAPGAP with parton showers and DJANGOH with the color dipole model for unfolding, half of the difference is taken as error.
5. An estimate of the bias from the unfolding procedure was determined by unfolding MC samples with themselves. The mean value from RAPGAP and DJANGOH is taken as the error.

Table 4.1: Experimental systematic uncertainties considered in the present analysis.

denotes the symmetric standard deviation. The correlation matrix C is calculated from the covariance matrix

$$C_{ij} = \frac{V'_{ij}}{\sqrt{V'_{ii}V'_{jj}}}, \tag{4.10}$$

and finally the covariance matrix for symmetrised errors reads:

$$V_{ij} = \bar{\delta}_i C_{ij} \bar{\delta}_j. \tag{4.11}$$

4.4 Combination of Data Sets

All unfolded histograms are available threefold, because of the separate analysis of the three data subsamples (compare section 3.1):

① proton beam momentum: $p_P = 820$ GeV, beam lepton: e^+

② proton beam momentum: $p_P = 920$ GeV, beam lepton: e^-

③ proton beam momentum: $p_P = 920$ GeV, beam lepton: e^+

Each unfolded histogram comes with a covariance matrix for the statistical and the systematical error. In this section it will be discussed how the results are combined. For completeness, in Appendix 6 all results are also given individually for the three data sets.

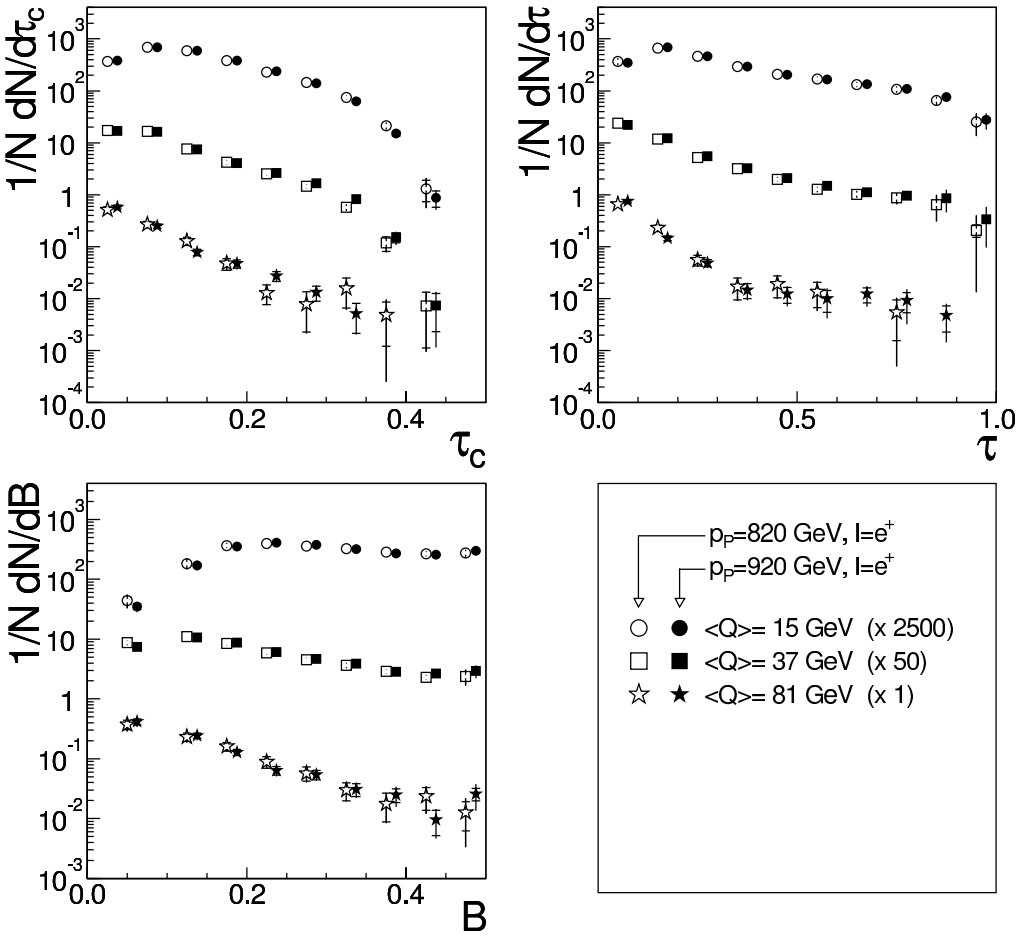

Figure 4.16: Event shape distributions unfolded for detector effects and QED radiation. Data sets with proton beam energies of 820 GeV and 920 GeV are compared, corresponding to a center of mass energy of 301 GeV and 318 GeV, respectively.

Fig. 4.16 compares positron data at two different proton beam energies (① and ③), three event shape variables are presented in three bins of Q each. The distributions are compatible within statistical errors. This is expected, because the difference in the center of mass energy amounts to 6%, corresponding to only small discrepancies in the mean values of Q and Bjørken x for all seven bins of Q. The variable with the strongest dependence on x among the studied event shapes is known to be thrust τ [57] (especially at high Q), however no discrepancies are visible here.

Consequently it appears sensible to average both sets of distributions. In order to take into account the different amount of data in ① and ③, the weighted mean values are computed, with the weight given by the inverse of the integrated luminosity. Accordingly, the resulting covariance matrices are calculated by error propagation, such that ① and ③ are assumed to be fully uncorrelated with respect to the statistical uncertainty, and fully correlated with respect to the systematical uncertainty. The latter assumption affects that the systematical errors are not reduced by the combination procedure, which is intended.

The effective center of mass energy of the combined e^+ sample amounts to 313 GeV, whereas the shifts of the central values of Q and x are considered and found to be not larger than 4%.

When combining this new set of histograms with sample ②, it is important to take into account not only the unequal center of mass energies, but also the different lepton charges. Equation 1.2 shows that a part of the total cross section, namely the xF_3 contribution, enters with opposite sign for e^+p and e^-p scattering. This contribution, generated by Z^0 exchange and γZ^0 interference, is noteworthy at high scales Q in the order of the Z^0 mass.

For the normalised event shape distributions, any change in the total cross section cancels. However, the coupling of the neutral vector bosons (γ and Z^0) to quark/antiquark pairs differs, because of the additional axial vector coupling of the Z^0. Therefore in general a difference is anticipated between event shapes measured in e^+p and e^-p scattering [64] at high Q. This difference is however expected to be small.

Fig. 4.17 shows three event shape variables in three bins of Q, separately for e^+ (combined) and e^- data. While the data sets at lower Q show no distinctive features, for the highest Q bin shown one could argue that some discrepancy in the slope is present, which is not covered by the errors.

There is a NLO Monte Carlo program including electroweak contributions, MEPJET [16], but because of the employed phase space slicing method it is not suited for the determination of event shape distributions [25]. Moreover MEPJET has been found to give substantially different results compared to DISENT and DISASTER++ [65].

Unfortunately, the state-of-the-art NLO calculations used in this work (DISENT, DISASTER++ and NLOJET++) do not include Z^0 exchange, hence possible discrepancies due to differing matrix elements can not be studied here.

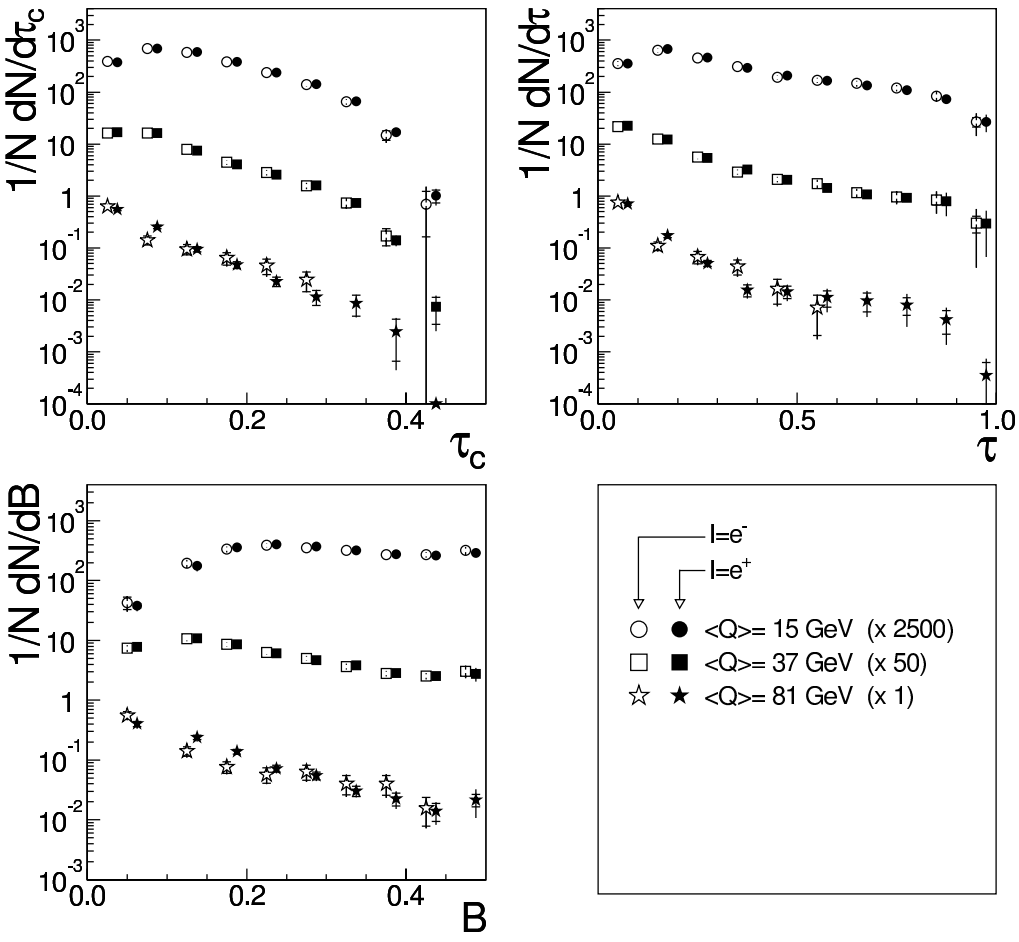

Figure 4.17: Event shape distributions unfolded for detector effects and QED radiation. Data sets for e^+p and e^-p scattering are compared.

# of Q bin	1	2	3	4	5	6	7
Interval/ GeV	[14,16]	[16,20]	[20,30]	[30,50]	[50,70]	[70,100]	[100,200]
$\langle Q \rangle$/ GeV	14.93	17.75	23.81	36.84	57.58	80.59	116.34
$\langle x \rangle$	0.00871	0.01196	0.02011	0.04622	0.10842	0.18450	0.30008

Table 4.2: Mean values of Bjørken x and momentum transfer Q for the bins of the combined data set.

If the effect is really as large as Fig. 4.17 suggests, fits to theories including only photon exchanges are problematic. Following a suggestion from M. Dasgupta and G. Salam [64], the effect can be lessened, if the cross section weighted distributions from e^+ and e^- data are used:

$$\frac{1}{\sigma^{\text{mean}}}\frac{\mathrm{d}\sigma^{\text{mean}}}{\mathrm{d}F} = \int_{Q-\text{bin}} \mathrm{d}x\mathrm{d}Q^2 \frac{\dfrac{\mathrm{d}^3\sigma^{e^+}}{\mathrm{d}x\mathrm{d}Q^2\mathrm{d}F} + \dfrac{\mathrm{d}^3\sigma^{e^-}}{\mathrm{d}x\mathrm{d}Q^2\mathrm{d}F}}{\dfrac{\mathrm{d}^2\sigma^{e^+}}{\mathrm{d}x\mathrm{d}Q^2} + \dfrac{\mathrm{d}^2\sigma^{e^-}}{\mathrm{d}x\mathrm{d}Q^2}}. \tag{4.12}$$

This way the part proportional to xF_3 cancels. The determination of the combined covariance matrices is made in analogy to the combination described above for the 820 GeV and 920 GeV data, the weights used here are the cross sections instead of the luminosities.

The remaining problem are the F_2 and F_L parts, where the relative weights of the different quark flavours are also modified by the Z^0 contributions. In principle this could be accounted for by a modification of the effective quark charges in the calculations, but this has not been done yet.

A practical drawback of the cross section weighted distributions stems from the fact that H1 has collected roughly six times more e^+p than e^-p data. Because of this asymmetry the statistical uncertainty of the combined result is degraded, compared to a scenario where an equal amount of data were available. However, this effect is somewhat attenuated: at high Q, where statistics plays the major rôle, the inclusive cross section for e^-p scattering is significantly larger than for e^+p scattering. At the highest Q bin in the presented analysis, the cross section for e^-p is twice as large as for e^+p.

In the following, all results are given for the weighted means according to equation 4.12, this way the fits to the pure electro-magnetic theory calculations are better founded.

4.5 Results on Distributions

Fig. 4.18-4.20 show the measured unfolded event shapes distributions. Depicted is the non radiative hadron level together with theory histograms for comparison. The

normalised cross sections are not bin center corrected, hence also the theory (which could be binned fine enough to display a smooth curve) is given integrated over the bins.

These distributions are a main result of the presented work.

- 2-jet Event Shapes
  The five studied 2-jet event shapes are well established observables. The measurement is precise, which is reflected by a small systematic error for most part of the phase space. Since no severe cuts are made in the definition of these variables, the full data statistics is exploited, hence only the highest Q bins are statistically limited.

  A strong dependence of the shapes on the scale Q demonstrates their sensitivity to quantum chromo dynamics. Sophisticated theory calculations are available, which allow for a QCD fit. The result of the fit, which is described in the following chapter in more detail, is already here shown for the 2-jet event shapes in comparison. Even if not applicable for the full range of phase space, the perturbative calculations together with power corrections provide a close description of the data.

- 3-jet Event Shapes
  Out-of-event plane momentum and azimuthal correlation were only recently introduced for deep inelastic scattering. The present work shows the first measurement of this quantities. As described in section 1.3.2, a cut on y_2 is made in their definition, which reduces the statistics of the data compared to the 2-jet event shapes.

  Unfortunately a resummed and matched calculation is only almost finished at the time of completion of this thesis, thus no QCD fit can be performed. Instead, the data is compared to RAPGAP, which at large describes the data. On the other hand, discrepancies are visible for the azimuthal correlation at the 2-jet limit (at low values) and at high scales.

- Jet Rates
  Of the observables shown here, only the 2-jet rate has been studied before in detail in DIS [14]. The distributions are strongly peaked at zero, hence usually the logarithm of the jet rates is studied.

  It is expected that the measurement gets difficult with increasing jet multiplicity, because of the decreasing cross section and the growing importance of the limited detector resolution. This is reflected in the large experimental errors of the 4-jet rate.

  Attempts of an α_s fit to the jet rates with fixed order calculations and hadronisation corrections showed no success in the context of this work. Thus y_2 and y_3 are displayed together with predictions from NLOJET++ at a literature

value of $\alpha_s = 0.118$, and y_4 together with a distribution determined by the RAPGAP event generator. The description is in all cases good.

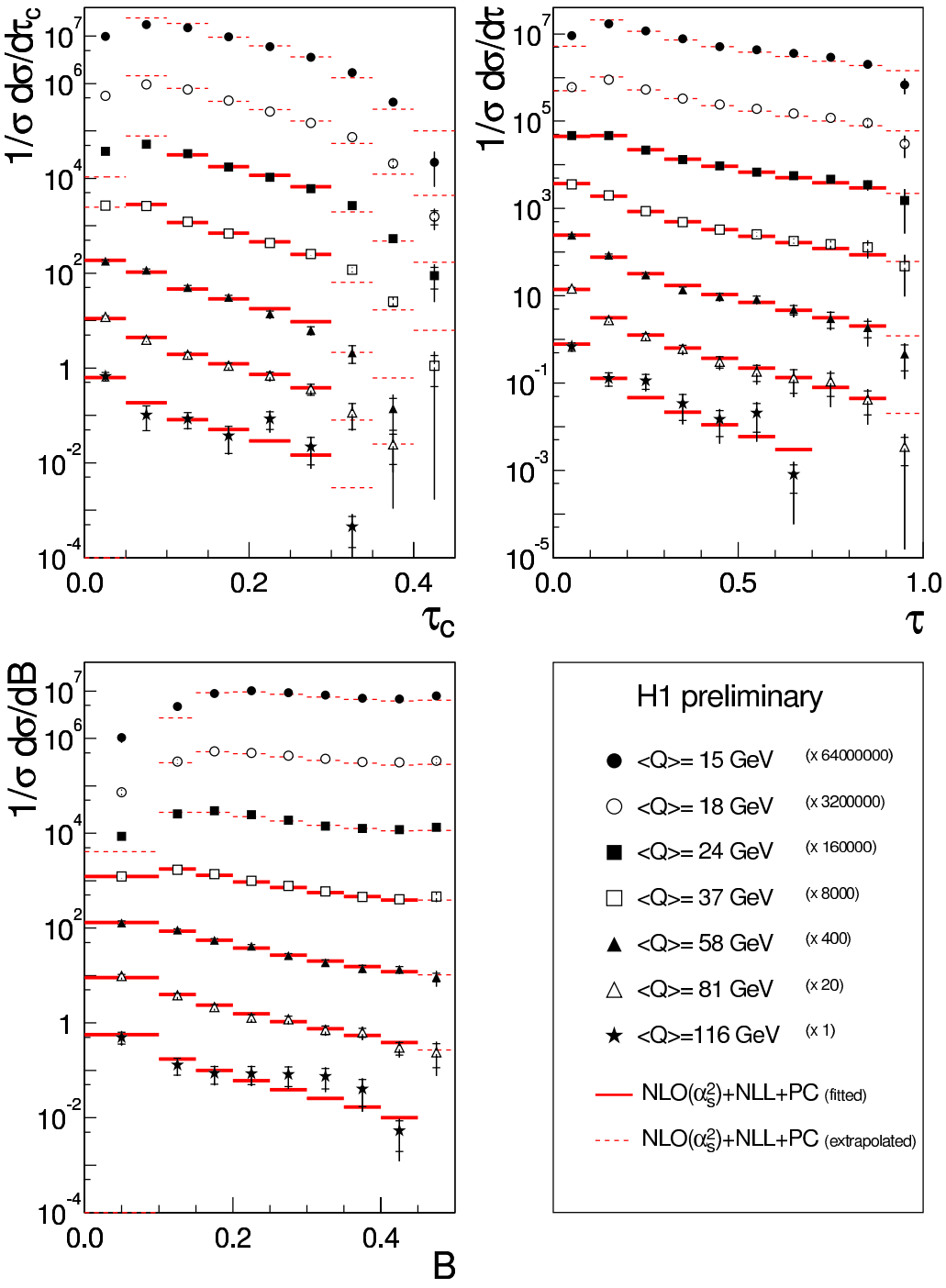

Figure 4.18: Measured distributions at non radiative hadron level. The data are compared with the results of a fit based on NLO QCD including resummation and power corrections. The fit predictions are shown with dashed lines for those data points which were not included in the fit.

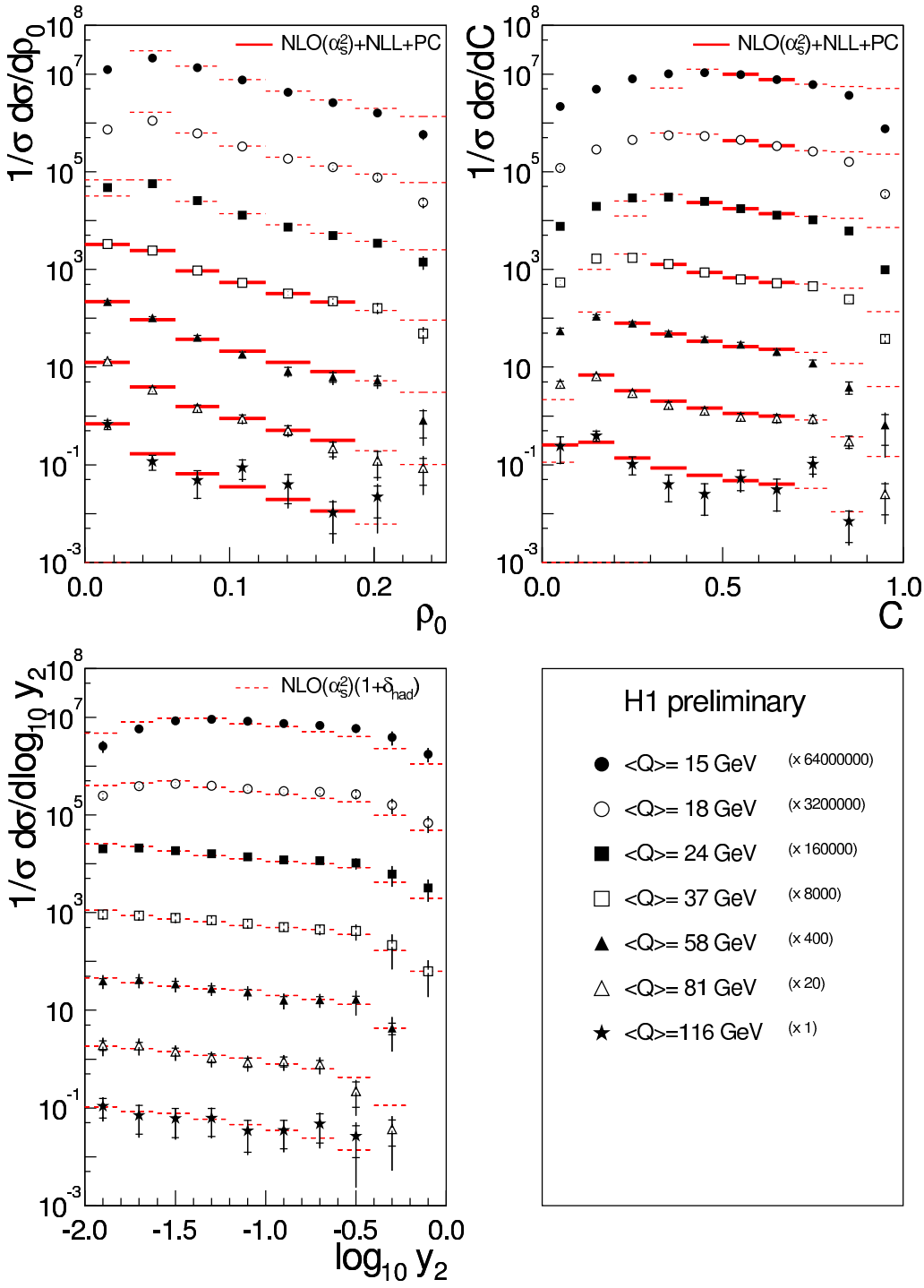

Figure 4.19: Measured distributions at non radiative hadron level. For the jet mass ρ_0 and the C-parameter, the data are compared with the results of a fit based on NLO QCD including resummation and power corrections. The fit predictions are shown with dashed lines for those data points which were not included in the fit. The jet rate y_2 is compared to a calculation based on NLOJET++, where hadronisation corrections are determined with RAPGAP.

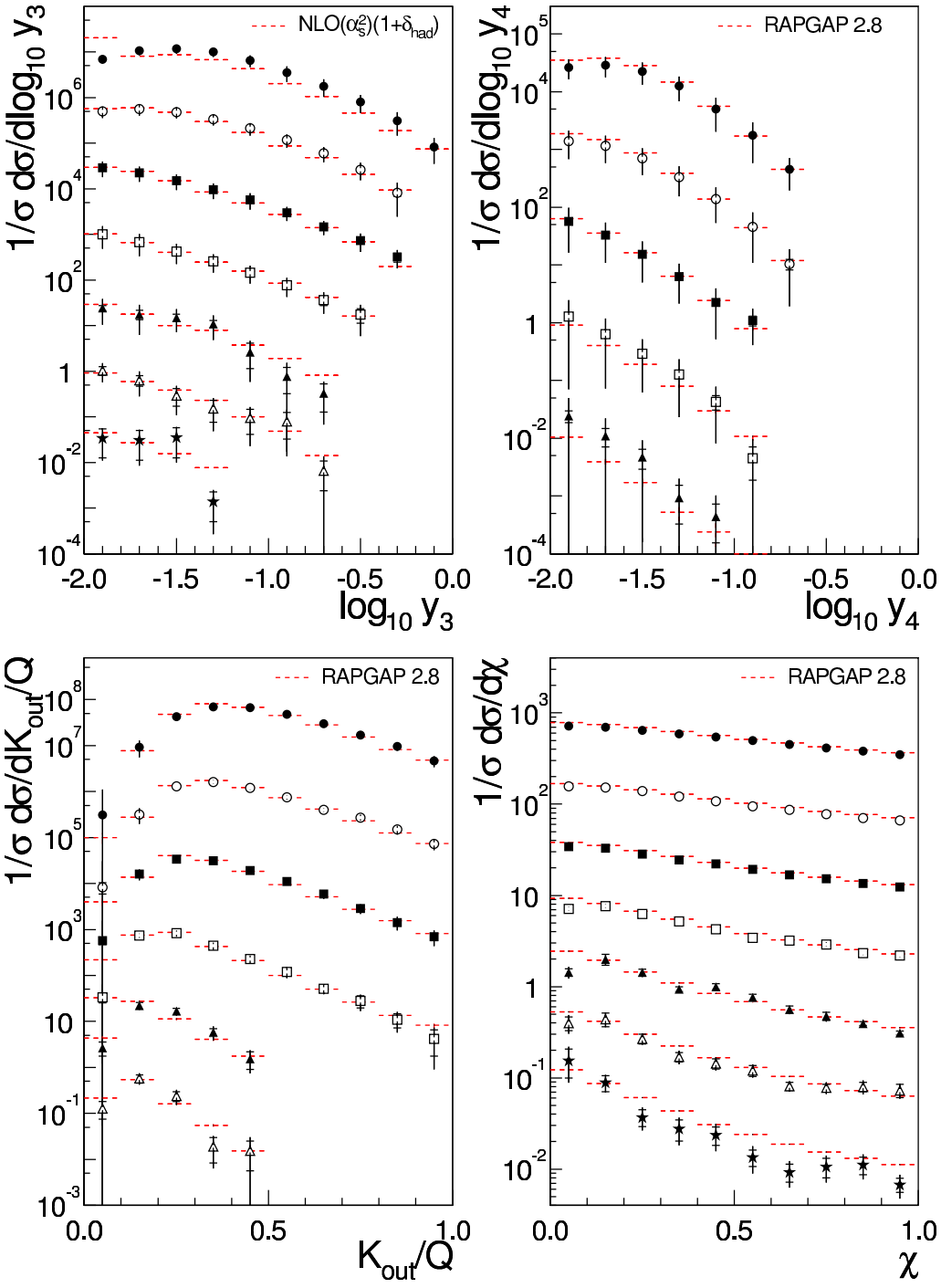

Figure 4.20: Measured distributions at non radiative hadron level. The jet rate y_3 is compared to a calculation based on NLOJET++, where hadronisation corrections are determined with RAPGAP. All other variables are compared to RAPGAP.

4.6 Results on Mean Values

The present work focuses on differential distributions of event shape variables. In order to allow for a comparison to former analyses of 2-jet event shapes, also mean values of this distributions are determined.

Different methods exist for the extraction of mean values, which are studied in more detail in [57]. One possibility is to calculate the mean value from the unfolded distributions. This method introduces a bias, at least in principle, because of the finite bin widths, but has been shown to be less model dependent. In order to reduce the bias, the distributions were unfolded with a finer binning (20 bins like in [57]), before the mean values were calculated.

Fig. 4.21 shows the mean values of the 2-jet event shapes as a function of the scale Q. The present analysis is compared to the previous H1 analysis [14] and to results from the ZEUS collaboration [66]. All three measurement are compatible to each other within errors. However, the deviations between the new and the published H1 data seem to be correlated between the bins, e.g. the new results are always higher for thrust τ and always lower for the jet mass ρ_0. This could be explained by correlated systematic uncertainties, because both analyses employ different electromagnetic and hadronic calibrations, which introduce correlations between the bins.

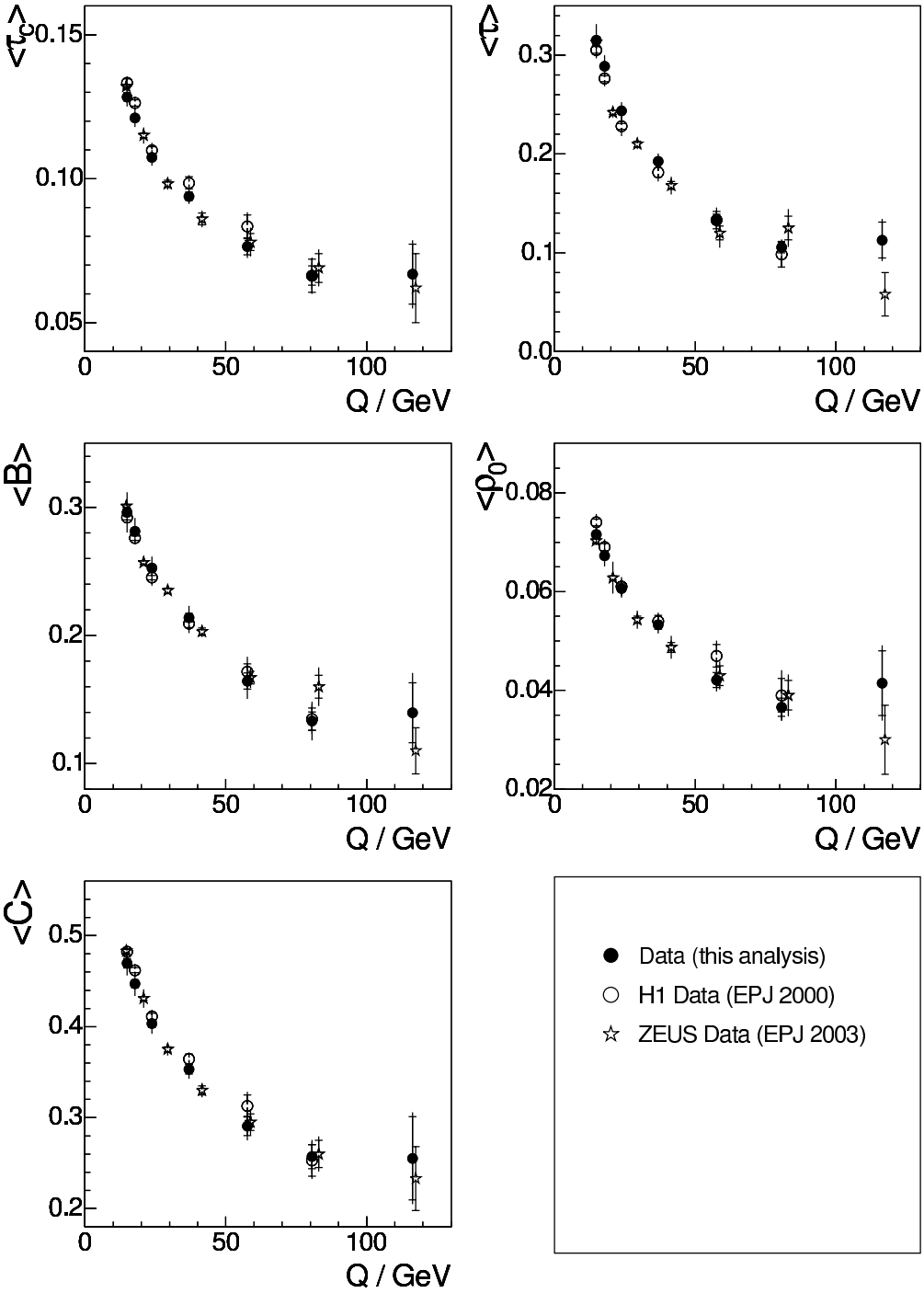

Figure 4.21: Mean value of event shapes variables as a function of the scale Q.

Chapter 5

QCD Analysis

In previous analyses dealing with mean values of event shape variables in deep inelastic scattering, fits to the data have been performed, based on fixed order theory calculations plus power corrections [14, 66]. The free parameters of such simultaneous fits are the strong coupling α_s and the average effective coupling α_0.

Missing resummed terms in the fixed order calculations prevented an application of these fits on differential distributions. Now resummed and matched calculations are available for the most common 2-jet event shapes. This results in an extension of the description to the exclusive limit, i.e. to low values of the event shape variables.

In consequence, it appears now promising to fit the event shape spectra. The motivation being, to check if the concept of power corrections is universal in that sense, that it holds for mean values as well as for the distributions.

In addition the spectra offer two advantages when it comes to a test of QCD: Firstly, the shape of the distributions is governed by QCD effects and offers hence supplementary sensitivity compared to the mean value. Secondly, regions where the calculations are known to have weaknesses can be excluded from the fit, in order to focus on the parts which are well under control.

In the following, the tools used for the QCD test are briefly introduced, then the result of fits to distributions is presented. As a cross check, fits to mean values are also shown.

5.1 Theory Calculations

Foundations of perturbative and non perturbative calculations of event shape variables have been introduced in Section 1.2. In [24] and [25], the actual resummation and matching was presented by M. Dasgupta and G. Salam, and also a first comparison to H1 data was made. The results of the calculations are available by means of two programs, called DISPATCH and DISRESUM.

5.1.1 DISPATCH

DISPATCH calculates spectra of event shape variables in next-to-leading order via an interface to DISENT 0.1 [17] and DISASTER++ 1.0.1 [18]. The latter are multi purpose Monte Carlo programs, which include the matrix elements for 1-jet and 2-jet like quantities in next-to-leading order QCD perturbation theory for DIS. DISPATCH offers an unified user interface and in addition saves computing time when several points on a (x, Q^2) grid are to be determined.

Input to the program are the points of (x, Q^2) at which the distributions are to be calculated as well as the set of parton density functions of the proton to use. The result is then given in terms of perturbative coefficients c_1 and c_2, compare equation 1.7:

$$R_{\mathrm{NLO}}(F) = 1 + c_1(F)\alpha_s + c_2(F)\alpha_s^2.$$

It has been shown [67] that some logarithmically enhanced terms are incorrect in DISENT. Consequently, certain event shape mean values obtained with DISENT deviate from those obtained with DISASTER++. Even though the effect is much reduced in the case of distributions [25], the present work uses DISASTER++ for the main calculations and DISENT only for a cross check.

Three high statistics coefficient sets were calculated for the present work, based on one billion events each:

- DISASTER++ 1.0.1 with three sets from the proton p.d.f MRST2001 [68] ($\alpha_s(m_Z) = 0.117$, $\alpha_s(m_Z) = 0.119$, $\alpha_s(m_Z) = 0.121$),
- DISASTER++ 1.0.1 with proton p.d.f CTEQ5M1 [41] ($\alpha_s(m_Z) = 0.118$),
- DISENT 0.1 with three sets from the proton p.d.f MRST2001 (see above).

5.1.2 DISRESUM

In a second step the fixed order result is read by DISRESUM, which applies the matching of the resummed terms and the power correction. Several options are available for the matching of the resummed to the fixed order part. Tab. 5.1 lists the matching schemes used for the fits to follow.

Detailed information on the definition of the schemes can be found in [24]. The "modified" $\log R$ matching assures correct upper limits of the distributions, and is recommended as the standard scheme. However, it was found in this work that for three event shape variables a better description in terms of χ^2 is obtained by the pure $\log R$ matching. Consequently, the scheme with the best description is chosen, together with a supplementary one for the systematic variation. In case of the jet broadening, the alternative scheme which is used is called M_2 and was invented in [24] within the context of the jet broadening resummation.

Event Shape	nominal matching scheme	varied matching scheme
τ_c	modified $\log R$	$\log R$
τ	$\log R$	modified $\log R$
B	$\log R$	M_2
ρ_0	modified $\log R$	$\log R$
C	$\log R$	modified $\log R$

Table 5.1: Matching schemes used for the central fit and the systematic variation.

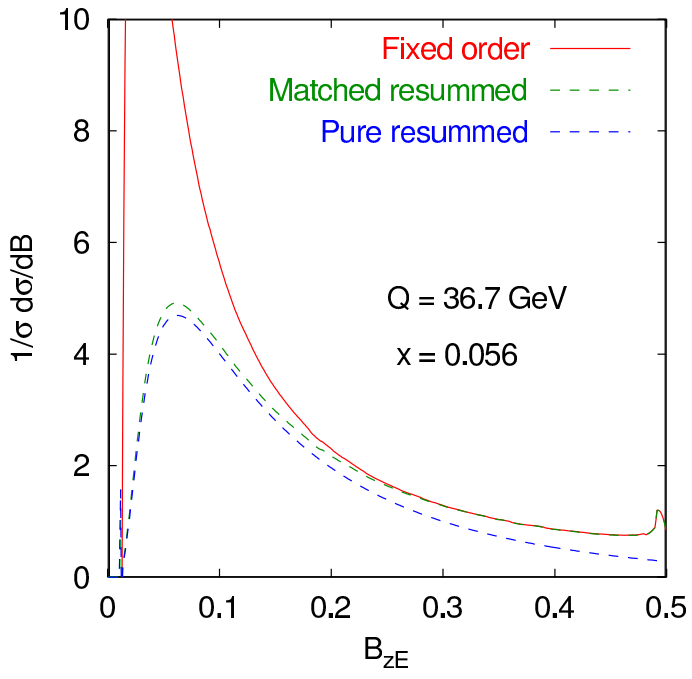

Figure 5.1: Comparison of resummed distributions with fixed order (NLO) results. Non-perturbative hadronisation corrections are not included. The matching scheme is the modified M matching. Figure taken from [25].

Fig 5.1 shows the fixed order, the resummed and the matched resummed results exemplarily for the Jet Broadening. The matched resummed distribution resembles the pure resummed calculation at low B and, accordingly, the fixed order calculation at high B.

For any given value of the free parameters $\alpha_s(\mu_r)$ and $\alpha_0(\mu_I)$, DISRESUM calculates the normalised distributions of the event shapes.

The parameter $\alpha_s(\mu_r)$ is the **renormalised** strong coupling constant, which is invented to absorb ultraviolet divergences occuring in the calculation of self energy loop Feynman diagrams [6]. One speaks then of the "running coupling", where the dependence on μ_r is determined by the renormalisation group equation:

$$\mu_r^2 \frac{\partial \alpha_s}{\partial \mu_r^2} = \beta(\alpha_s), \tag{5.1}$$

where the beta function is perturbatively calculable. There exist different renormalisation schemes, where in this work the $\overline{\text{MS}}$ scheme [69] is employed.

The renormalisation scale is set to a characteristic scale of the process under study, which is for the present work chosen to be the modulus of the four momentum Q. Any dependence of the perturbative predictions on μ_r is an artifact, generated because higher orders are neglected. It is common practice to evaluate the uncertainty due to this missing higher orders of perturbative results by varying the renormalisation scale μ_r by factors 2 and 1/2. This is also done in the presented analysis.

$\alpha_s(\mu_r)$ is fixed by the renormalisation group equation for the whole defined interval if its magnitude is given at only one value of μ_r, which is by convention chosen to be the mass of the Z^0 boson. DISRESUM expects the value of the strong coupling constant expressed at the renormalisation scale, i.e. $\alpha_s(Q)$ needs to be given. In this work, the data are spanning a large interval of the scale Q. In order to combine determinations of the strong coupling constant at different scales, the individual results are evolved to the common scale m_Z with the help of the renormalisation group equation.

The first moment of the effective coupling, α_0, depends explicitly on the infrared matching scale μ_I, where the infrared finite coupling coincides with the normal perturbative one. This scale is chosen to be $\mu_I = 2\,\text{GeV}$ and varied by $\pm 0.5\,\text{GeV}$ to estimate the theoretical uncertainty due to this arbitrary choice.

Fig. 5.2 compares the measured data to different variants of the theory prediction. Values of α_s and α_0 are always taken from a fit of the full theory to the data. Certain constituents of the theory are omitted in three of the diagrams, to show the impact of the resummation and the power corrections. It is obvious from the upper left plot, that the next-to-leading order calculation alone is not able to describe the data at any part of the distribution.

When power corrections are added (upper right diagram), the drop at the leftmost bin is reproduced. This drop can be understood as the broadening of a parton

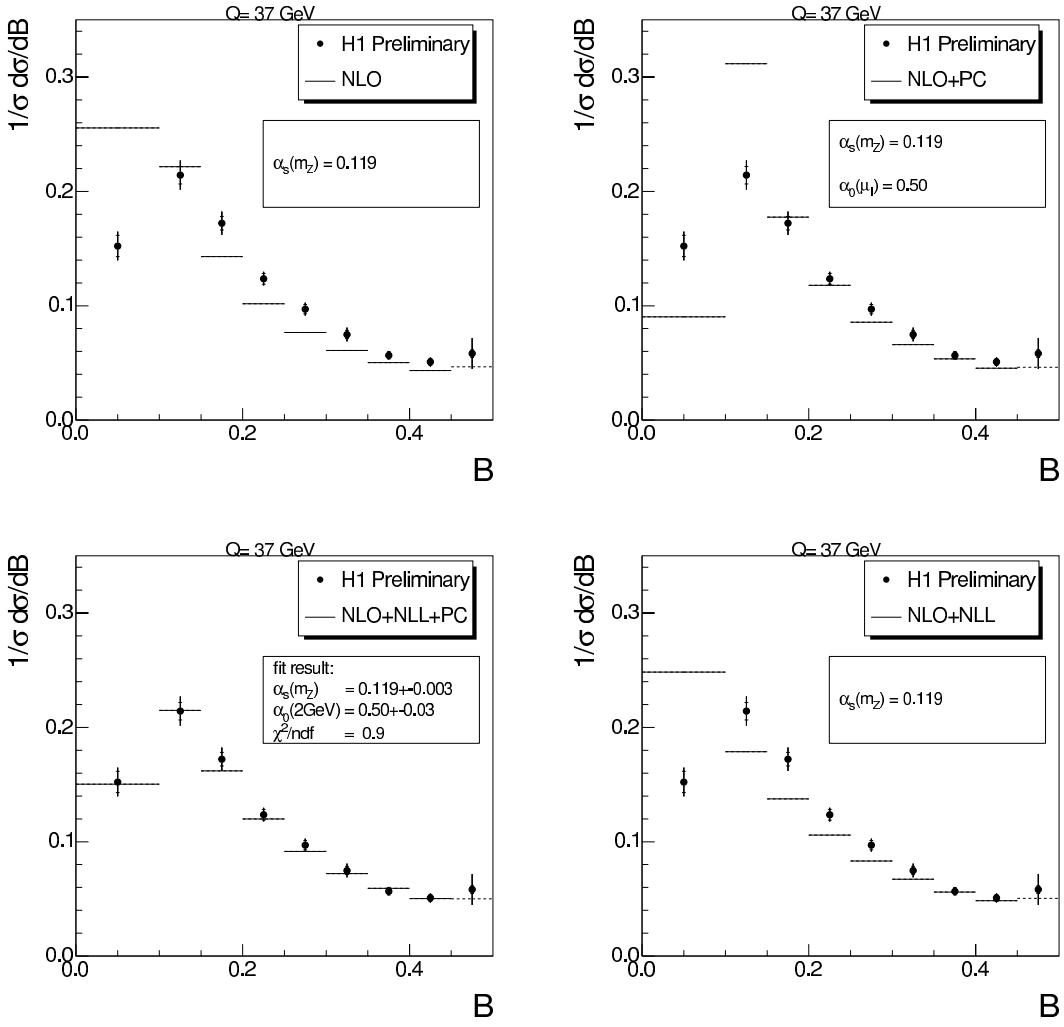

Figure 5.2: The jet broadening in a comparison of data and theory. In turn, individual building blocks of the full theory are not included, to underline the effect of power corrections and resummation.

configuration due to hadronisation, resulting in a shift of the events to higher values of B. Still, the theory histogram at the lower third of the abscissa is far off the data.

Addition of the resummed terms, shown on the lower left diagram, leads to a close description of the data, the fit results shown in the box meet expectations. The effect of resummation appears most prominent at the two leftmost bins.

Finally, the lower right sub-diagram, where the power correction is leaved out again, proves that the hadronisation is the major effect which needs to be included. The resummation extends the prediction to low values of the event shape variable.

5.2 Fit Procedure

All fits were performed with the help of the MINUIT [70] package. The MIGRAD procedure is chosen as the strategy for the fits, which is an implementation of the Newton Method and involves the calculation of the Hessian matrix.

How well the data is described by the theory for a set of fit parameters is expressed in the quantity χ^2, which is hence minimised by MINUIT. In this analysis, the χ^2 for one event shape in one Q bin is defined as

$$\chi^2 = \Delta_i V_{ij}^{-1} \Delta_j, \qquad \Delta_i = m_i - t_i(\alpha_s, \alpha_0), \tag{5.2}$$

with V the covariance matrix, m the measured data points and $t(\alpha_s, \alpha_0)$ the theory prediction, which depends on the free parameters. Following a proposal in [71], the covariance matrix V which holds absolute uncertainties, is determined as

$$V_{ij} = \frac{m_i + t_i}{2} W_{ij} \frac{m_j + t_j}{2}, \tag{5.3}$$

where W is the covariance matrix with respect to the relative uncertainties. W is build as a sum of the individual covariances matrices from sources of uncertainty, which were presented in chapter 4, corresponding to the errors added in quadrature:

$$W = W_{\text{stat}} + W_{\text{elm.escale}} + W_{\text{had.escale}} + W_{\text{e.track}} + W_{\text{model}} + W_{\text{unfold}}, \tag{5.4}$$

where the model and unfolding uncertainties are treated uncorrelated, i.e. these covariance matrices are diagonal.

For a combined fit of several Q bins, the individual χ^2 are simply added. In consequence, correlations between these bins are ignored, which is correct concerning the statistical error (the data are disjoint w.r.t. the Q bins). However, possible correlations due to systematic uncertainties are neglected at this stage, which leaves room for improvement.

When it comes to fits of the spectra, the interval of the distributions has to be determined. The upper bounds are more or less unambiguously given in [25], motivated by properties of the calculations. As an example, the LO prediction for the C-parameter vanishes for values greater than $3/4$, rendering the NLO calculation

effectively only at LO precision in this region. Therefore the fits in this work are restricted to $C < 0.7$.

It is not so clear how to choose the lower bounds of the fit intervals. The power corrections are expected to limit the reliability of the prediction, depending on Q. In [25] the bin center of the lower limit was chosen to scale with $1/Q$. The present analysis tries to extend the fit interval to low values.

In a scan, bins were successively included, starting at high values of the event shape variable, unless the total χ^2 of the fit increased not dramatically (a $\Delta\chi^2$ of less than four was required). As can be seen from Fig. 4.18-4.19, in most of the cases even the lowest bin could be included. This may appear ambitious, but one has to keep in mind that this way the distribution is not probed down to zero, which would be unsafe. Instead, with the lowest bin one tests the distribution integrated up to the upper bin boundary, which is potentially acceptable [25]. The effect of the leftmost bins included or not is evaluated in a systematic study and included in the theoretical uncertainty.

The inclusion of whole Q bins to the fit of each event shape was determined in a similar way, starting with the highest scales and adding lower bins until the description, evaluated by $\Delta\chi^2$, gets worse.

5.3 Fits to Distributions

The results for α_0 and α_s in the form of 1σ contours are given in Fig. 5.3. For comparison a determination of the average value and error of α_s [5] is shown as a band. A negative correlation coefficient between α_s and α_0 is found for all variables. The universal non-perturbative parameter α_0 is consistent to 0.5 within 10%. The 1σ contours correspond to the statistical and experimental systematic uncertainties added in quadrature.

In order to estimate the magnitude of the theoretical error, the following variations are applied:

- Usage of $2Q$ and $Q/2$ as the renormalisation scale μ_r[1].
- The infrared matching scale is set to $\mu_I = 1.5\,\mathrm{GeV}$ and $\mu_I = 2.5\,\mathrm{GeV}$.
- The leftmost bins, which include the the value of zero for the event shape, are omitted from the fit intervals.
- The value of the strong coupling constant used in the MRST2001 proton p.d.f. is varied from 0.119 to 0.117 and 0.121.
- The proton p.d.f. is taken from CTEQ5M1 ($\alpha_s(m_Z) = 0.118$).

[1] This variation is often quoted as $\mu_r^2 \cdot 4$ and $\mu_r^2/4$.

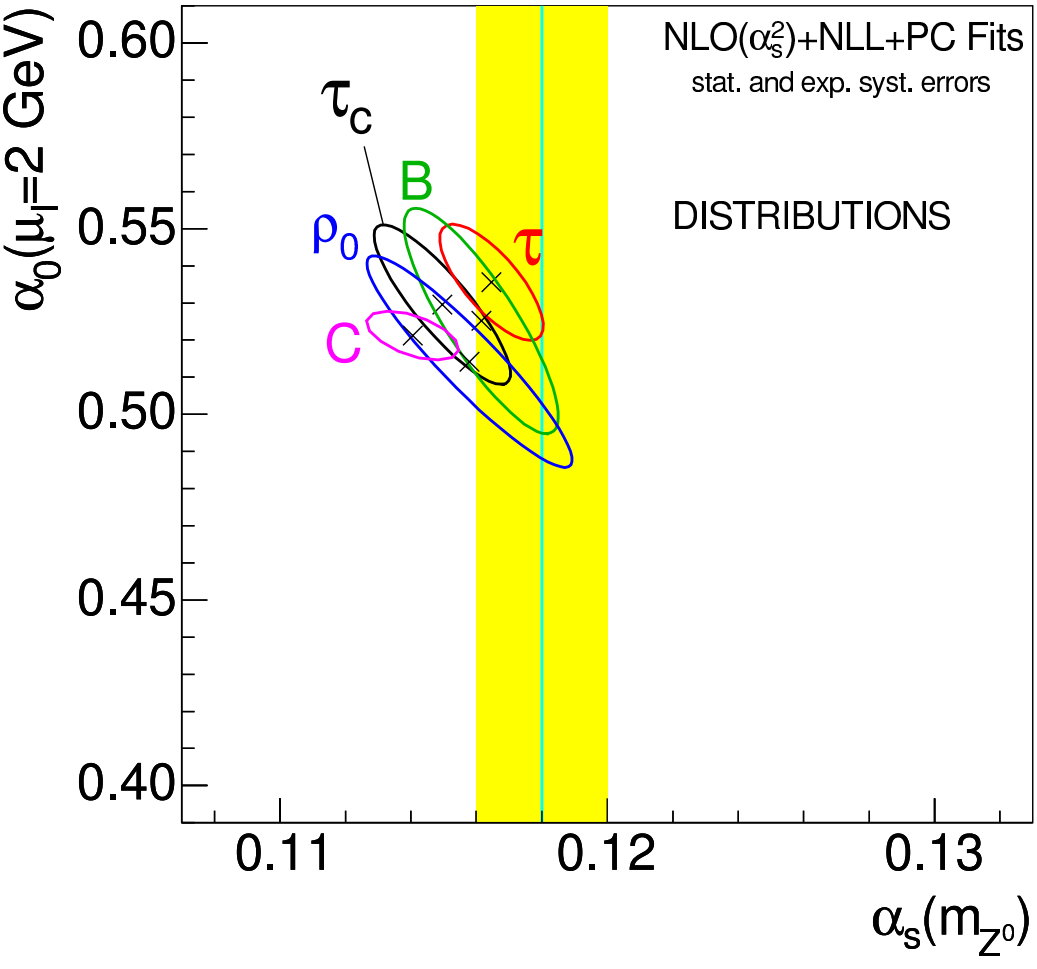

Figure 5.3: 1-σ contours in the (α_s, α_0) plane from fits to the 2-jet event shape differential distributions. The α_s band is taken from [5].

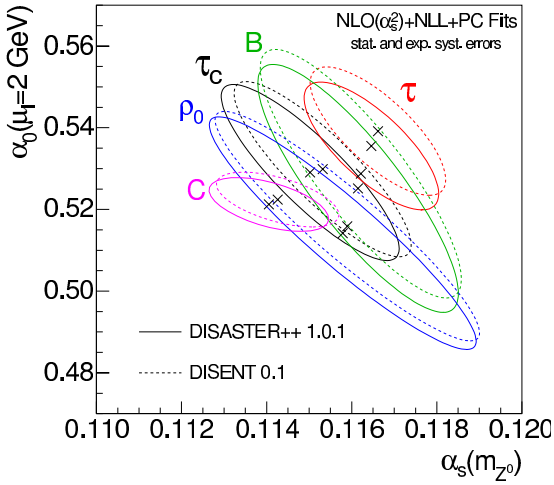

Figure 5.4: 1-σ contours in the (α_s, α_0) plane from fits to the 2-jet event shape differential distributions. Comparison between DISENT and DISASTER++.

- An alternative matching scheme is chosen (compare section 5.1).

The fit procedure was individually repeated for any of these variations. It has been shown in [25] that the effect of a modification of the factorisation scale by a factor of 2 can be safely neglected for the phase space under study, hence this variation was not done in the present analysis. Many more systematic studies were performed in [25], where it has been found that the total systematic uncertainty is mainly determined by the renormalisation scale.

All fit results are given in numerical form in Tab. 5.2. As in many QCD analyses, the theoretical error is the dominant contribution to the total uncertainty. The goodness of the fit is expressed in terms of χ^2 per degree of freedom. It tends to be greater than one, with τ_c being the worst case, which indicates imperfections of the theoretical assumption or underestimated experimental errors.

Fig. 5.4 shows the fit results obtained with DISENT together with the central result. The deviations are only small when compared to the theoretical and systematical errors.

Results from a recent analysis of e^+e^- data by the DELPHI collaboration are shown in Fig. 5.5. Three of the event shape variables may be compared to the work on hand: Thrust $1-T$ (τ_c in DIS), C Parameter and jet mass $M^2_{sE}/E^2_{\mathrm{vis}}$ (ρ_0 in DIS). Contrary to the presented analysis, the LEP data are statistically limited at low scales, because most of the data were taken at energies matching the Z^0 mass or higher.

While a direct one-to-one comparison may be problematic, it is interesting to note

strong coupling constant $\alpha_s(m_Z)$					
event shape variable	τ_c	τ	B	ρ_0	C
central value	0.1150	0.1165	0.1161	0.1158	0.1141
uncertainties:					
total	$^{+0.0061}_{-0.0047}$	$^{+0.0057}_{-0.0042}$	$^{+0.0053}_{-0.0036}$	$^{+0.0066}_{-0.0058}$	$^{+0.0053}_{-0.0057}$
total experimental	± 0.0021	± 0.0016	± 0.0024	± 0.0031	± 0.0014
statistical exp.	± 0.0009	± 0.0007	± 0.0010	± 0.0016	± 0.0005
systematical exp.	± 0.0019	± 0.0014	± 0.0021	± 0.0027	± 0.0013
total theoretical	$^{+0.0057}_{-0.0043}$	$^{+0.0054}_{-0.0039}$	$^{+0.0047}_{-0.0027}$	$^{+0.0058}_{-0.0048}$	$^{+0.0051}_{-0.0055}$
μ_r dependence	$^{+0.0057}_{-0.0041}$	$^{+0.0054}_{-0.0038}$	$^{+0.0044}_{-0.0027}$	$^{+0.0058}_{-0.0044}$	$^{+0.0051}_{-0.0052}$
μ_I dependence	$<10^{-4}$	$^{+0.0001}_{-0.0001}$	$<10^{-4}$	$^{+0.0001}_{-0.0001}$	$^{+0.0001}_{-0.0003}$
fit interval	± 0.0002	± 0.0005	± 0.0007	± 0.0004	± 0.0005
parton density functions	$^{+0.0002}_{-0.0001}$	$^{+0.0006}_{-0.0006}$	$^{+0.0006}_{-0.0006}$	$^{+0.0003}_{-0.0003}$	$^{+0.0002}_{-0.0002}$
matching scheme	-0.0013	$+0.0003$	$+0.0016$	-0.0020	-0.0016
NP effective coupling $\alpha_0(\mu_I)$					
event shape variable	τ_c	τ	B	ρ_0	C
central value	0.5290	0.5355	0.5252	0.5142	0.5212
uncertainties:					
total	$^{+0.0336}_{-0.0370}$	$^{+0.0212}_{-0.0272}$	$^{+0.0563}_{-0.0334}$	$^{+0.0380}_{-0.0397}$	$^{+0.0243}_{-0.0442}$
total experimental	± 0.0216	± 0.0156	± 0.0304	± 0.0285	± 0.0066
statistical exp.	± 0.0074	± 0.0068	± 0.0123	± 0.0131	± 0.0021
systematical exp.	± 0.0202	± 0.0141	± 0.0277	± 0.0253	± 0.0062
total theoretical	$^{+0.0258}_{-0.0301}$	$^{+0.0144}_{-0.0223}$	$^{+0.0474}_{-0.0140}$	$^{+0.0251}_{-0.0276}$	$^{+0.0234}_{-0.0437}$
μ_r dependence	$^{+0.0177}_{-0.0300}$	$^{+0.0133}_{-0.0206}$	$^{+0.0137}_{-0.0135}$	$^{+0.0186}_{-0.0275}$	$^{+0.0233}_{-0.0261}$
fit interval	± 0.0032	± 0.0053	± 0.0452	± 0.0017	± 0.0003
parton density functions	$^{+0.0009}_{-0.0008}$	$^{+0.0027}_{-0.0027}$	$^{+0.0035}_{-0.0032}$	$^{+0.0020}_{-0.0020}$	$^{+0.0007}_{-0.0007}$
matching scheme	$+0.0188$	-0.0078	-0.0023	$+0.0168$	-0.0351
correlation coefficient α_s,α_0	-0.86	-0.75	-0.85	-0.93	-0.54
χ^2 / No. d.o.f. (exp. errors)	2.03	0.88	1.42	1.27	1.47

Table 5.2: Results of fits for event shape distributions.

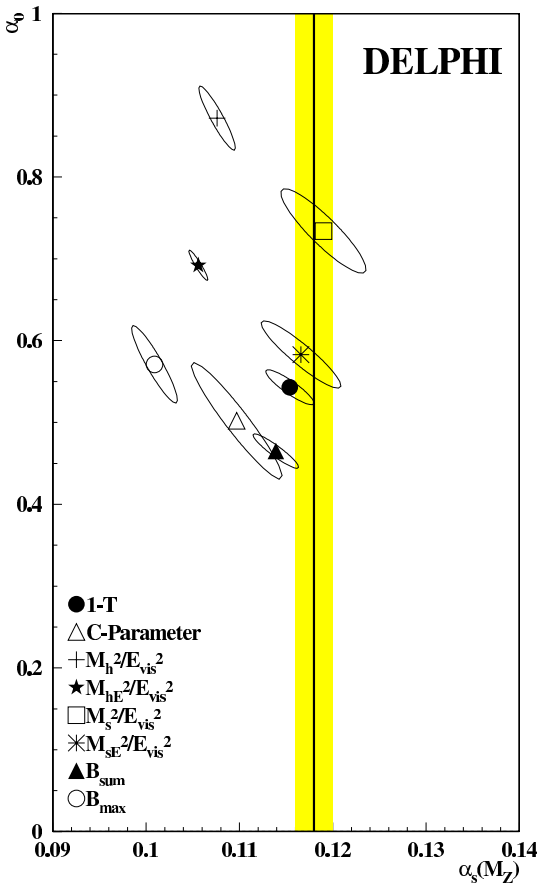

Figure 5.5: 1-σ contours in the (α_s, α_0) plane from fits to the 2-jet event shape differential distributions by the DELPHI collaboration. The fits are based on LEP e^+e^- data of center of mass energies from 45 GeV to 202 GeV. The contours correspond to statistical and experimental systematical errors added in quadrature.

similarities between the presented analysis and that by the DELPHI collaboration: for the three mentioned event shape variables the value of α_s is somewhat below the world mean, and α_0 lies in the interval from 0.5 to 0.6.

As a cross check of the fit results shown in Fig. 5.3, fits of the distributions for individual Q bins are performed. Still, a common value of α_0 is required, which e.g. for the C-parameter results in a fit of eight free parameters. Again, no correlations between the Q bins are included in the χ^2 definition. On the other hand, the mutual correlation of all $\alpha_s(Q)$ to the common α_0 introduces also a correlation between the $\alpha_s(Q)$ (typically around 10%).

Fig. 5.6 shows the result of this fit. The points denote the value of α_s against the scale Q, together with the total experimental error. The running of the renormalised strong coupling is well demonstrated

For comparison, the results of the combined fit (compare Fig. 5.3) are shown as bands, determined with the renormalisation group equation. The outer band denotes the total error, the inner band corresponds to the experimental error. For all event shapes a consistent picture is maintained.

It appears tempting to quote an overall average of $\alpha_s(m_Z)$ from all five event shape variables. This is not without difficulties, because the observables are highly correlated to each other, which has to be taken into account, in order not to underestimate the total error.

A rather simplified treatment of the correlations is used in this work. Firstly the sample correlation coefficients between all pairs of event shapes F_1 and F_2 are determined [58]

$$\rho_{12} = \frac{\overline{F_1 F_2} - \overline{F_1}\,\overline{F_2}}{\sqrt{\overline{F_1^2} - \overline{F_1}^2}\sqrt{\overline{F_2^2} - \overline{F_2}^2}}, \tag{5.5}$$

where the mean values are build for the RAPGAP sample on hadron level. These coefficients are displayed in Fig. 5.7. It is obvious from the figure, that there are two classes of highly correlated observables: on the one hand the variables which make explicit use of the virtual boson axis (τ and B), and on the other hand the variables which do not (τ_c, ρ_0 and the C-parameter).

Now the assumption is made, that the correlations between the fitted values of α_s are not too different from those of the event shapes themselves (which neglects that the theory calculations may have different properties).

In consequence, the correlation coefficients from Fig. 5.7 are used for a combined fit of all five event shape variables, the outcome is depicted in Fig. 5.8. Shown are the individual fit results for $\alpha_s(m_Z)$ and the mean result, which does not lie in between. This is a feature known from highly correlated observables. In fact it can be shown [58], that any correlated weighted average from two measurements does not lie between the individual measurements, if

$$\rho_{12} > \min\left(\frac{\sigma_1}{\sigma_2}, \frac{\sigma_2}{\sigma_1}\right). \tag{5.6}$$

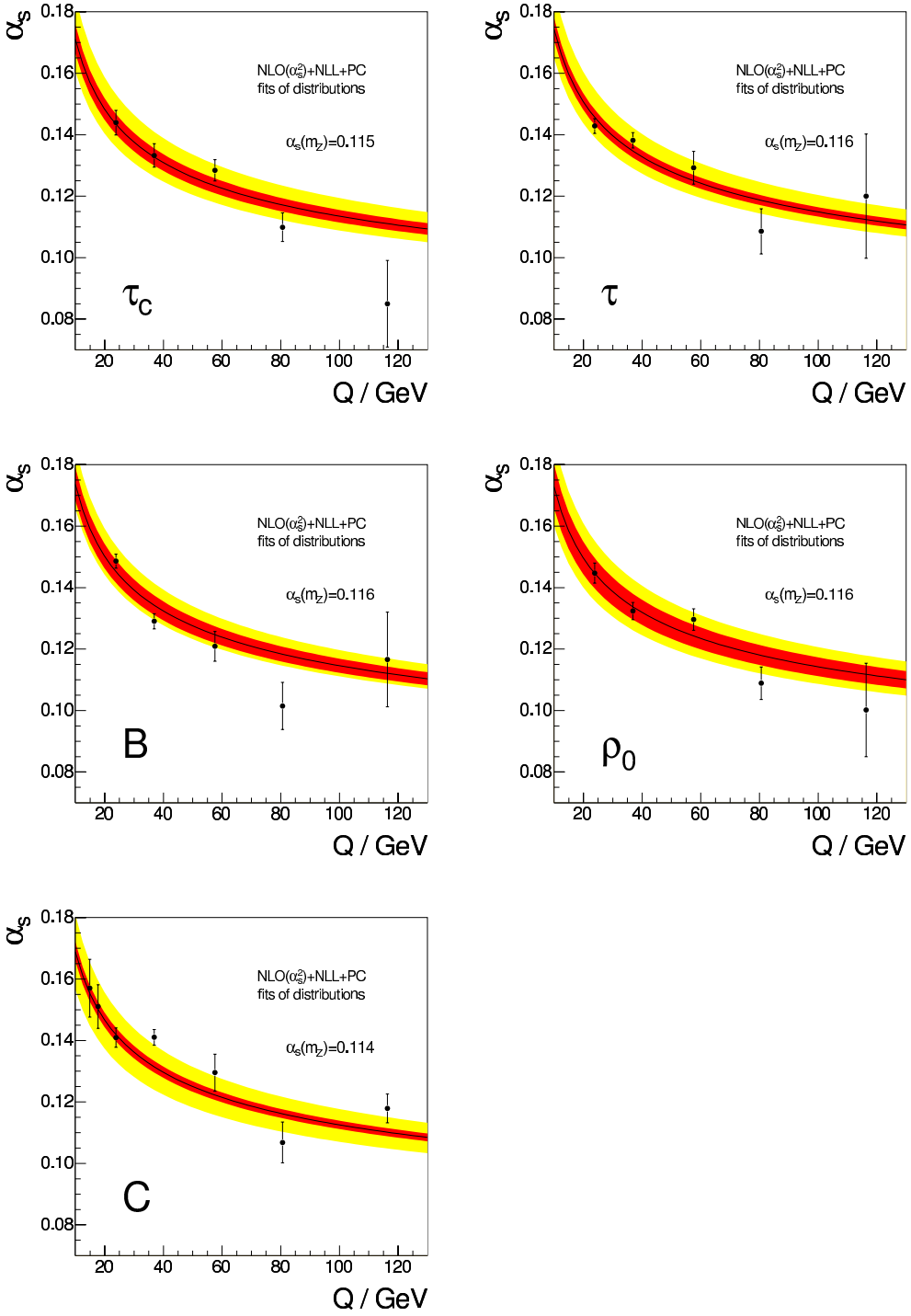

Figure 5.6: The running coupling $\alpha_s(Q)$ obtained from fits to the event shape variables at single values of Q. For each event shape, a common value of α_0 was fitted. The combined fit result is given as a band, the inner area denoting the experimental error, the outer area represents the total error.

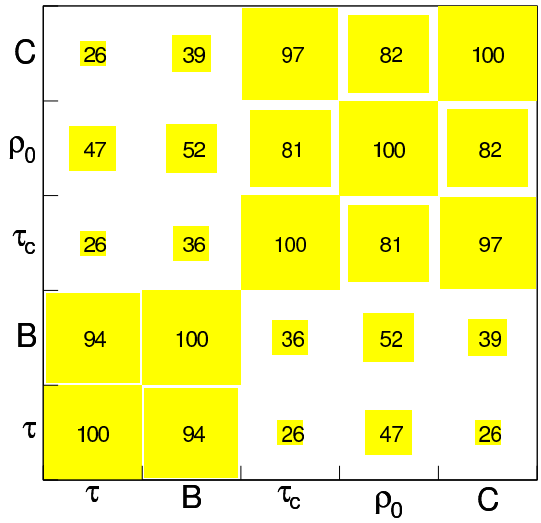

Figure 5.7: Correlation coefficients for pairs of event shape variables in per cent, determined with RAPGAP on hadron level.

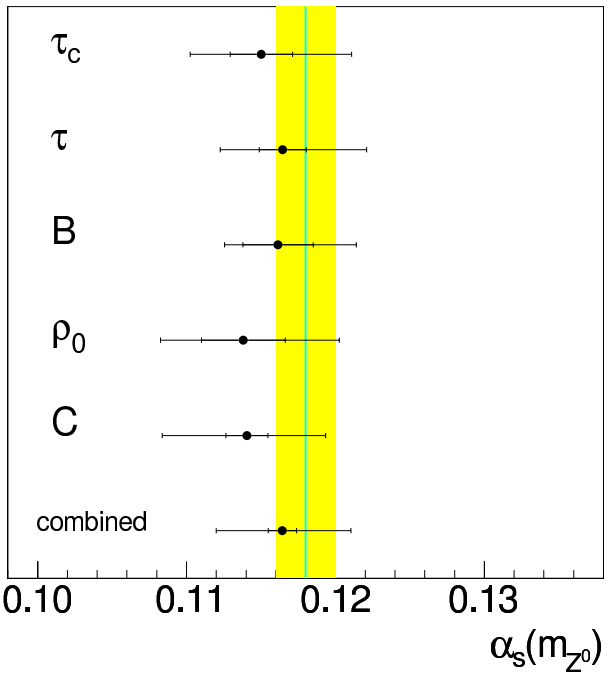

Figure 5.8: The fitted values of $\alpha_s(m_Z)$. The inner error bar denotes the experimental uncertainty. The total uncertainty is given by the outer error bar.

The presented average is affected by this, e.g. for thrust τ and jet broadening B: $0.94 > 0.0016/0.0024$. Because of this, one should not read too much in the combined result of Fig. 5.8.

5.4 Fits to Mean Values

The mean values which are presented in Fig. 4.21 are used for a fit as well. For this application it is not reasonable to use the resummed calculation, because of difficulties at high values of the event shape variable, which are related to subleading logarithms and the matching procedure [64]. These regions can be excluded from the fit of spectra, but are always present in the mean values.

Fig. 5.9 shows the event shape mean values as a function of the scale Q, together with the fitted prediction from DISASTER++.

Also shown is the calculation without power corrections. The size of the correction depends significantly on the observable, the variables with explicit reference to the virtual boson axis τ and B exhibit rather small hadronisation corrections.

Since the preceding mean value analysis by the H1 collaboration [14] employed DISENT for the fixed order calculation, this program was only used as an alternative for the present work. The results are compared in the upper left diagram of Fig. 5.10. The obtained values of α_s and α_0 are not consistent within experimental errors. Rather they appear to be shifted to lower values of α_s and α_0, while maintaining the relative alignment to each other. This is puzzling, because the data points in Fig. 4.21 are compatible within errors, hence there needs to be a discrepancy in the calculation, most probably in the application of the power corrections.

Another possibility is, that the different detector calibrations lead to a systematic shift of the mean values at all Q bins. Such a correlated shift could be compensated by the power correction, compare Fig. 5.9. Since in both analyses the Q bins are treated uncorrelated, it may be that the error of α_0 is underestimated, and in consequence the contours shown in Fig. 5.10 are too small.

No contours for τ and B can be given in the diagram, because both variables showed correlations between α_s and α_0 of more than 99%, rendering a stable fit impossible. However, if alternately one of the two fit parameters was fixed, reasonable results were obtained

High correlation for this variables were also found in [14], but to a lesser extend, probably because also data at lower values of Q had been included. Since the present analysis is optimised for the study of spectra, this low Q phase space is not considered here.

The upper right diagram of Fig. 5.10 shows the fit results obtained with DISASTER++, together with contours from the ZEUS collaboration. The difference between DISENT and DISASTER++ is larger compared to the difference seen with the spectra, which is expected. The contours for the ZEUS analysis had to be de-

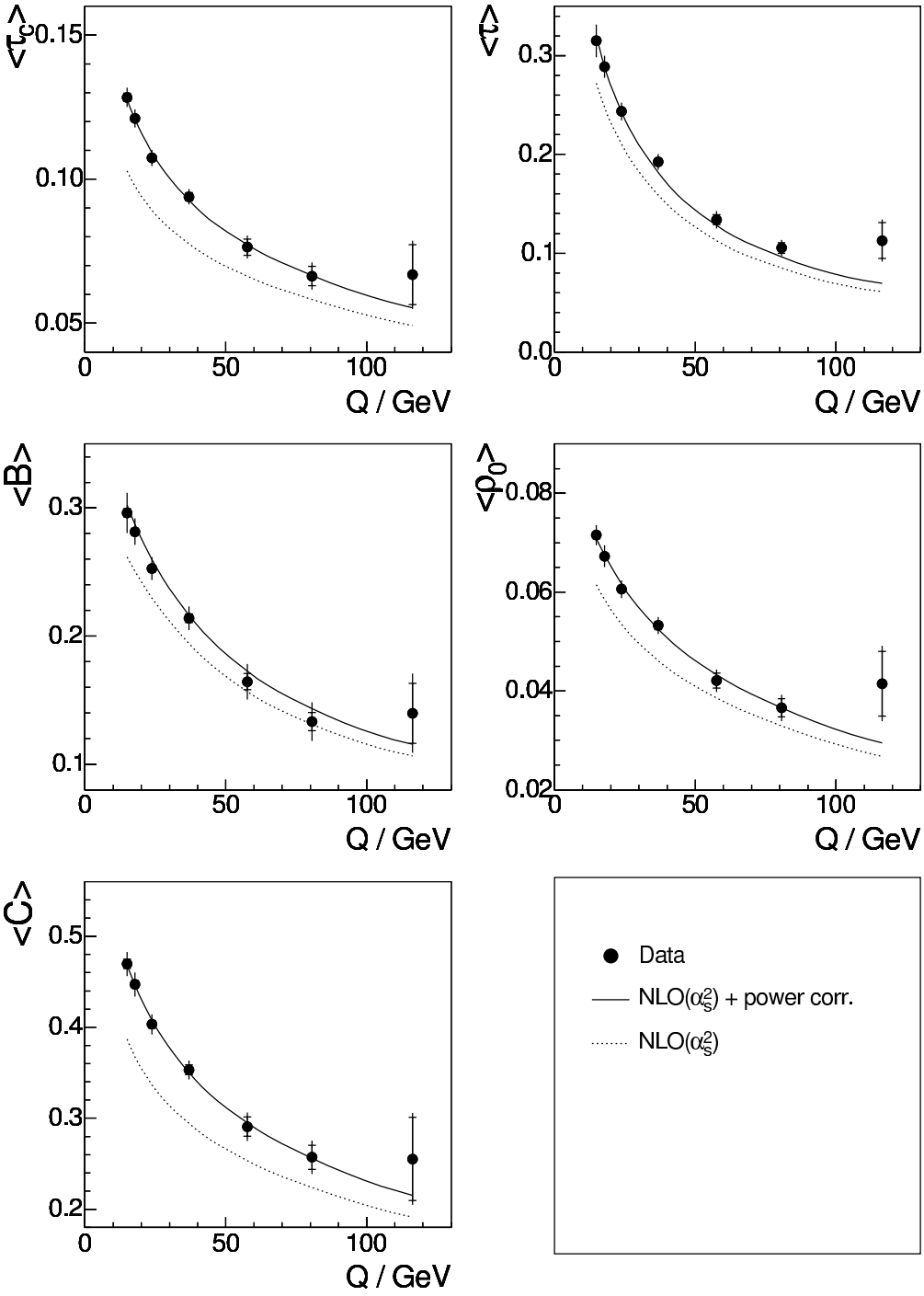

Figure 5.9: Mean values of the event shape variables against the scale Q. The inner error bars denote the statistical error, the outer error bars correspond to the statistical and the experimental systematical error, added in quadrature.

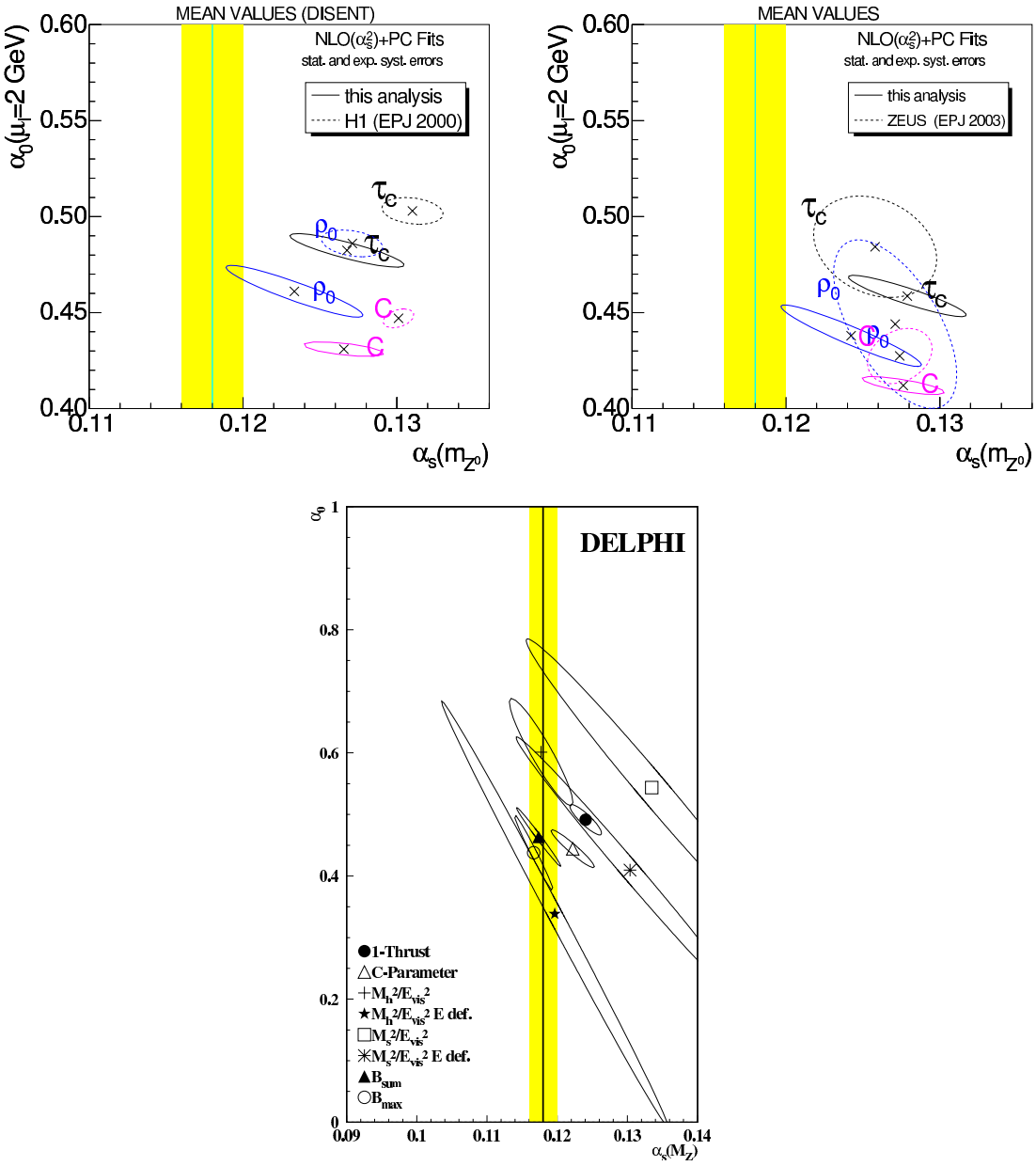

Figure 5.10: 1-σ contours in the (α_s, α_0) plane from fits to the event shape mean values. Comparison between the present analysis and analyses by the H1, ZEUS and DELPHI collaborations.

termined from numbers (central values, errors, and the correlation coefficient) given in a table in [66], since contours were only presented for the statistical error alone.

Consistency is found for the results of the presented analysis and the analysis from the ZEUS collaboration.

Fig. 5.10 presents on the lower plot results from the DELPHI collaboration, which include also data from several past e^+e^- experiments, e.g. at PETRA [28]. Again, the variables which may be compared are thrust $1-T$, C-parameter and jet mass $M_{sE}^2/E_{\text{vis}}^2$. Just as the spectra, the mean values exhibit roughly the same properties in e^+e^- annihilation and in DIS: the strong coupling constant being somewhat higher than the world mean, and α_0 between 0.4 and 0.5 in both cases.

5.5 Conclusion

Power correction fits to the spectra of 2-jet event shapes have been successfully performed in the context of this work. The average effective non-perturbative coupling α_0 is found to be 0.5 within 10%, being in good agreement with expectations from theorists side. The results are consistent with each other and with the world mean of α_s. This is an impotant achievement compared to fits of the mean values.

Spectra could be used for the QCD fits only because resummed calculations have become available, which compared to the fixed order terms alone extend the description to low values of event shapes, corresponding to pencil like configurations. More or less surprisingly, it is even possible to extend the fit interval down to the bin containing $F = 0$.

Together with recent results from the ZEUS and DELPHI[2] collaborations, a consistent picture of event shapes variables evolves. Power corrections have to be considered as an alternative for the description of hadronisation of event shapes variables, with respect to conventional hadronisation models.

With the theory calculations used in the work at hand, the dependence on the renormalisation scale has been reduced a lot: While for a variation of μ_r^2 by a factor of 4, a change of more than 10% for α_s was found in the former mean value analysis [57], this effect is now at the 5% level.

Still, this uncertainty due to missing higher orders is the largest single contribution to the total error. For a competitive α_s determination also more investigations of the various correlations are needed, both between the bins of Q and between the event shape variables. It should be possible to profit from similar ongoing endeavours of the LEP QCD working group [72].

Attempts to fit the spectra of jet rates after applying conventional hadronisation corrections remained fruitless. While the reason of this is not exactly clear, it is conspicuous that the NLO calculations produced now and then negative cross sections

[2]The LEP collaborations ALEPH, L3 and OPAL offer results as well, which are not discussed here for sake of brevity.

at low values of the jet rates. This is an evidence of bad convergence of the perturbative series in this region of phase space, which may be solved when resummed terms are included. Therefore the completion of the generalised resummation program, which is currently underway [23], is eagerly awaited for.

Also it would be interesting to have a reliable NLO calculation at hand, which includes electroweak contributions, as the Z^0 exchange. The statistical precision in the data of the high Q region is already good enough to study possible differences for e^+p and e^-p scattering.

Chapter 6

Summary and Outlook

In this thesis an analysis of event shape variables in DIS is presented. The data measurement is based on the whole H1 data set taken at HERA I from 1995 to 2000 and covers scales from 14 GeV to 200 GeV, divided in seven bins.

The present work extends former analyses [8, 14] of mean values to the whole differential distributions. Also new variables are included: out-of-event plane momentum, azimuthal correlation as well as the three- and four-jet rate, hence in total 679 data points have been determined. A refined experimental treatment of the hadronic final state and a better hadronic calibration result in an improved measurement.

Event samples at two center of mass energies and two lepton beam polarities are separately corrected for detector effects. Differences in the results between the e^+p and e^-p subsamples are observed, which could partly be canceled for the final result by building the cross section weighted averages. Correlations between the bins of the differential event shape distributions are generated by the limited detector resolution and experimental systematic uncertainties. These have been accounted for and are represented by the full covariance matrices. A strong dependence of the event shape distributions on the scale Q demonstrates their sensitivity to QCD.

It has been shown earlier [14] that power corrections are applicable in the description of the non-perturbative hadronisation of event shape mean values in DIS. In the present work this conclusion is extended to the spectra of event shapes in DIS. Resummed terms turn out to be indispensable for the description of the lower part of the spectra. If these contributions are included, large parts of the investigated phase space are well described, in particular for scales larger than 30 GeV.

Fits of the free parameters of these calculations, α_s and α_0, lead to consistent results, with a considerably reduced spread in the fitted value of $\alpha_s(m_Z)$ compared to the mean value analysis. The theoretical uncertainty makes up the largest contribution to the total uncertainty on the $\alpha_s(m_Z)$ determinations. The event shape variables which are defined with respect to the virtual boson axis (τ and B) are found to be highly correlated. This statement also holds for the remaining vari-

ables, which do not employ this axis. However, the correlation between these two classes of observables is only moderate. The results of the fit are in good agreement with findings in e^+e^- annihilation, represented here by an analysis of the DELPHI collaboration.

The results obtained in this thesis received the "preliminary" status by the H1 collaboration and are being prepared for publication.

In the future the present work could be extended in several ways: The completion of the generalised resummation program, which is currently underway [23], will allow a QCD analysis for the spectra of y_2, y_3, K_{out} and χ. Unfortunately there is no NLO calculation available yet which is suitable for event shapes variables and includes electro weak contributions.

The assesment of the theoretical errors could be refined, e.g. if the uncertainty band method, which was recently proposed [73], will be used.

In order to extract a common value of $\alpha_s(m_Z)$ from event shapes in DIS it is necessary to account for the correlations: both between the determinations at different values of Q as well as between the variables.

Appendix

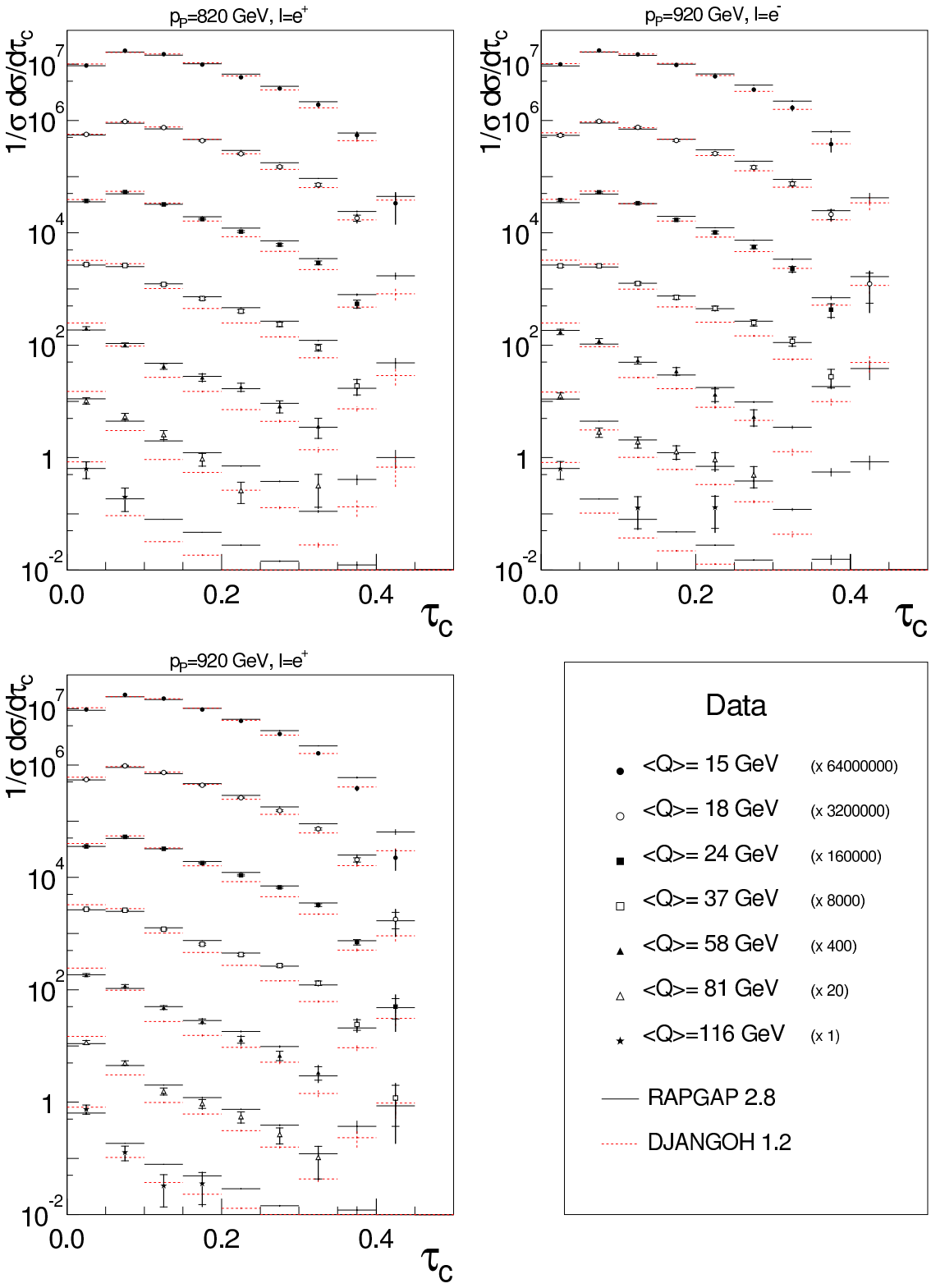

Figure 6.1: Measured distributions of thrust w.r.t. the thrust axis at the non-radiative hadron level for three data subsets.

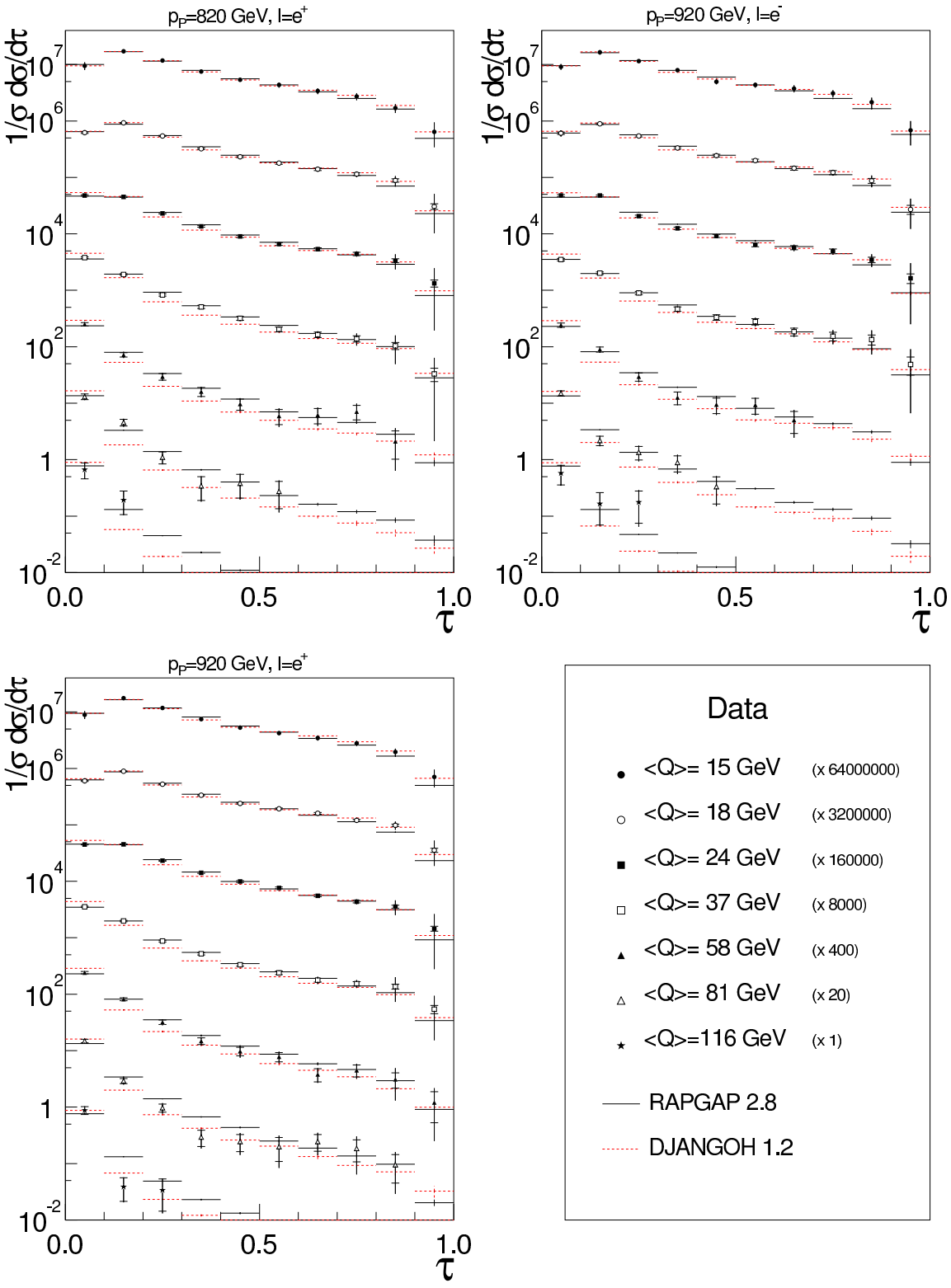

Figure 6.2: Measured distributions of thrust w.r.t. the virtual boson axis at the non-radiative hadron level for three data subsets.

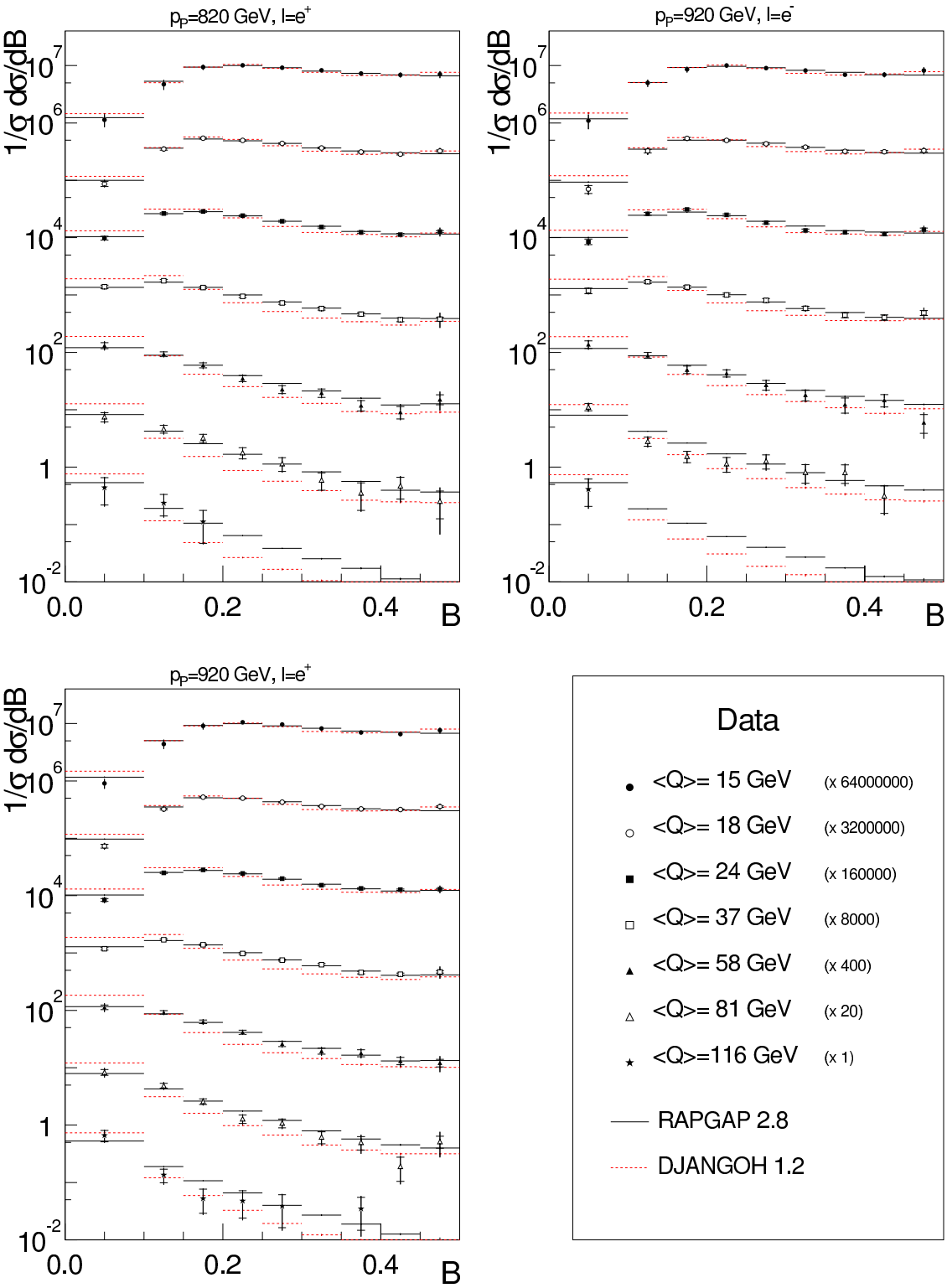

Figure 6.3: Measured distributions of jet broadining at the non-radiative hadron level for three data subsets.

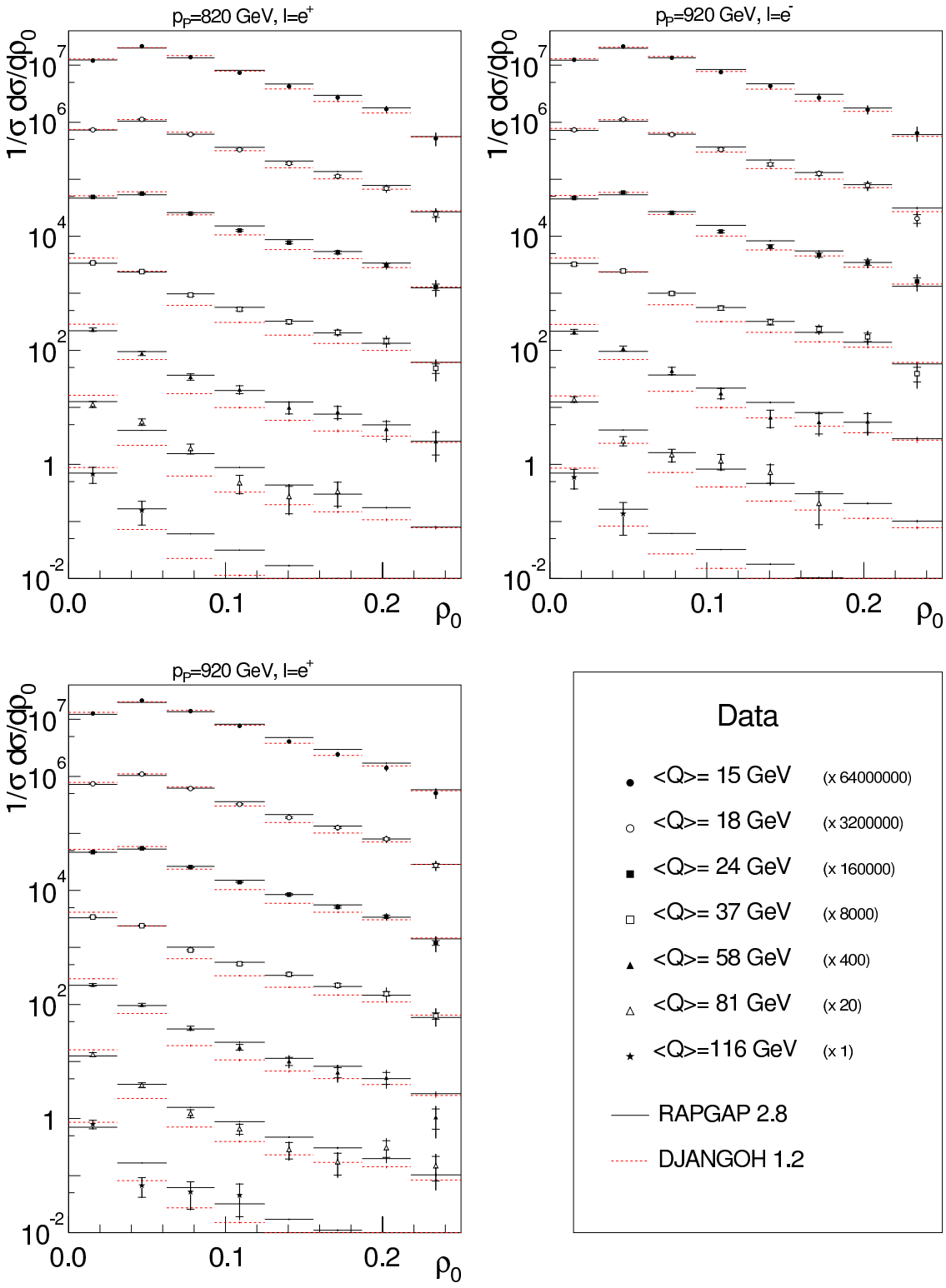

Figure 6.4: Measured distributions of the jet mass at the non-radiative hadron level for three data subsets.

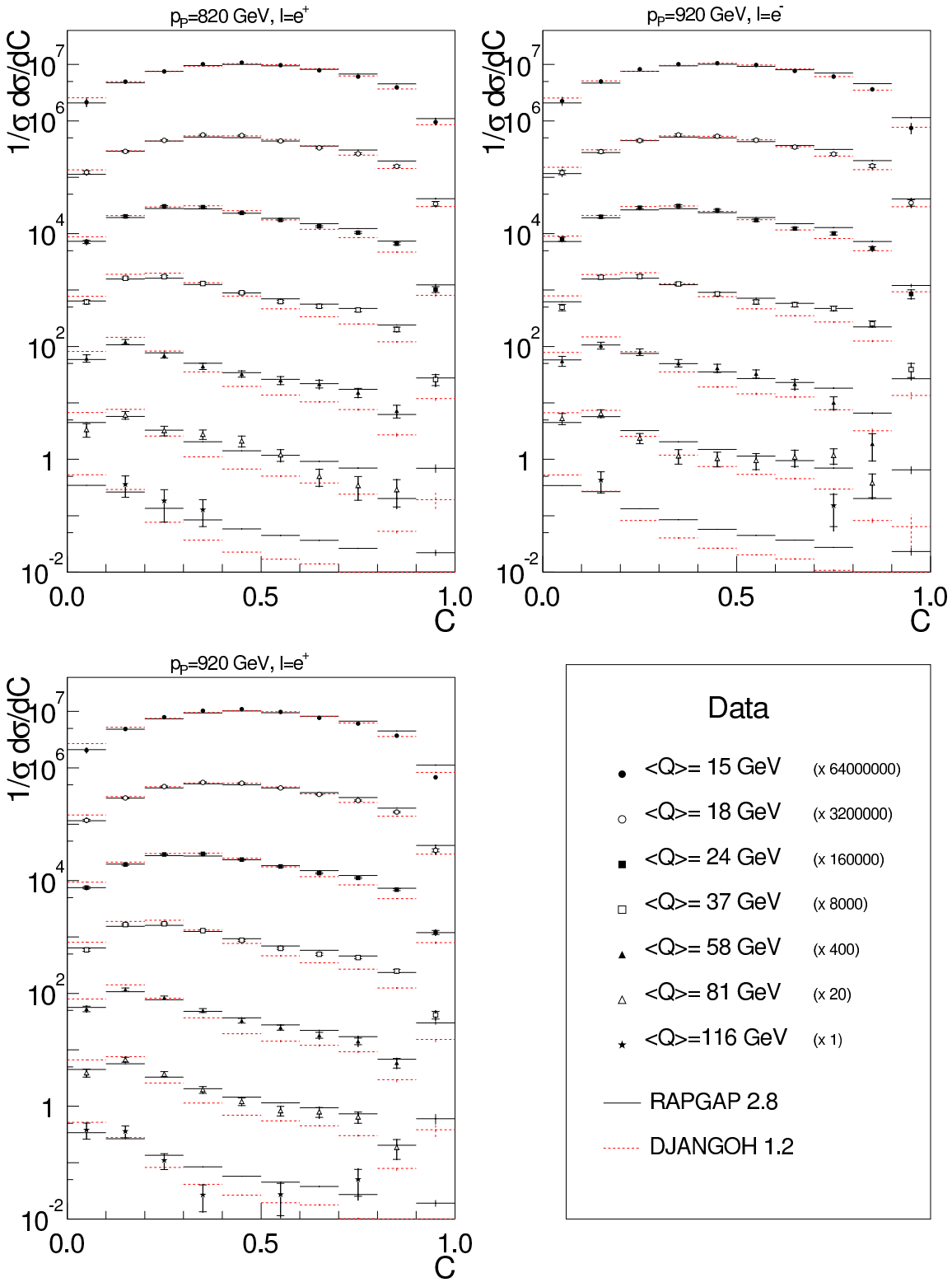

Figure 6.5: Measured distributions of the C-parameter at the non-radiative hadron level for three data subsets.

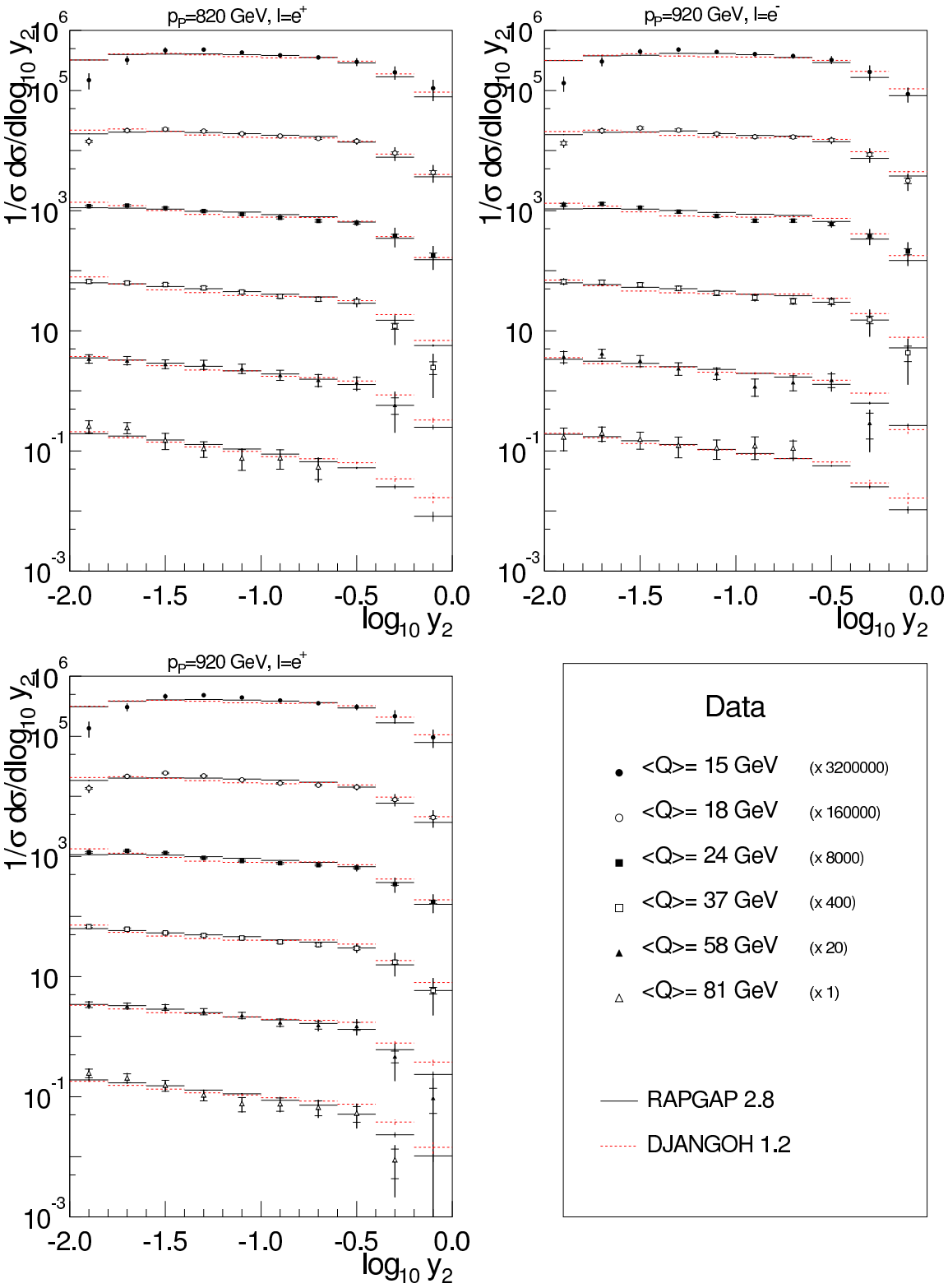

Figure 6.6: Measured distributions of the 2-jet rate at the non-radiative hadron level for three data subsets.

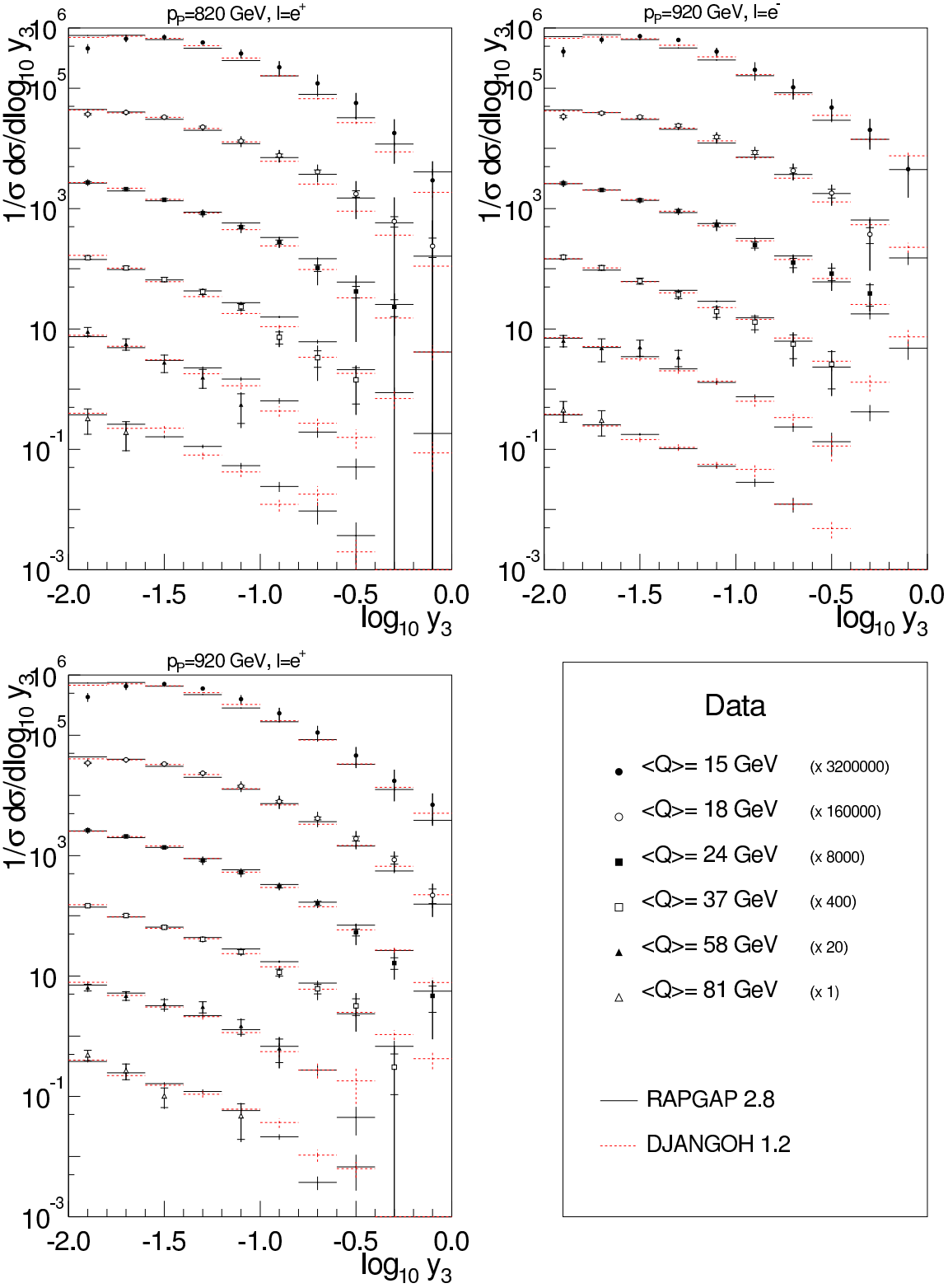

Figure 6.7: Measured distributions of the 3-jet rate at the non-radiative hadron level for three data subsets.

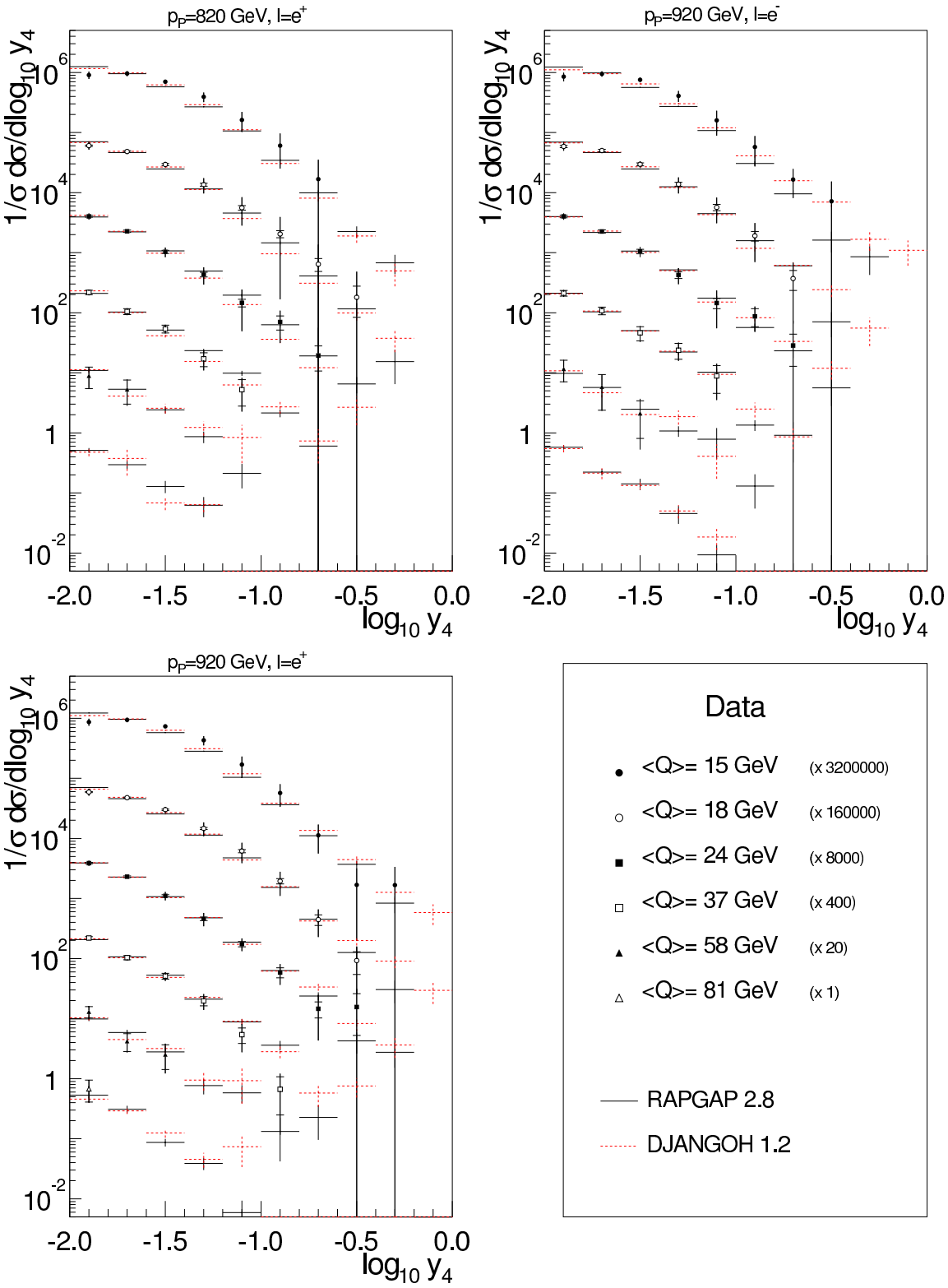

Figure 6.8: Measured distributions of the 4-jet rate at the non-radiative hadron level for three data subsets.

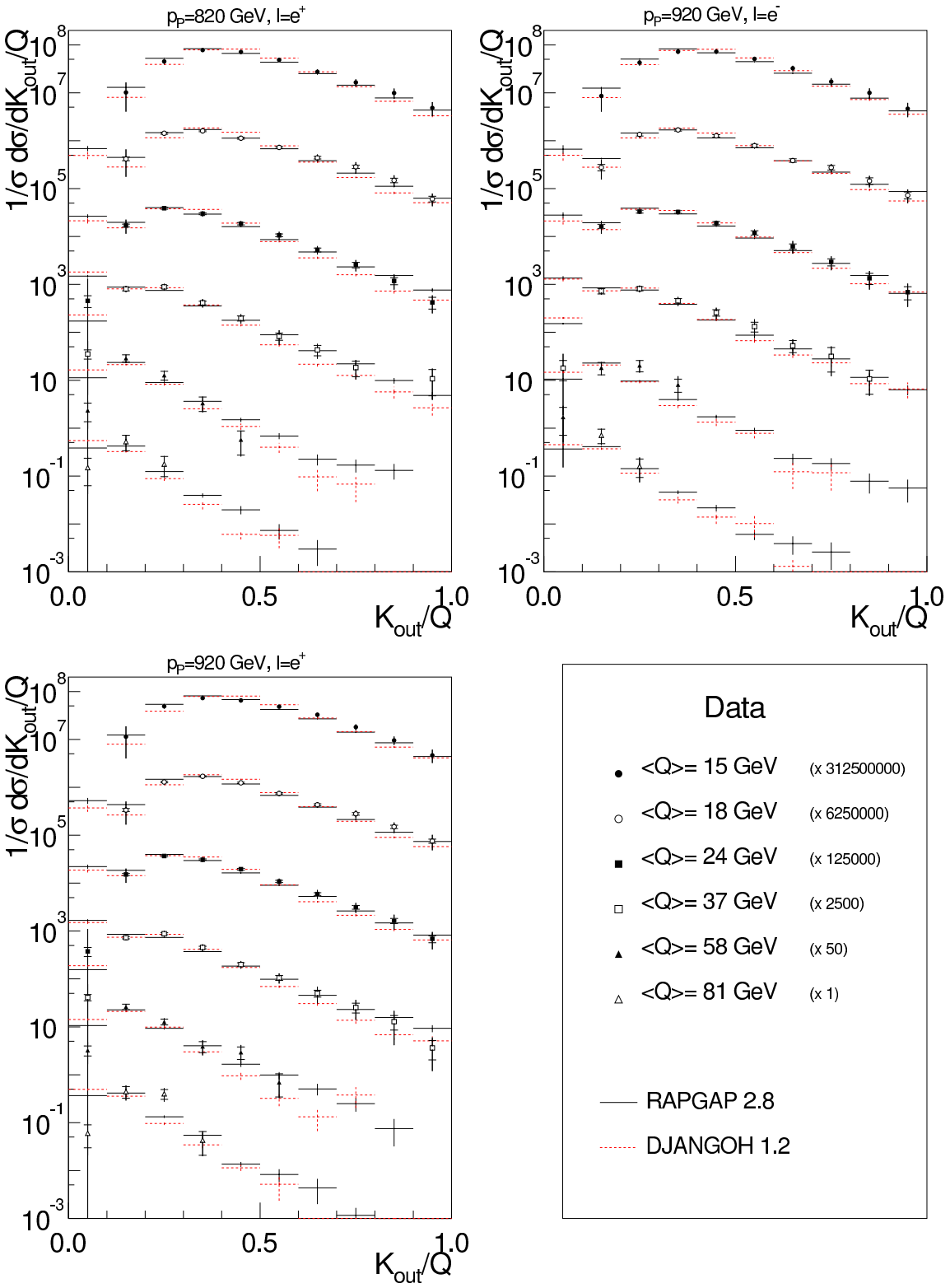

Figure 6.9: Measured distributions of the out-of-event plane momentum at the non-radiative hadron level for three data subsets.

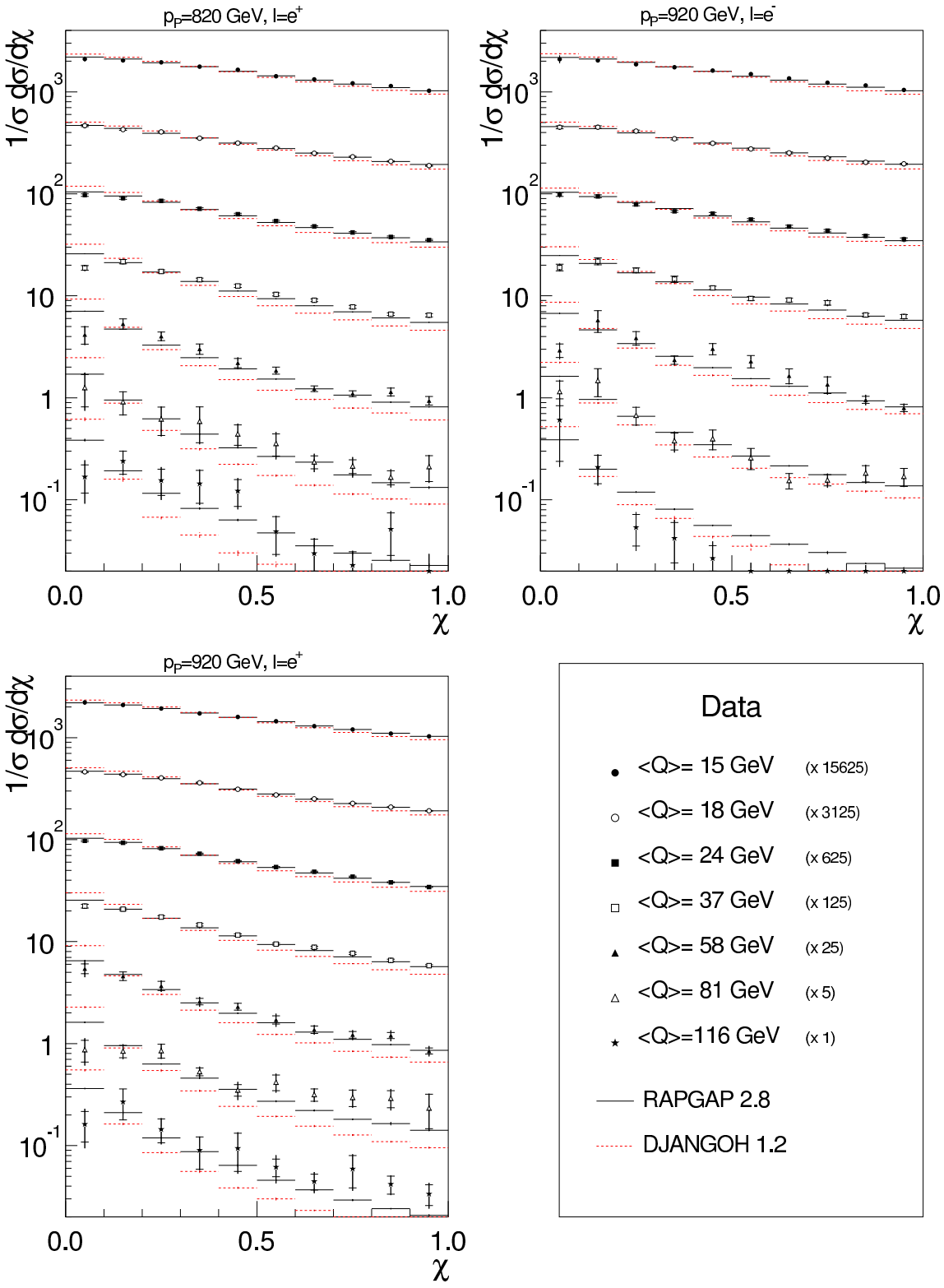

Figure 6.10: Measured distributions of the azimuthal correlation at the non-radiative hadron level for three data subsets.

$\langle Q \rangle$	$\tau_c \in [0.000, 0.050]$	$\tau_c \in [0.050, 0.100]$	$\tau_c \in [0.100, 0.150]$	$\tau_c \in [0.150, 0.200]$	$\tau_c \in [0.200, 0.250]$
14.926	$0.1514 \pm 0.0039 \pm 0.0046$	$0.2757 \pm 0.0054 \pm 0.0097$	$0.2385 \pm 0.0046 \pm 0.0037$	$0.1517 \pm 0.0034 \pm 0.0065$	$0.0955 \pm 0.0027 \pm 0.0038$
17.750	$0.1718 \pm 0.0038 \pm 0.0048$	$0.3029 \pm 0.0050 \pm 0.0095$	$0.2291 \pm 0.0040 \pm 0.0043$	$0.1367 \pm 0.0029 \pm 0.0056$	$0.0819 \pm 0.0021 \pm 0.0024$
23.816	$0.2223 \pm 0.0047 \pm 0.0066$	$0.3285 \pm 0.0055 \pm 0.0084$	$0.2019 \pm 0.0039 \pm 0.0041$	$0.1127 \pm 0.0028 \pm 0.0037$	$0.0683 \pm 0.0021 \pm 0.0029$
36.854	$0.3386 \pm 0.0091 \pm 0.0097$	$0.3254 \pm 0.0077 \pm 0.0144$	$0.1496 \pm 0.0045 \pm 0.0039$	$0.0806 \pm 0.0032 \pm 0.0039$	$0.0527 \pm 0.0026 \pm 0.0026$
57.580	$0.4598 \pm 0.0262 \pm 0.0227$	$0.2919 \pm 0.0168 \pm 0.0063$	$0.1210 \pm 0.0096 \pm 0.0088$	$0.0689 \pm 0.0066 \pm 0.0059$	$0.0324 \pm 0.0045 \pm 0.0050$
80.592	$0.5790 \pm 0.0473 \pm 0.0298$	$0.2486 \pm 0.0226 \pm 0.0121$	$0.0781 \pm 0.0110 \pm 0.0058$	$0.0472 \pm 0.0083 \pm 0.0062$	$0.0274 \pm 0.0061 \pm 0.0031$
116.337	$0.7481 \pm 0.1390 \pm 0.0515$	$0.1278 \pm 0.0369 \pm 0.0118$	$0.0325 \pm 0.0187 \pm 0.0037$	$0.0355 \pm 0.0205 \pm 0.0074$	$0.0323 \pm 0.0228 \pm 0.0084$

$\langle Q \rangle$	$\tau_c \in [0.250, 0.300]$	$\tau_c \in [0.300, 0.350]$	$\tau_c \in [0.350, 0.400]$	$\tau_c \in [0.400, 0.450]$	$\tau_c \in [0.450, 0.500]$
14.926	$0.0557 \pm 0.0019 \pm 0.0021$	$0.0252 \pm 0.0013 \pm 0.0011$	$0.0060 \pm 0.0006 \pm 0.0002$	$0.0003 \pm 0.0001 \pm 0.0001$	$0.0000 \pm 0.0000 \pm 0.0000$
17.750	$0.0480 \pm 0.0016 \pm 0.0024$	$0.0228 \pm 0.0011 \pm 0.0019$	$0.0064 \pm 0.0006 \pm 0.0010$	$0.0006 \pm 0.0002 \pm 0.0002$	$0.0000 \pm 0.0000 \pm 0.0000$
23.816	$0.0414 \pm 0.0016 \pm 0.0023$	$0.0201 \pm 0.0011 \pm 0.0015$	$0.0044 \pm 0.0005 \pm 0.0002$	$0.0003 \pm 0.0001 \pm 0.0002$	$0.0000 \pm 0.0000 \pm 0.0000$
36.854	$0.0336 \pm 0.0021 \pm 0.0017$	$0.0164 \pm 0.0015 \pm 0.0014$	$0.0030 \pm 0.0006 \pm 0.0006$	$0.0001 \pm 0.0001 \pm 0.0001$	$0.0000 \pm 0.0000 \pm 0.0000$
57.580	$0.0169 \pm 0.0032 \pm 0.0009$	$0.0084 \pm 0.0023 \pm 0.0018$	$0.0005 \pm 0.0006 \pm 0.0003$	$0.0000 \pm 0.0000 \pm 0.0000$	$0.0000 \pm 0.0000 \pm 0.0000$
80.592	$0.0132 \pm 0.0042 \pm 0.0013$	$0.0052 \pm 0.0030 \pm 0.0009$	$0.0013 \pm 0.0013 \pm 0.0004$	$0.0001 \pm 0.0001 \pm 0.0000$	$0.0000 \pm 0.0000 \pm 0.0000$
116.337	$0.0234 \pm 0.0166 \pm 0.0083$	$0.0005 \pm 0.0005 \pm 0.0003$	$0.0000 \pm 0.0000 \pm 0.0000$	$0.0000 \pm 0.0000 \pm 0.0000$	$0.0000 \pm 0.0000 \pm 0.0000$

Table 6.1: Normalised differential cross section for τ_c.

$\langle Q \rangle$	$\tau \in [0.000, 0.100]$	$\tau \in [0.100, 0.200]$	$\tau \in [0.200, 0.300]$	$\tau \in [0.300, 0.400]$	$\tau \in [0.400, 0.500]$
14.926	$0.1394 \pm 0.0044 \pm 0.0213$	$0.2736 \pm 0.0052 \pm 0.0165$	$0.1835 \pm 0.0038 \pm 0.0036$	$0.1164 \pm 0.0030 \pm 0.0063$	$0.0823 \pm 0.0024 \pm 0.0056$
17.750	$0.1885 \pm 0.0044 \pm 0.0153$	$0.2783 \pm 0.0045 \pm 0.0073$	$0.1639 \pm 0.0032 \pm 0.0037$	$0.1047 \pm 0.0025 \pm 0.0034$	$0.0749 \pm 0.0021 \pm 0.0047$
23.816	$0.2810 \pm 0.0057 \pm 0.0160$	$0.2825 \pm 0.0047 \pm 0.0058$	$0.1449 \pm 0.0032 \pm 0.0019$	$0.0886 \pm 0.0025 \pm 0.0023$	$0.0619 \pm 0.0021 \pm 0.0026$
36.854	$0.4421 \pm 0.0105 \pm 0.0192$	$0.2470 \pm 0.0061 \pm 0.0091$	$0.1093 \pm 0.0038 \pm 0.0035$	$0.0648 \pm 0.0030 \pm 0.0026$	$0.0415 \pm 0.0023 \pm 0.0018$
57.580	$0.6032 \pm 0.0298 \pm 0.0283$	$0.2044 \pm 0.0124 \pm 0.0109$	$0.0799 \pm 0.0073 \pm 0.0058$	$0.0370 \pm 0.0050 \pm 0.0038$	$0.0244 \pm 0.0041 \pm 0.0038$
80.592	$0.7426 \pm 0.0508 \pm 0.0387$	$0.1452 \pm 0.0149 \pm 0.0133$	$0.0486 \pm 0.0079 \pm 0.0067$	$0.0147 \pm 0.0047 \pm 0.0028$	$0.0122 \pm 0.0041 \pm 0.0030$
116.337	$0.8782 \pm 0.1407 \pm 0.0385$	$0.0387 \pm 0.0173 \pm 0.0056$	$0.0339 \pm 0.0196 \pm 0.0069$	$0.0298 \pm 0.0211 \pm 0.0090$	$0.0190 \pm 0.0135 \pm 0.0072$
$\langle Q \rangle$	$\tau \in [0.500, 0.600]$	$\tau \in [0.600, 0.700]$	$\tau \in [0.700, 0.800]$	$\tau \in [0.800, 0.900]$	$\tau \in [0.900, 1.000]$
14.926	$0.0657 \pm 0.0022 \pm 0.0036$	$0.0542 \pm 0.0021 \pm 0.0052$	$0.0436 \pm 0.0019 \pm 0.0041$	$0.0305 \pm 0.0017 \pm 0.0043$	$0.0110 \pm 0.0010 \pm 0.0037$
17.750	$0.0604 \pm 0.0019 \pm 0.0025$	$0.0501 \pm 0.0018 \pm 0.0028$	$0.0375 \pm 0.0016 \pm 0.0030$	$0.0307 \pm 0.0015 \pm 0.0049$	$0.0111 \pm 0.0009 \pm 0.0052$
23.816	$0.0479 \pm 0.0019 \pm 0.0020$	$0.0347 \pm 0.0016 \pm 0.0011$	$0.0273 \pm 0.0014 \pm 0.0023$	$0.0223 \pm 0.0014 \pm 0.0063$	$0.0091 \pm 0.0009 \pm 0.0073$
36.854	$0.0300 \pm 0.0021 \pm 0.0017$	$0.0222 \pm 0.0017 \pm 0.0028$	$0.0192 \pm 0.0017 \pm 0.0025$	$0.0171 \pm 0.0017 \pm 0.0077$	$0.0068 \pm 0.0011 \pm 0.0047$
57.580	$0.0195 \pm 0.0036 \pm 0.0030$	$0.0095 \pm 0.0025 \pm 0.0012$	$0.0113 \pm 0.0027 \pm 0.0020$	$0.0078 \pm 0.0024 \pm 0.0038$	$0.0030 \pm 0.0017 \pm 0.0017$
80.592	$0.0100 \pm 0.0045 \pm 0.0036$	$0.0123 \pm 0.0040 \pm 0.0034$	$0.0092 \pm 0.0039 \pm 0.0046$	$0.0047 \pm 0.0025 \pm 0.0022$	$0.0004 \pm 0.0004 \pm 0.0003$
116.337	$0.0004 \pm 0.0004 \pm 0.0002$	$0.0000 \pm 0.0000 \pm 0.0000$	$0.0000 \pm 0.0000 \pm 0.0000$	$0.0000 \pm 0.0000 \pm 0.0000$	$0.0000 \pm 0.0000 \pm 0.0000$

Table 6.2: Normalised differential cross section for τ.

$\langle Q \rangle$	$B \in [0.000, 0.100]$	$B \in [0.100, 0.150]$	$B \in [0.150, 0.200]$	$B \in [0.200, 0.250]$	$B \in [0.250, 0.300]$
14.926	$0.0141 \pm 0.0016 \pm 0.0023$	$0.0689 \pm 0.0032 \pm 0.0123$	$0.1418 \pm 0.0041 \pm 0.0180$	$0.1646 \pm 0.0039 \pm 0.0054$	$0.1504 \pm 0.0034 \pm 0.0032$
17.750	$0.0229 \pm 0.0018 \pm 0.0025$	$0.1008 \pm 0.0035 \pm 0.0091$	$0.1625 \pm 0.0037 \pm 0.0079$	$0.1561 \pm 0.0032 \pm 0.0024$	$0.1329 \pm 0.0029 \pm 0.0024$
23.816	$0.0527 \pm 0.0030 \pm 0.0057$	$0.1564 \pm 0.0043 \pm 0.0093$	$0.1755 \pm 0.0039 \pm 0.0047$	$0.1529 \pm 0.0034 \pm 0.0032$	$0.1238 \pm 0.0030 \pm 0.0027$
36.854	$0.1486 \pm 0.0077 \pm 0.0079$	$0.2135 \pm 0.0069 \pm 0.0097$	$0.1746 \pm 0.0053 \pm 0.0067$	$0.1221 \pm 0.0041 \pm 0.0040$	$0.0940 \pm 0.0037 \pm 0.0043$
57.580	$0.2836 \pm 0.0253 \pm 0.0424$	$0.2306 \pm 0.0159 \pm 0.0175$	$0.1584 \pm 0.0116 \pm 0.0138$	$0.1042 \pm 0.0087 \pm 0.0057$	$0.0654 \pm 0.0070 \pm 0.0058$
80.592	$0.4177 \pm 0.0494 \pm 0.0634$	$0.2440 \pm 0.0232 \pm 0.0317$	$0.1287 \pm 0.0142 \pm 0.0121$	$0.0641 \pm 0.0107 \pm 0.0077$	$0.0542 \pm 0.0094 \pm 0.0064$
116.337	$0.6613 \pm 0.1479 \pm 0.0820$	$0.1349 \pm 0.0361 \pm 0.0250$	$0.0527 \pm 0.0236 \pm 0.0100$	$0.0479 \pm 0.0240 \pm 0.0099$	$0.0387 \pm 0.0224 \pm 0.0095$

$\langle Q \rangle$	$B \in [0.300, 0.350]$	$B \in [0.350, 0.400]$	$B \in [0.400, 0.450]$	$B \in [0.450, 0.500]$	
14.926	$0.1283 \pm 0.0031 \pm 0.0064$	$0.1095 \pm 0.0029 \pm 0.0069$	$0.1027 \pm 0.0028 \pm 0.0075$	$0.1197 \pm 0.0033 \pm 0.0127$	
17.750	$0.1130 \pm 0.0026 \pm 0.0045$	$0.1014 \pm 0.0025 \pm 0.0050$	$0.0990 \pm 0.0025 \pm 0.0032$	$0.1114 \pm 0.0029 \pm 0.0120$	
23.816	$0.0951 \pm 0.0026 \pm 0.0037$	$0.0833 \pm 0.0025 \pm 0.0020$	$0.0794 \pm 0.0024 \pm 0.0032$	$0.0810 \pm 0.0025 \pm 0.0119$	
36.854	$0.0784 \pm 0.0034 \pm 0.0034$	$0.0570 \pm 0.0028 \pm 0.0027$	$0.0530 \pm 0.0028 \pm 0.0024$	$0.0587 \pm 0.0030 \pm 0.0137$	
57.580	$0.0490 \pm 0.0058 \pm 0.0061$	$0.0453 \pm 0.0063 \pm 0.0062$	$0.0331 \pm 0.0049 \pm 0.0051$	$0.0305 \pm 0.0047 \pm 0.0082$	
80.592	$0.0309 \pm 0.0074 \pm 0.0047$	$0.0250 \pm 0.0066 \pm 0.0065$	$0.0096 \pm 0.0043 \pm 0.0023$	$0.0259 \pm 0.0061 \pm 0.0105$	
116.337	$0.0293 \pm 0.0207 \pm 0.0082$	$0.0349 \pm 0.0202 \pm 0.0121$	$0.0003 \pm 0.0003 \pm 0.0001$	$0.0000 \pm 0.0000 \pm 0.0000$	

Table 6.3: Normalised differential cross section for B.

$\langle Q \rangle$	$\rho_0 \in [0.000, 0.031]$	$\rho_0 \in [0.031, 0.062]$	$\rho_0 \in [0.062, 0.093]$	$\rho_0 \in [0.093, 0.125]$	$\rho_0 \in [0.125, 0.156]$
14.926	$0.1973 \pm 0.0046 \pm 0.0102$	$0.3337 \pm 0.0058 \pm 0.0112$	$0.2168 \pm 0.0043 \pm 0.0086$	$0.1206 \pm 0.0029 \pm 0.0039$	$0.0637 \pm 0.0021 \pm 0.0039$
17.750	$0.2310 \pm 0.0045 \pm 0.0117$	$0.3440 \pm 0.0052 \pm 0.0062$	$0.1912 \pm 0.0035 \pm 0.0077$	$0.1013 \pm 0.0024 \pm 0.0029$	$0.0594 \pm 0.0018 \pm 0.0030$
23.816	$0.2947 \pm 0.0055 \pm 0.0121$	$0.3432 \pm 0.0054 \pm 0.0098$	$0.1599 \pm 0.0034 \pm 0.0027$	$0.0879 \pm 0.0024 \pm 0.0033$	$0.0530 \pm 0.0019 \pm 0.0046$
36.854	$0.4264 \pm 0.0101 \pm 0.0136$	$0.3002 \pm 0.0070 \pm 0.0068$	$0.1122 \pm 0.0038 \pm 0.0026$	$0.0647 \pm 0.0029 \pm 0.0033$	$0.0423 \pm 0.0024 \pm 0.0039$
57.580	$0.5553 \pm 0.0281 \pm 0.0236$	$0.2466 \pm 0.0145 \pm 0.0086$	$0.0960 \pm 0.0083 \pm 0.0058$	$0.0447 \pm 0.0053 \pm 0.0040$	$0.0255 \pm 0.0042 \pm 0.0049$
80.592	$0.6667 \pm 0.0488 \pm 0.0326$	$0.1928 \pm 0.0187 \pm 0.0077$	$0.0616 \pm 0.0097 \pm 0.0056$	$0.0330 \pm 0.0067 \pm 0.0048$	$0.0144 \pm 0.0046 \pm 0.0025$
116.337	$0.7973 \pm 0.1368 \pm 0.0487$	$0.0668 \pm 0.0253 \pm 0.0054$	$0.0516 \pm 0.0258 \pm 0.0079$	$0.0450 \pm 0.0260 \pm 0.0111$	$0.0289 \pm 0.0205 \pm 0.0092$

$\langle Q \rangle$	$\rho_0 \in [0.156, 0.187]$	$\rho_0 \in [0.187, 0.218]$	$\rho_0 \in [0.218, 0.250]$		
14.926	$0.0380 \pm 0.0016 \pm 0.0035$	$0.0220 \pm 0.0012 \pm 0.0027$	$0.0079 \pm 0.0008 \pm 0.0014$		
17.750	$0.0395 \pm 0.0015 \pm 0.0042$	$0.0249 \pm 0.0012 \pm 0.0035$	$0.0086 \pm 0.0007 \pm 0.0016$		
23.816	$0.0321 \pm 0.0014 \pm 0.0029$	$0.0218 \pm 0.0012 \pm 0.0029$	$0.0075 \pm 0.0007 \pm 0.0022$		
36.854	$0.0270 \pm 0.0019 \pm 0.0029$	$0.0193 \pm 0.0016 \pm 0.0051$	$0.0079 \pm 0.0010 \pm 0.0026$		
57.580	$0.0163 \pm 0.0033 \pm 0.0045$	$0.0130 \pm 0.0031 \pm 0.0036$	$0.0026 \pm 0.0010 \pm 0.0011$		
80.592	$0.0087 \pm 0.0036 \pm 0.0020$	$0.0154 \pm 0.0050 \pm 0.0051$	$0.0074 \pm 0.0034 \pm 0.0032$		
116.337	$0.0101 \pm 0.0101 \pm 0.0043$	$0.0002 \pm 0.0002 \pm 0.0001$	$0.0000 \pm 0.0000 \pm 0.0000$		

Table 6.4: Normalised differential cross section for ρ_0.

$\langle Q \rangle$	$C \in [0.000, 0.100]$	$C \in [0.100, 0.200]$	$C \in [0.200, 0.300]$	$C \in [0.300, 0.400]$	$C \in [0.400, 0.500]$
14.926	$0.0320 \pm 0.0017 \pm 0.0034$	$0.0763 \pm 0.0028 \pm 0.0036$	$0.1232 \pm 0.0036 \pm 0.0073$	$0.1598 \pm 0.0041 \pm 0.0056$	$0.1718 \pm 0.0040 \pm 0.0033$
17.750	$0.0367 \pm 0.0016 \pm 0.0033$	$0.0916 \pm 0.0028 \pm 0.0046$	$0.1458 \pm 0.0036 \pm 0.0080$	$0.1725 \pm 0.0037 \pm 0.0058$	$0.1667 \pm 0.0035 \pm 0.0030$
23.816	$0.0467 \pm 0.0021 \pm 0.0042$	$0.1203 \pm 0.0035 \pm 0.0042$	$0.1819 \pm 0.0042 \pm 0.0071$	$0.1860 \pm 0.0041 \pm 0.0053$	$0.1476 \pm 0.0034 \pm 0.0038$
36.854	$0.0740 \pm 0.0041 \pm 0.0040$	$0.2079 \pm 0.0072 \pm 0.0090$	$0.2148 \pm 0.0067 \pm 0.0091$	$0.1628 \pm 0.0053 \pm 0.0060$	$0.1093 \pm 0.0039 \pm 0.0018$
57.580	$0.1336 \pm 0.0148 \pm 0.0117$	$0.2921 \pm 0.0204 \pm 0.0127$	$0.2087 \pm 0.0154 \pm 0.0063$	$0.1247 \pm 0.0101 \pm 0.0052$	$0.0823 \pm 0.0077 \pm 0.0042$
80.592	$0.1964 \pm 0.0324 \pm 0.0110$	$0.3349 \pm 0.0341 \pm 0.0244$	$0.1856 \pm 0.0202 \pm 0.0093$	$0.0981 \pm 0.0139 \pm 0.0050$	$0.0609 \pm 0.0095 \pm 0.0040$
116.337	$0.3815 \pm 0.1207 \pm 0.0321$	$0.3598 \pm 0.0849 \pm 0.0212$	$0.1098 \pm 0.0347 \pm 0.0092$	$0.0269 \pm 0.0134 \pm 0.0035$	$0.0181 \pm 0.0181 \pm 0.0022$
$\langle Q \rangle$	$C \in [0.500, 0.600]$	$C \in [0.600, 0.700]$	$C \in [0.700, 0.800]$	$C \in [0.800, 0.900]$	$C \in [0.900, 1.000]$
14.926	$0.1527 \pm 0.0036 \pm 0.0042$	$0.1202 \pm 0.0030 \pm 0.0060$	$0.0954 \pm 0.0026 \pm 0.0031$	$0.0580 \pm 0.0019 \pm 0.0031$	$0.0106 \pm 0.0008 \pm 0.0005$
17.750	$0.1371 \pm 0.0030 \pm 0.0044$	$0.1052 \pm 0.0025 \pm 0.0043$	$0.0822 \pm 0.0021 \pm 0.0031$	$0.0514 \pm 0.0016 \pm 0.0034$	$0.0108 \pm 0.0007 \pm 0.0016$
23.816	$0.1117 \pm 0.0028 \pm 0.0024$	$0.0848 \pm 0.0023 \pm 0.0030$	$0.0700 \pm 0.0021 \pm 0.0033$	$0.0434 \pm 0.0017 \pm 0.0028$	$0.0075 \pm 0.0006 \pm 0.0008$
36.854	$0.0787 \pm 0.0032 \pm 0.0046$	$0.0620 \pm 0.0028 \pm 0.0028$	$0.0543 \pm 0.0026 \pm 0.0024$	$0.0312 \pm 0.0020 \pm 0.0016$	$0.0052 \pm 0.0008 \pm 0.0008$
57.580	$0.0623 \pm 0.0065 \pm 0.0045$	$0.0454 \pm 0.0054 \pm 0.0057$	$0.0356 \pm 0.0049 \pm 0.0055$	$0.0147 \pm 0.0029 \pm 0.0017$	$0.0005 \pm 0.0004 \pm 0.0003$
80.592	$0.0417 \pm 0.0081 \pm 0.0039$	$0.0396 \pm 0.0079 \pm 0.0061$	$0.0322 \pm 0.0071 \pm 0.0034$	$0.0093 \pm 0.0036 \pm 0.0012$	$0.0013 \pm 0.0014 \pm 0.0003$
116.337	$0.0272 \pm 0.0157 \pm 0.0060$	$0.0257 \pm 0.0257 \pm 0.0044$	$0.0506 \pm 0.0253 \pm 0.0147$	$0.0004 \pm 0.0004 \pm 0.0001$	$0.0000 \pm 0.0000 \pm 0.0000$

Table 6.5: Normalised differential cross section for C.

$\langle Q \rangle$	$\log_{10} y_2 \in [-2.000, -1.800]$	$\log_{10} y_2 \in [-1.800, -1.600]$	$\log_{10} y_2 \in [-1.600, -1.400]$	$\log_{10} y_2 \in [-1.400, -1.200]$	$\log_{10} y_2 \in [-1.200, -1.000]$
14.926	$0.0398 \pm 0.0015 \pm 0.0107$	$0.0898 \pm 0.0027 \pm 0.0116$	$0.1355 \pm 0.0036 \pm 0.0125$	$0.1423 \pm 0.0036 \pm 0.0077$	$0.1298 \pm 0.0034 \pm 0.0082$
17.750	$0.0778 \pm 0.0023 \pm 0.0102$	$0.1234 \pm 0.0031 \pm 0.0106$	$0.1396 \pm 0.0033 \pm 0.0114$	$0.1251 \pm 0.0030 \pm 0.0099$	$0.1079 \pm 0.0027 \pm 0.0094$
23.816	$0.1218 \pm 0.0033 \pm 0.0152$	$0.1288 \pm 0.0034 \pm 0.0152$	$0.1186 \pm 0.0032 \pm 0.0143$	$0.0983 \pm 0.0027 \pm 0.0120$	$0.0873 \pm 0.0025 \pm 0.0107$
36.854	$0.1181 \pm 0.0047 \pm 0.0226$	$0.1069 \pm 0.0045 \pm 0.0206$	$0.0924 \pm 0.0041 \pm 0.0186$	$0.0843 \pm 0.0038 \pm 0.0151$	$0.0761 \pm 0.0035 \pm 0.0130$
57.580	$0.0991 \pm 0.0106 \pm 0.0305$	$0.0947 \pm 0.0105 \pm 0.0295$	$0.0893 \pm 0.0098 \pm 0.0328$	$0.0759 \pm 0.0091 \pm 0.0207$	$0.0659 \pm 0.0081 \pm 0.0172$
80.592	$0.1140 \pm 0.0187 \pm 0.0407$	$0.0948 \pm 0.0158 \pm 0.0352$	$0.0716 \pm 0.0148 \pm 0.0207$	$0.0491 \pm 0.0098 \pm 0.0153$	$0.0352 \pm 0.0095 \pm 0.0104$
116.337	$0.0593 \pm 0.0343 \pm 0.0157$	$0.0400 \pm 0.0283 \pm 0.0121$	$0.0464 \pm 0.0328 \pm 0.0149$	$0.0563 \pm 0.0325 \pm 0.0133$	$0.0258 \pm 0.0258 \pm 0.0048$
$\langle Q \rangle$	$\log_{10} y_2 \in [-1.000, -0.800]$	$\log_{10} y_2 \in [-0.800, -0.600]$	$\log_{10} y_2 \in [-0.600, -0.400]$	$\log_{10} y_2 \in [-0.400, -0.200]$	$\log_{10} y_2 \in [-0.200, 0.000]$
14.926	$0.1157 \pm 0.0031 \pm 0.0102$	$0.1043 \pm 0.0028 \pm 0.0104$	$0.0902 \pm 0.0027 \pm 0.0141$	$0.0638 \pm 0.0023 \pm 0.0193$	$0.0283 \pm 0.0015 \pm 0.0100$
17.750	$0.0946 \pm 0.0024 \pm 0.0094$	$0.0882 \pm 0.0023 \pm 0.0106$	$0.0816 \pm 0.0023 \pm 0.0161$	$0.0505 \pm 0.0018 \pm 0.0159$	$0.0255 \pm 0.0013 \pm 0.0096$
23.816	$0.0804 \pm 0.0024 \pm 0.0088$	$0.0749 \pm 0.0023 \pm 0.0104$	$0.0674 \pm 0.0023 \pm 0.0183$	$0.0359 \pm 0.0016 \pm 0.0153$	$0.0181 \pm 0.0012 \pm 0.0076$
36.854	$0.0654 \pm 0.0032 \pm 0.0108$	$0.0590 \pm 0.0031 \pm 0.0139$	$0.0516 \pm 0.0030 \pm 0.0192$	$0.0302 \pm 0.0022 \pm 0.0187$	$0.0102 \pm 0.0013 \pm 0.0066$
57.580	$0.0502 \pm 0.0072 \pm 0.0126$	$0.0454 \pm 0.0065 \pm 0.0139$	$0.0436 \pm 0.0065 \pm 0.0237$	$0.0136 \pm 0.0030 \pm 0.0092$	$0.0028 \pm 0.0012 \pm 0.0030$
80.592	$0.0352 \pm 0.0089 \pm 0.0109$	$0.0307 \pm 0.0086 \pm 0.0106$	$0.0245 \pm 0.0072 \pm 0.0096$	$0.0041 \pm 0.0021 \pm 0.0024$	$0.0010 \pm 0.0010 \pm 0.0021$
116.337	$0.0411 \pm 0.0291 \pm 0.0090$	$0.0351 \pm 0.0249 \pm 0.0152$	$0.0099 \pm 0.0099 \pm 0.0059$	$0.0000 \pm 0.0000 \pm 0.0000$	$0.0000 \pm 0.0000 \pm 0.0000$

Table 6.6: Normalised differential cross section for $\log_{10} y_2$.

$\langle Q \rangle$	$\log_{10} y_3 \in [-2.000, -1.800]$	$\log_{10} y_3 \in [-1.800, -1.600]$	$\log_{10} y_3 \in [-1.600, -1.400]$	$\log_{10} y_3 \in [-1.400, -1.200]$	$\log_{10} y_3 \in [-1.200, -1.000]$
14.926	$0.1091 \pm 0.0027 \pm 0.0204$	$0.1649 \pm 0.0037 \pm 0.0341$	$0.1800 \pm 0.0041 \pm 0.0383$	$0.1510 \pm 0.0037 \pm 0.0350$	$0.1010 \pm 0.0030 \pm 0.0291$
17.750	$0.1568 \pm 0.0032 \pm 0.0425$	$0.1772 \pm 0.0036 \pm 0.0472$	$0.1514 \pm 0.0033 \pm 0.0394$	$0.1059 \pm 0.0027 \pm 0.0285$	$0.0643 \pm 0.0020 \pm 0.0205$
23.816	$0.1822 \pm 0.0041 \pm 0.0674$	$0.1448 \pm 0.0035 \pm 0.0515$	$0.0946 \pm 0.0027 \pm 0.0347$	$0.0576 \pm 0.0020 \pm 0.0222$	$0.0364 \pm 0.0016 \pm 0.0133$
36.854	$0.1231 \pm 0.0049 \pm 0.0607$	$0.0846 \pm 0.0041 \pm 0.0413$	$0.0540 \pm 0.0031 \pm 0.0249$	$0.0341 \pm 0.0024 \pm 0.0163$	$0.0210 \pm 0.0019 \pm 0.0092$
57.580	$0.0614 \pm 0.0078 \pm 0.0368$	$0.0446 \pm 0.0073 \pm 0.0248$	$0.0325 \pm 0.0060 \pm 0.0130$	$0.0292 \pm 0.0061 \pm 0.0159$	$0.0140 \pm 0.0038 \pm 0.0061$
80.592	$0.0655 \pm 0.0129 \pm 0.0225$	$0.0360 \pm 0.0106 \pm 0.0177$	$0.0136 \pm 0.0049 \pm 0.0058$	$0.0034 \pm 0.0034 \pm 0.0012$	$0.0064 \pm 0.0038 \pm 0.0036$
116.337	$0.0013 \pm 0.0013 \pm 0.0004$	$0.0038 \pm 0.0038 \pm 0.0013$	$0.0138 \pm 0.0139 \pm 0.0048$	$0.0006 \pm 0.0006 \pm 0.0002$	$0.0000 \pm 0.0000 \pm 0.0000$

$\langle Q \rangle$	$\log_{10} y_3 \in [-1.000, -0.800]$	$\log_{10} y_3 \in [-0.800, -0.600]$	$\log_{10} y_3 \in [-0.600, -0.400]$	$\log_{10} y_3 \in [-0.400, -0.200]$	$\log_{10} y_3 \in [-0.200, 0.000]$
14.926	$0.0585 \pm 0.0023 \pm 0.0196$	$0.0280 \pm 0.0015 \pm 0.0101$	$0.0117 \pm 0.0010 \pm 0.0051$	$0.0044 \pm 0.0006 \pm 0.0025$	$0.0018 \pm 0.0004 \pm 0.0010$
17.750	$0.0359 \pm 0.0015 \pm 0.0121$	$0.0188 \pm 0.0011 \pm 0.0067$	$0.0087 \pm 0.0008 \pm 0.0035$	$0.0038 \pm 0.0006 \pm 0.0016$	$0.0010 \pm 0.0003 \pm 0.0005$
23.816	$0.0214 \pm 0.0012 \pm 0.0071$	$0.0112 \pm 0.0009 \pm 0.0038$	$0.0037 \pm 0.0005 \pm 0.0015$	$0.0011 \pm 0.0002 \pm 0.0005$	$0.0003 \pm 0.0002 \pm 0.0003$
36.854	$0.0096 \pm 0.0013 \pm 0.0036$	$0.0051 \pm 0.0009 \pm 0.0016$	$0.0027 \pm 0.0008 \pm 0.0014$	$0.0003 \pm 0.0002 \pm 0.0003$	$0.0000 \pm 0.0000 \pm 0.0000$
57.580	$0.0060 \pm 0.0025 \pm 0.0035$	$0.0016 \pm 0.0012 \pm 0.0010$	$0.0001 \pm 0.0001 \pm 0.0002$	$0.0000 \pm 0.0000 \pm 0.0000$	$0.0000 \pm 0.0000 \pm 0.0000$
80.592	$0.0085 \pm 0.0062 \pm 0.0080$	$0.0010 \pm 0.0011 \pm 0.0010$	$0.0000 \pm 0.0000 \pm 0.0000$	$0.0000 \pm 0.0000 \pm 0.0000$	$0.0000 \pm 0.0000 \pm 0.0000$
116.337	$0.0000 \pm 0.0000 \pm 0.0000$	$0.0000 \pm 0.0000 \pm 0.0000$	$0.0000 \pm 0.0000 \pm 0.0000$	$0.0000 \pm 0.0000 \pm 0.0000$	$0.0000 \pm 0.0000 \pm 0.0000$

Table 6.7: Normalised differential cross section for $\log_{10} y_3$.

$\langle Q \rangle$	$\log_{10} y_4 \in [-2.000, -1.800]$	$\log_{10} y_4 \in [-1.800, -1.600]$	$\log_{10} y_4 \in [-1.600, -1.400]$	$\log_{10} y_4 \in [-1.400, -1.200]$	$\log_{10} y_4 \in [-1.200, -1.000]$
14.926	$0.1631 \pm 0.0035 \pm 0.0596$	$0.1768 \pm 0.0039 \pm 0.0659$	$0.1380 \pm 0.0036 \pm 0.0554$	$0.0809 \pm 0.0028 \pm 0.0370$	$0.0319 \pm 0.0017 \pm 0.0173$
17.750	$0.1768 \pm 0.0035 \pm 0.0884$	$0.1426 \pm 0.0032 \pm 0.0680$	$0.0898 \pm 0.0026 \pm 0.0429$	$0.0438 \pm 0.0018 \pm 0.0216$	$0.0184 \pm 0.0011 \pm 0.0104$
23.816	$0.1426 \pm 0.0036 \pm 0.0958$	$0.0845 \pm 0.0027 \pm 0.0534$	$0.0407 \pm 0.0018 \pm 0.0267$	$0.0169 \pm 0.0011 \pm 0.0108$	$0.0064 \pm 0.0007 \pm 0.0038$
36.854	$0.0673 \pm 0.0038 \pm 0.0612$	$0.0317 \pm 0.0024 \pm 0.0264$	$0.0157 \pm 0.0018 \pm 0.0121$	$0.0061 \pm 0.0011 \pm 0.0045$	$0.0017 \pm 0.0005 \pm 0.0010$
57.580	$0.0284 \pm 0.0061 \pm 0.0288$	$0.0092 \pm 0.0030 \pm 0.0072$	$0.0055 \pm 0.0024 \pm 0.0040$	$0.0005 \pm 0.0005 \pm 0.0004$	$0.0000 \pm 0.0000 \pm 0.0000$
80.592	$0.0134 \pm 0.0053 \pm 0.0073$	$0.0010 \pm 0.0010 \pm 0.0011$	$0.0018 \pm 0.0018 \pm 0.0019$	$0.0031 \pm 0.0035 \pm 0.0036$	$0.0000 \pm 0.0000 \pm 0.0000$
116.337	$0.0035 \pm 0.0035 \pm 0.0019$	$0.0003 \pm 0.0003 \pm 0.0002$	$0.0000 \pm 0.0000 \pm 0.0000$	$0.0000 \pm 0.0000 \pm 0.0000$	$0.0000 \pm 0.0000 \pm 0.0000$
$\langle Q \rangle$	$\log_{10} y_4 \in [-1.000, -0.800]$	$\log_{10} y_4 \in [-0.800, -0.600]$	$\log_{10} y_4 \in [-0.600, -0.400]$	$\log_{10} y_4 \in [-0.400, -0.200]$	$\log_{10} y_4 \in [-0.200, 0.000]$
14.926	$0.0107 \pm 0.0009 \pm 0.0063$	$0.0021 \pm 0.0004 \pm 0.0012$	$0.0003 \pm 0.0001 \pm 0.0003$	$0.0003 \pm 0.0002 \pm 0.0003$	$0.0000 \pm 0.0000 \pm 0.0000$
17.750	$0.0058 \pm 0.0006 \pm 0.0034$	$0.0013 \pm 0.0003 \pm 0.0008$	$0.0003 \pm 0.0001 \pm 0.0002$	$0.0001 \pm 0.0001 \pm 0.0001$	$0.0000 \pm 0.0000 \pm 0.0000$
23.816	$0.0022 \pm 0.0004 \pm 0.0013$	$0.0005 \pm 0.0002 \pm 0.0004$	$0.0006 \pm 0.0004 \pm 0.0007$	$0.0000 \pm 0.0000 \pm 0.0000$	$0.0000 \pm 0.0000 \pm 0.0000$
36.854	$0.0002 \pm 0.0001 \pm 0.0001$	$0.0001 \pm 0.0001 \pm 0.0003$	$0.0000 \pm 0.0000 \pm 0.0000$	$0.0000 \pm 0.0000 \pm 0.0000$	$0.0000 \pm 0.0000 \pm 0.0000$
57.580	$0.0000 \pm 0.0000 \pm 0.0000$	$0.0000 \pm 0.0000 \pm 0.0000$	$0.0000 \pm 0.0000 \pm 0.0000$	$0.0000 \pm 0.0000 \pm 0.0000$	$0.0000 \pm 0.0000 \pm 0.0000$
80.592	$0.0000 \pm 0.0000 \pm 0.0000$	$0.0006 \pm 0.0006 \pm 0.0007$	$0.0000 \pm 0.0000 \pm 0.0000$	$0.0000 \pm 0.0000 \pm 0.0000$	$0.0000 \pm 0.0000 \pm 0.0000$
116.337	$0.0000 \pm 0.0000 \pm 0.0000$	$0.0000 \pm 0.0000 \pm 0.0000$	$0.0000 \pm 0.0000 \pm 0.0000$	$0.0000 \pm 0.0000 \pm 0.0000$	$0.0000 \pm 0.0000 \pm 0.0000$

Table 6.8: Normalised differential cross section for $\log_{10} y_4$.

$\langle Q \rangle$	$K_{out}/Q \in [0.000, 0.100]$	$K_{out}/Q \in [0.100, 0.200]$	$K_{out}/Q \in [0.200, 0.300]$	$K_{out}/Q \in [0.300, 0.400]$	$K_{out}/Q \in [0.400, 0.500]$
14.926	$0.0007 \pm 0.0003 \pm 0.0014$	$0.0329 \pm 0.0029 \pm 0.0142$	$0.1470 \pm 0.0067 \pm 0.0056$	$0.2204 \pm 0.0073 \pm 0.0204$	$0.1989 \pm 0.0063 \pm 0.0238$
17.750	$0.0012 \pm 0.0004 \pm 0.0033$	$0.0521 \pm 0.0036 \pm 0.0195$	$0.1971 \pm 0.0071 \pm 0.0112$	$0.2611 \pm 0.0076 \pm 0.0247$	$0.1917 \pm 0.0056 \pm 0.0162$
23.816	$0.0032 \pm 0.0007 \pm 0.0052$	$0.1222 \pm 0.0065 \pm 0.0337$	$0.2853 \pm 0.0098 \pm 0.0247$	$0.2419 \pm 0.0080 \pm 0.0296$	$0.1537 \pm 0.0061 \pm 0.0145$
36.854	$0.0188 \pm 0.0028 \pm 0.0161$	$0.2849 \pm 0.0165 \pm 0.0199$	$0.3462 \pm 0.0174 \pm 0.0508$	$0.1835 \pm 0.0110 \pm 0.0249$	$0.0798 \pm 0.0070 \pm 0.0100$
57.580	$0.0686 \pm 0.0164 \pm 0.0291$	$0.5115 \pm 0.0653 \pm 0.0370$	$0.2575 \pm 0.0365 \pm 0.0320$	$0.0794 \pm 0.0210 \pm 0.0170$	$0.0637 \pm 0.0188 \pm 0.0188$
80.592	$0.0716 \pm 0.0359 \pm 0.0304$	$0.4351 \pm 0.1174 \pm 0.1162$	$0.4031 \pm 0.0919 \pm 0.0950$	$0.0336 \pm 0.0174 \pm 0.0041$	$0.0093 \pm 0.0094 \pm 0.0044$
116.337	$0.1638 \pm 0.1638 \pm 0.0698$	$0.8355 \pm 0.3754 \pm 0.2130$	$0.0007 \pm 0.0007 \pm 0.0004$	$0.0000 \pm 0.0000 \pm 0.0000$	$0.0000 \pm 0.0000 \pm 0.0000$

$\langle Q \rangle$	$K_{out}/Q \in [0.500, 0.600]$	$K_{out}/Q \in [0.600, 0.700]$	$K_{out}/Q \in [0.700, 0.800]$	$K_{out}/Q \in [0.800, 0.900]$	$K_{out}/Q \in [0.900, 1.000]$
14.926	$0.1502 \pm 0.0052 \pm 0.0077$	$0.1006 \pm 0.0042 \pm 0.0092$	$0.0563 \pm 0.0031 \pm 0.0069$	$0.0304 \pm 0.0021 \pm 0.0052$	$0.0147 \pm 0.0014 \pm 0.0041$
17.750	$0.1163 \pm 0.0041 \pm 0.0109$	$0.0671 \pm 0.0031 \pm 0.0073$	$0.0438 \pm 0.0027 \pm 0.0068$	$0.0237 \pm 0.0019 \pm 0.0045$	$0.0120 \pm 0.0012 \pm 0.0035$
23.816	$0.0859 \pm 0.0043 \pm 0.0112$	$0.0470 \pm 0.0032 \pm 0.0077$	$0.0247 \pm 0.0022 \pm 0.0046$	$0.0131 \pm 0.0016 \pm 0.0038$	$0.0063 \pm 0.0011 \pm 0.0019$
36.854	$0.0433 \pm 0.0053 \pm 0.0078$	$0.0209 \pm 0.0035 \pm 0.0060$	$0.0106 \pm 0.0025 \pm 0.0034$	$0.0051 \pm 0.0017 \pm 0.0027$	$0.0016 \pm 0.0007 \pm 0.0007$
57.580	$0.0144 \pm 0.0074 \pm 0.0055$	$0.0046 \pm 0.0038 \pm 0.0021$	$0.0004 \pm 0.0004 \pm 0.0013$	$0.0000 \pm 0.0000 \pm 0.0000$	$0.0000 \pm 0.0000 \pm 0.0000$
80.592	$0.0345 \pm 0.0360 \pm 0.0167$	$0.0128 \pm 0.0155 \pm 0.0087$	$0.0000 \pm 0.0000 \pm 0.0000$	$0.0000 \pm 0.0000 \pm 0.0000$	$0.0000 \pm 0.0000 \pm 0.0000$
116.337	$0.0000 \pm 0.0000 \pm 0.0000$	$0.0000 \pm 0.0000 \pm 0.0000$	$0.0000 \pm 0.0000 \pm 0.0000$	$0.0000 \pm 0.0000 \pm 0.0000$	$0.0000 \pm 0.0000 \pm 0.0000$

Table 6.9: Normalised differential cross section for K_{out}/Q.

$\langle Q \rangle$	$\chi \in [0.000, 0.100]$	$\chi \in [0.100, 0.200]$	$\chi \in [0.200, 0.300]$	$\chi \in [0.300, 0.400]$	$\chi \in [0.400, 0.500]$
14.926	$0.0478 \pm 0.0007 \pm 0.0025$	$0.0451 \pm 0.0006 \pm 0.0007$	$0.0416 \pm 0.0005 \pm 0.0007$	$0.0372 \pm 0.0004 \pm 0.0007$	$0.0345 \pm 0.0004 \pm 0.0003$
17.750	$0.0508 \pm 0.0007 \pm 0.0018$	$0.0479 \pm 0.0006 \pm 0.0012$	$0.0443 \pm 0.0005 \pm 0.0006$	$0.0398 \pm 0.0004 \pm 0.0004$	$0.0344 \pm 0.0003 \pm 0.0004$
23.816	$0.0544 \pm 0.0011 \pm 0.0021$	$0.0522 \pm 0.0009 \pm 0.0016$	$0.0460 \pm 0.0007 \pm 0.0008$	$0.0407 \pm 0.0006 \pm 0.0003$	$0.0344 \pm 0.0004 \pm 0.0003$
36.854	$0.0635 \pm 0.0026 \pm 0.0024$	$0.0592 \pm 0.0018 \pm 0.0015$	$0.0497 \pm 0.0014 \pm 0.0005$	$0.0417 \pm 0.0012 \pm 0.0006$	$0.0330 \pm 0.0009 \pm 0.0004$
57.580	$0.0802 \pm 0.0089 \pm 0.0107$	$0.0678 \pm 0.0065 \pm 0.0024$	$0.0544 \pm 0.0056 \pm 0.0042$	$0.0382 \pm 0.0028 \pm 0.0034$	$0.0340 \pm 0.0026 \pm 0.0015$
80.592	$0.0649 \pm 0.0157 \pm 0.0112$	$0.0630 \pm 0.0086 \pm 0.0058$	$0.0637 \pm 0.0100 \pm 0.0049$	$0.0396 \pm 0.0035 \pm 0.0035$	$0.0262 \pm 0.0034 \pm 0.0044$
116.337	$0.0618 \pm 0.0205 \pm 0.0149$	$0.1024 \pm 0.0344 \pm 0.0079$	$0.0550 \pm 0.0145 \pm 0.0071$	$0.0343 \pm 0.0120 \pm 0.0042$	$0.0358 \pm 0.0146 \pm 0.0065$
$\langle Q \rangle$	$\chi \in [0.500, 0.600]$	$\chi \in [0.600, 0.700]$	$\chi \in [0.700, 0.800]$	$\chi \in [0.800, 0.900]$	$\chi \in [0.900, 1.000]$
14.926	$0.0312 \pm 0.0003 \pm 0.0003$	$0.0280 \pm 0.0003 \pm 0.0005$	$0.0259 \pm 0.0002 \pm 0.0005$	$0.0236 \pm 0.0002 \pm 0.0005$	$0.0223 \pm 0.0002 \pm 0.0005$
17.750	$0.0302 \pm 0.0003 \pm 0.0007$	$0.0276 \pm 0.0003 \pm 0.0005$	$0.0250 \pm 0.0002 \pm 0.0006$	$0.0230 \pm 0.0002 \pm 0.0006$	$0.0211 \pm 0.0002 \pm 0.0006$
23.816	$0.0301 \pm 0.0004 \pm 0.0005$	$0.0271 \pm 0.0003 \pm 0.0006$	$0.0243 \pm 0.0003 \pm 0.0007$	$0.0213 \pm 0.0002 \pm 0.0007$	$0.0192 \pm 0.0002 \pm 0.0005$
36.854	$0.0270 \pm 0.0006 \pm 0.0005$	$0.0251 \pm 0.0006 \pm 0.0011$	$0.0219 \pm 0.0005 \pm 0.0012$	$0.0187 \pm 0.0005 \pm 0.0009$	$0.0166 \pm 0.0003 \pm 0.0006$
57.580	$0.0253 \pm 0.0023 \pm 0.0030$	$0.0202 \pm 0.0017 \pm 0.0014$	$0.0180 \pm 0.0014 \pm 0.0015$	$0.0177 \pm 0.0012 \pm 0.0019$	$0.0125 \pm 0.0009 \pm 0.0012$
80.592	$0.0313 \pm 0.0055 \pm 0.0040$	$0.0236 \pm 0.0033 \pm 0.0017$	$0.0221 \pm 0.0041 \pm 0.0021$	$0.0217 \pm 0.0041 \pm 0.0034$	$0.0174 \pm 0.0065 \pm 0.0019$
116.337	$0.0235 \pm 0.0047 \pm 0.0061$	$0.0170 \pm 0.0030 \pm 0.0029$	$0.0226 \pm 0.0079 \pm 0.0045$	$0.0159 \pm 0.0032 \pm 0.0017$	$0.0128 \pm 0.0030 \pm 0.0024$

Table 6.10: Normalised differential cross section for χ.

Bibliography

[1] **TASSO** Collaboration, R. Brandelik *et al.*, "PROPERTIES OF HADRON FINAL STATES IN e+ e- ANNIHILATION AT 13-GeV AND 17-GeV CENTER-OF-MASS ENERGIES," *Phys. Lett.* **B83** (1979) 261.

[2] **PLUTO** Collaboration, C. Berger *et al.*, "ENERGY-ENERGY CORRELATIONS IN e+ e- ANNIHILATION INTO HADRONS," *Phys. Lett.* **B99** (1981) 292.

[3] A. Petersen *et al.*, "MULTI - HADRONIC EVENTS AT E(cm) = 29-GeV AND PREDICTIONS OF QCD MODELS FROM E(cm) = 29-GeV TO E(cm) = 93-GeV," *Phys. Rev.* **D37** (1988) 1.

[4] S. Kluth, P. A. Movilla Fernandez, S. Bethke, C. Pahl, and P. Pfeifenschneider, "A measurement of the QCD colour factors using event shape distributions at s**(1/2) = 14-GeV to 189-GeV," *Eur. Phys. J.* **C21** (2001) 199–210, `hep-ex/0012044`.

[5] S. Bethke, "Determination of the QCD coupling alpha(s)," *J. Phys.* **G26** (2000) R27, `hep-ex/0004021`.

[6] R.K. Ellis, W.J. Stirling, B.R. Webber, *QCD and Collider Physics*. Cambridge University Press, 1996.

[7] M. Dasgupta and B. R. Webber, "Power corrections to event shapes in deep inelastic scattering," *Eur. Phys. J.* **C1** (1998) 539–546, `hep-ph/9704297`.

[8] **H1** Collaboration, C. Adloff *et al.*, "Measurement of event shape variables in deep inelastic e p scattering," *Phys. Lett.* **B406** (1997) 256–270, `hep-ex/9706002`.

[9] T. Sjostrand, "High-energy physics event generation with PYTHIA 5.7 and JETSET 7.4," *Comput. Phys. Commun.* **82** (1994) 74–90.

[10] G. Corcella *et al.*, "HERWIG 6: An event generator for hadron emission reactions with interfering gluons (including supersymmetric processes)," *JHEP* **01** (2001) 010, `hep-ph/0011363`.

[11] S. Frixione and B. R. Webber, "Matching NLO QCD computations and parton shower simulations," *JHEP* **06** (2002) 029, hep-ph/0204244.

[12] Y. L. Dokshitzer and B. R. Webber, "Power corrections to event shape distributions," *Phys. Lett.* **B404** (1997) 321–327, hep-ph/9704298.

[13] D. E. Soper, "Jet observables in theory and reality,hep-ph/9706320," hep-ph/9706320.

[14] **H1** Collaboration, C. Adloff *et al.*, "Investigation of power corrections to event shape variables measured in deep-inelastic scattering," *Eur. Phys. J.* **C14** (2000) 255–269, hep-ex/9912052.

[15] Z. Nagy and Z. Trocsanyi, "Multi-jet cross sections in deep inelastic scattering at next-to-leading order," *Phys. Rev. Lett.* **87** (2001) 082001, hep-ph/0104315.

[16] E. Mirkes and D. Zeppenfeld, "Dijet Production at HERA in Next-to-Leading Order," *Phys. Lett.* **B380** (1996) 205–212, hep-ph/9511448.

[17] S. Catani and M. H. Seymour, "A general algorithm for calculating jet cross sections in NLO QCD," *Nucl. Phys.* **B485** (1997) 291–419, hep-ph/9605323.

[18] D. Graudenz, "DISASTER++ version 1.0," hep-ph/9710244.

[19] V. N. Gribov and L. N. Lipatov, "Deep inelastic e p scattering in perturbation theory," *Yad. Fiz.* **15** (1972) 781–807.

[20] V. N. Gribov and L. N. Lipatov, "e+ e- pair annihilation and deep inelastic e p scattering in perturbation theory," *Yad. Fiz.* **15** (1972) 1218–1237.

[21] G. Altarelli and G. Parisi, "ASYMPTOTIC FREEDOM IN PARTON LANGUAGE," *Nucl. Phys.* **B126** (1977) 298.

[22] M. Bengtsson and T. Sjostrand, "PARTON SHOWERS IN LEPTOPRODUCTION EVENTS," *Z. Phys.* **C37** (1988) 465.

[23] A. Banfi, G. P. Salam, and G. Zanderighi, "Generalized resummation of QCD final-state observables," hep-ph/0304148.

[24] M. Dasgupta and G. P. Salam, "Resummation of the jet broadening in DIS," *Eur. Phys. J.* **C24** (2002) 213–236, hep-ph/0110213.

[25] M. Dasgupta and G. P. Salam, "Resummed event-shape variables in DIS," *JHEP* **08** (2002) 032, hep-ph/0208073.

[26] Y. L. Dokshitzer, G. Marchesini, and B. R. Webber, "Dispersive Approach to Power-Behaved Contributions in QCD Hard Processes," *Nucl. Phys.* **B469** (1996) 93–142, hep-ph/9512336.

[27] M. Dasgupta and B. R. Webber, "Two-loop enhancement factor for 1/Q corrections to event shapes in deep inelastic scattering," *JHEP* **10** (1998) 001, hep-ph/9809247.

[28] **DELPHI** Collaboration, J. Abdallah *et al.*, "A study of the energy evolution of event shape distributions and their means with the DELPHI detector at LEP," *Eur. Phys. J.* **C29** (2003) 285–312, hep-ex/0307048.

[29] A. Banfi, G. Marchesini, G. Smye, and G. Zanderighi, "Out-of-plane QCD radiation in DIS with high p(t) jets," *JHEP* **11** (2001) 066, hep-ph/0111157.

[30] A. Banfi, G. Marchesini, and G. Smye, "Azimuthal correlation in DIS," *JHEP* **04** (2002) 024, hep-ph/0203150.

[31] A. Banfi, G. Marchesini, Y. L. Dokshitzer, and G. Zanderighi, "QCD analysis of near-to-planar 3-jet events," *JHEP* **07** (2000) 002, hep-ph/0004027.

[32] S. Catani, Y. L. Dokshitzer, M. H. Seymour, and B. R. Webber, "Longitudinally invariant K(t) clustering algorithms for hadron hadron collisions," *Nucl. Phys.* **B406** (1993) 187–224.

[33] S. Catani, Y. L. Dokshitzer, and B. R. Webber, "The K-perpendicular clustering algorithm for jets in deep inelastic scattering and hadron collisions," *Phys. Lett.* **B285** (1992) 291–299.

[34] **HERMES** Collaboration, K. Ackerstaff *et al.*, "HERMES spectrometer," *Nucl. Instrum. Meth.* **A417** (1998) 230–265, hep-ex/9806008.

[35] T. Lohse *et al.*, "HERA-B: An Experiment to study CP violation in the B system using an internal target at the HERA proton ring,". DESY-PRC-93-04.

[36] **H1** Collaboration, I. Abt *et al.*, "The H1 detector at HERA," *Nucl. Instrum. Meth.* **A386** (1997) 310–347.

[37] **H1** Collaboration, I. Abt *et al.*, "The Tracking, calorimeter and muon detectors of the H1 experiment at HERA," *Nucl. Instrum. Meth.* **A386** (1997) 348–396.

[38] CERN, "GEANT, Detector Description and Simulation Tool,". CERN Program Library Long Writeup W5013.

[39] H. Jung, "Hard diffractive scattering in high-energy e p collisions and the Monte Carlo generation RAPGAP," *Comp. Phys. Commun.* **86** (1995) 147–161.

[40] K. Charchula, G. A. Schuler, and H. Spiesberger, "Combined QED and QCD radiative effects in deep inelastic lepton - proton scattering: The Monte Carlo generator DJANGO6," *Comput. Phys. Commun.* **81** (1994) 381–402.

[41] **CTEQ** Collaboration, H. L. Lai *et al.*, "Global QCD analysis of parton structure of the nucleon: CTEQ5 parton distributions," *Eur. Phys. J.* **C12** (2000) 375–392, hep-ph/9903282.

[42] H. Plothow-Besch, "PDFLIB: A Library of all available parton density functions of the nucleon, the pion and the photon and the corresponding alpha-s calculations," *Comput. Phys. Commun.* **75** (1993) 396–416.

[43] CERN, "Proton, Pion and Photon Parton Density Functions, Parton Density Functions of the Nucleus, and alpha(s) calculations. User's Manual, Version 8.04,". CERN Program Library Long Writeup W5051.

[44] A. Kwiatkowski, H. Spiesberger, and H. J. Mohring, "HERACLES: AN EVENT GENERATOR FOR e p INTERACTIONS AT HERA ENERGIES INCLUDING RADIATIVE PROCESSES: VERSION 1.0," *Comp. Phys. Commun.* **69** (1992) 155–172.

[45] G. Ingelman, A. Edin, and J. Rathsman, "LEPTO 6.5 - A Monte Carlo Generator for Deep Inelastic Lepton-Nucleon Scattering," *Comput. Phys. Commun.* **101** (1997) 108–134, hep-ph/9605286.

[46] L. Lonnblad, "ARIADNE version 4: A Program for simulation of QCD cascades implementing the color dipole model," *Comput. Phys. Commun.* **71** (1992) 15–31.

[47] T. Sjostrand *et al.*, "High-energy-physics event generation with PYTHIA 6.1," *Comput. Phys. Commun.* **135** (2001) 238–259, hep-ph/0010017.

[48] P. Kandel, "Monte-Carlo-Untersuchungen zur Weitwinkelbremsstrahlung im H1-Detektor," 1998.

[49] T. Abe, "GRAPE-Dilepton (Version 1.1): A generator for dilepton production in e p collisions," *Comput. Phys. Commun.* **136** (2001) 126–147, hep-ph/0012029.

[50] U. Baur, J. A. M. Vermaseren, and D. Zeppenfeld, "Electroweak vector boson production in high-energy e p collisions," *Nucl. Phys.* **B375** (1992) 3–44.

[51] **H1** Collaboration, C. Adloff *et al.*, "Measurement and QCD analysis of neutral and charged current cross sections at HERA," hep-ex/0304003.

[52] B. Heinemann, "Measurement of Charged Current and Neutral Current Cross Sections in Positron-Proton Collisions ats**(1/2) = 300- GeV,". DESY-THESIS-1999-046.

[53] E. Chabert *et al.*, "QBGFMAR, An Updated Phan Package for Cosmic and Halo Muon Topological Rejection in High PT Physics Analysis,". H1 internal note-556.

[54] C. Issever *et al.*, "An Improved Weighting Algorithm to Achieve Software Compensation in a Fine Grained LaR Calorimeter,". H1 internal note-608.

[55] **H1** Collaboration, C. Adloff *et al.*, "Diffraction dissociation in photoproduction at HERA," *Z. Phys.* **C74** (1997) 221–236, hep-ex/9702003.

[56] **H1** Collaboration, C. Adloff *et al.*, "Measurement of dijet cross sections in photoproduction at HERA," *Eur. Phys. J.* **C25** (2002) 13–23, hep-ex/0201006.

[57] K. Rabbertz, "Power corrections to event shape variables measured in e p deep-inelastic scattering," hep-ph/0001051.

[58] G. Cowan, *Statistical Data Analysis*. Oxford Science Publications, 1998.

[59] G. D'Agostini, "A Multidimensional unfolding method based on Bayes' theorem," *Nucl. Instrum. Meth.* **A362** (1995) 487–498.

[60] **H1** Collaboration, A. Aktas *et al.*, "Measurement of dijet production at low Q**2 at HERA," hep-ex/0401010.

[61] G. D'Agostini, "Comments on the Bayesian unfolding,". ZEUS-Note 95-166.

[62] **H1** Collaboration, C. Adloff *et al.*, "Measurement of neutral and charged current cross sections in electron proton collisions at high Q**2," *Eur. Phys. J.* **C19** (2001) 269–288, hep-ex/0012052.

[63] V. Blobel and E. Lohrmann, *Statistische und numerische Methoden der Datenanalyse*. Teubner, 1998.

[64] M. Dasgupta and G. P. Salam, "private communication."

[65] G. J. McCance, "NLO program comparison for event shapes," hep-ph/9912481.

[66] **ZEUS** Collaboration, S. Chekanov *et al.*, "Measurement of event shapes in deep inelastic scattering at HERA," *Eur. Phys. J.* **C27** (2003) 531–545, hep-ex/0211040.

[67] V. Antonelli, M. Dasgupta, and G. P. Salam, "Resummation of thrust distributions in DIS," *JHEP* **02** (2000) 001, hep-ph/9912488.

[68] A. D. Martin, R. G. Roberts, W. J. Stirling, and R. S. Thorne, "MRST2001: Partons and alpha(s) from precise deep inelastic scattering and Tevatron jet data," *Eur. Phys. J.* **C23** (2002) 73–87, hep-ph/0110215.

[69] W. A. Bardeen, A. J. Buras, D. W. Duke, and T. Muta, "DEEP INELASTIC SCATTERING BEYOND THE LEADING ORDER IN ASYMPTOTICALLY FREE GAUGE THEORIES," *Phys. Rev.* **D18** (1978) 3998.

[70] F. James, *MINUIT, Function Minimization and Error Analysis.* CERN Program Library Long Writeup D506, 1994.

[71] M. Wobisch, "Measurement and QCD analysis of jet cross sections in deep-inelastic positron proton collisions at s**(1/2) = 300- GeV,". DESY-THESIS-2000-049.

[72] T. L. Q. W. Group, "Progress on the Combination of QCD Observables at LEP1.5 and LEP2,". ALEPH 98-030 Physic 98-011 , DELPHI 98-30 PHYS 769, L3 Note 2245, OPAL TN 537.

[73] R. W. L. Jones, M. Ford, G. P. Salam, H. Stenzel, and D. Wicke, "Theoretical uncertainties on alpha(s) from event-shape variables in e+ e- annihilations," *JHEP* **12** (2003) 007, hep-ph/0312016.

Bildungsweg

16. April 2004	Ablegung der mündlichen Prüfung und Abschluss der Promotion
Februar 2004	Abgabe der Dissertation, Titel "Measurement and QCD Analysis of Event Shape Variables in Deep-Inelastic Electron-Proton Collisions at HERA"
Juli 2000	Beginn der Promotionsarbeit, Betreuer Prof. Dr. Ch. Berger
Mai 2000	Diplom in Physik an der RWTH Aachen
Februar 2000	Abgabe der Diplomarbeit mit dem Titel "Untersuchung des QED-Bremsstrahlungsprozesses bei kleinen Impulsüberträgen mit dem H1-Detektor bei HERA", PITHA-00/08
Oktober 1998	Beginn der Diplomarbeit am III. Physikalischen Institut B der RWTH Aachen bei Prof. Dr. G. Flügge im Rahmen der H1-Kollaboration, DESY, Hamburg
September 1995	Vordiplom in Physik an der RWTH Aachen
Oktober 1993	Beginn des Physikstudiums an der RWTH Aachen
Mai 1993	Abitur
1984–1993	Besuch des Städt. Mathematisch-Naturwissenschaftlichen Gymnasiums in Mönchengladbach

Danksagung

An erster Stelle bedanke ich mich bei Prof. Dr. Christoph Berger für die Aufgabenstellung und die Betreuung der Dissertation. Mein Dank gilt Prof. Dr. Günter Flügge für die Übernahme des Koreferats.

Dr. Hans-Ulrich Martyn schulde ich Dank für die vielfältigen Anregungen und die Unterstützung während aller Phasen der Analyse. Die Diskussionen mit Dr. Mrinal Dasgupta und Dr. Gavin Salam haben entscheidend zum Gelingen der Arbeit beigetragen.

Für die gute Arbeitsathmosphäre und die schöne Zeit in Hamburg bedanke ich mich bei meinen Bürokollegen Dr. Peer-Oliver Meyer, Dr. Markus Wobisch, Dr. Carlo Duprel, Martin Wessels, Anja Vest, Linus Lindfeld und Lars Finke. Ebenso gilt mein Dank allen Mitgliedern der Aachen-H1 Gruppe, insbesondere Dr. Jürgen Scheins, Dr. Carsten Krauss, Dr. Gilles Frising, Dr. Klaus Rabbertz und Dr. Thomas Hadig.

Für das sorgfältige Korrekturlesen bedanke ich mich bei Dr. Hans-Ulrich Martyn, Christina Diers, Anja Vest, Martin Wessels und Dr. Carlo Duprel.

DESY, HERA und die H1 Kollaboration haben mir hervorragende Arbeitsmöglichkeiten geboten, ich möchte mich bei allen bedanken, die dazu beitragen.

Herzlich danke ich meiner Mutter für die Unterstützung, vor allem während des gesamten Studiums.

Spezieller Dank gilt Christina Diers, ganz besonders für den großartigen Beistand während der kritischeren Phasen der Promotionszeit.